Department of Advanced Materials Science
Graduate School of Frontier Sciences
The University of Tokyo

2009

Master's Thesis

Low-Dimensional Electronic Properties of Oxide Heterostructures

－酸化物ヘテロ構造における低次元電子物性－

Submitted on January 26, 2010
Supervisor: Professor Harold Y. Hwang

86017 Minu Kim

Contents

Chapter 1

Introduction

1.1 Oxides as Materials for Emerging Devices

Research into emergent materials seeks to explore novel materials with a variety of physical properties, and aims to make new functional devices to keep up with the continued demand by society for advances in technology. Conventional silicon-based complementary metal-oxide semiconductor (CMOS) technology has been developed by doubling the density of the integrated circuit every 18 months known as Moore's Law [1]. Since the difficulties of further downscaling are becoming more apparent [2], two axes for further development of devices were recognized by the Semiconductor Industry Association *International Technology Roadmap for Semiconductors* (ITRS) [3], shown in Fig. 1.1. One axis is called "More Moore": the continued reduction of the feature size existing logic devices. The other axis is called "More than Moore": the incorporation of devices with functionalities that do not necessarily scale according to Moore's Law, but provide additional value to the end product in different ways. Following this latter axis, emergent materials research is a long-term topic focused on the creation of new types of devices which operate in novel ways.

Transition metal oxides have a variety of physical properties showing almost every phase possible in the solid state: insulator, semiconductor, metal, superconductor, ferromagnetism, anti-ferromagnetism, ferroelectricity, piezoelectricity, and so on. The fact that a large number of these materials have the same perovskite structure and similar lattice constant allows the growth of heteroepitaxial layers with different ground states and is advantageous to further integration. Also the oxides are in general stabilized in atmosphere, so that vacuum processing of oxides is less energy-consuming, which has important benefits in the future eco-friendly society. From these features, it is expected that multi-functional, low-cost, and eco-friendly devices operating with unconventional mechanisms can be realized. Thus, research into the physical properties of oxides is *essential* to make a fundamental base towards future post-semiconductor technologies.

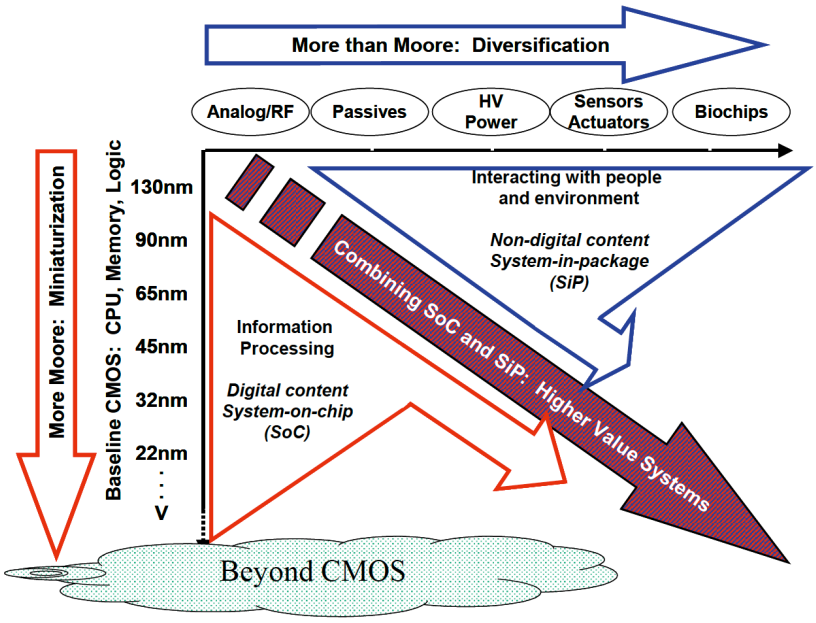

Figure 1.1: "Moore's law and more," taken from the ITRS report [3]. Vertical axis refers to "More Moore," heading to further miniaturization. Horizontal axis is "More Than Moore," consisting of the functional diversification.

1.2 Strontium Titanate

$SrTiO_3$, the target material of this Thesis, is one of the representative perovskite oxides. Perovskite oxides have a chemical composition of ABO_3, where A is an alkaline-earth or rare-earth ion, and B is a transition metal ion, as shown in Fig. 1.2. The octahedron structure of oxygen ions O around the transition metal ion B makes a crystal field which lifts the degeneracy of the $3d$-orbital of B. Many of the wide range of physical properties of the oxides originate from the large freedom of these d-electrons. These are known as strongly correlated systems [4], famous for showing behavior such as the Mott insulator [5], colossal magnetoresistance [6], high temperature superconductivity [7], and so on. With the establishment of single crystal growth techniques of $SrTiO_3$ (using the Verneuil method), it is the most widely used substrate for the heteroepitaxial growth of oxide thin films, such as $YBa_2Cu_3O_7$, manganites, and so on. Thus, the research into $SrTiO_3$ has considerable repercussions on all of the perovskite oxides, as well as being an interesting physical system in itself, as will be discussed below.

$SrTiO_3$ has been studied for more than a half century ago, beginning with studies of its high dielectric constant at low temperatures. It is also famous for inspiring the research which led to the discovery of the copper oxide-based high temperature superconductors [8]. Some important characteristics of bulk $SrTiO_3$ are itemized below, and in Fig. 1.3.

- Band insulator with bandgap of 3.2 eV [9], but chemical doping or oxygen vacancies

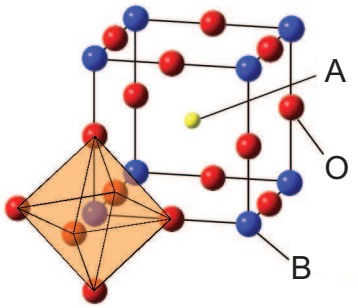

Figure 1.2: Schematic diagram of the atomic structure of the perovskite oxide ABO_3 (courtesy of Y. Kozuka).

induce a metallic state.

- Superconducting with the lowest carrier density known ($10^{18} \sim 10^{19}$ cm^{-3}) [10].
- High dielectric constant at low temperatures [11], which is nonlinear with applied electric field [12]. Does not become ferroelectric at low temperatures, but rather enters into a quantum paraelectric state below 4 K [13].
- High electron mobility ($\approx$ 10000 cm^{2}V^{-1}s^{-1}) for dopant carrier densities in the range 10^{17} to 10^{19} cm^{-3} at low temperatures [14] due to the screening of impurities.
- Large effective mass ($m^* = 1.24 \sim 1.40$) [15]. Small kinetic energy compared to the correlation energy.

Because of the high-mobility and low carrier density of $SrTiO_3$, it is expected that quantum effects may emerge in low dimensional semiconductor heterostructures [16]. Furthermore, $SrTiO_3$ may show an interplay between superconductivity and quantum oscillations [17]. On the other hand, superconductivity in $SrTiO_3$ itself is an interesting topic because of the low carrier density. An approach to the thin limit of a two-dimensional superconductor, with careful thin-film growth control, may reveal novel physics related to the layered copper-oxide superconductors [18].

1.3 Low-Dimensional Electronic Systems in Oxide Heterostructures

There are three common methods to realize low-dimensional electronic systems in oxide heterostructures: first, to use a heterointerface, second, to use the electric field effect, and third, to use the delta-doping technique. In this section, I will introduce each topic briefly. As will be discussed in the following sections, low-dimensional oxide heterostructures show

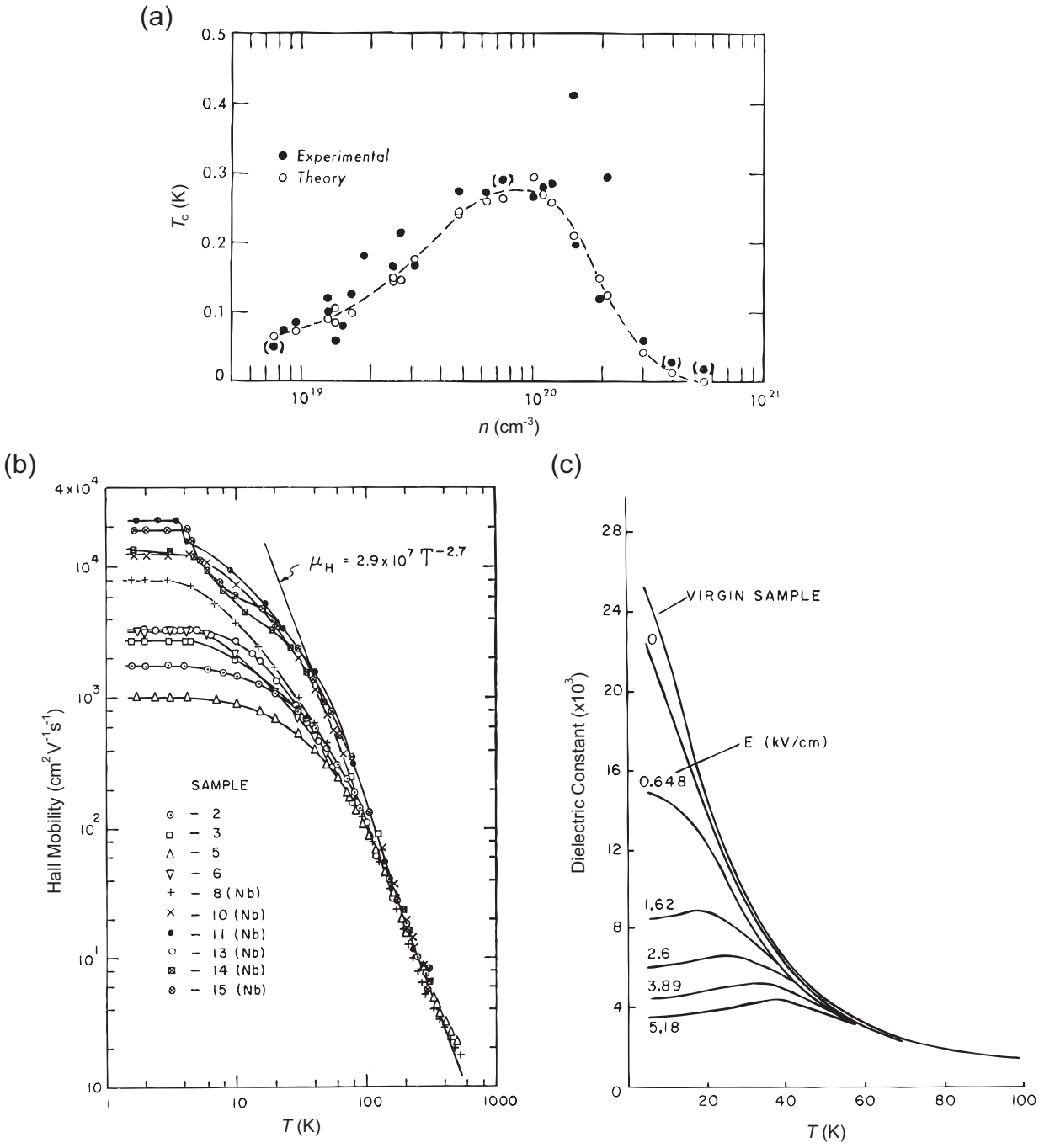

Figure 1.3: Some physical properties of $SrTiO_3$ bulk crystals. (a) Superconducting transition temperature as a function of carrier density for reduced $SrTiO_3$ bulk samples, taken from C. S. Koonce *et al.* [10]. (b) Temperature dependence of the electron Hall mobility in reduced and Nb doped $SrTiO_3$ samples, taken from O. N. Tufte *et al.* [14]. (c) Temperature dependence of the weak-field dielectric constant for an unannealed crystal of $SrTiO_3$, taken from M. A. Saifi *et al.* [11]. The dielectric constant decreases monotonically with the d.c. electric field applied, at low temperatures.

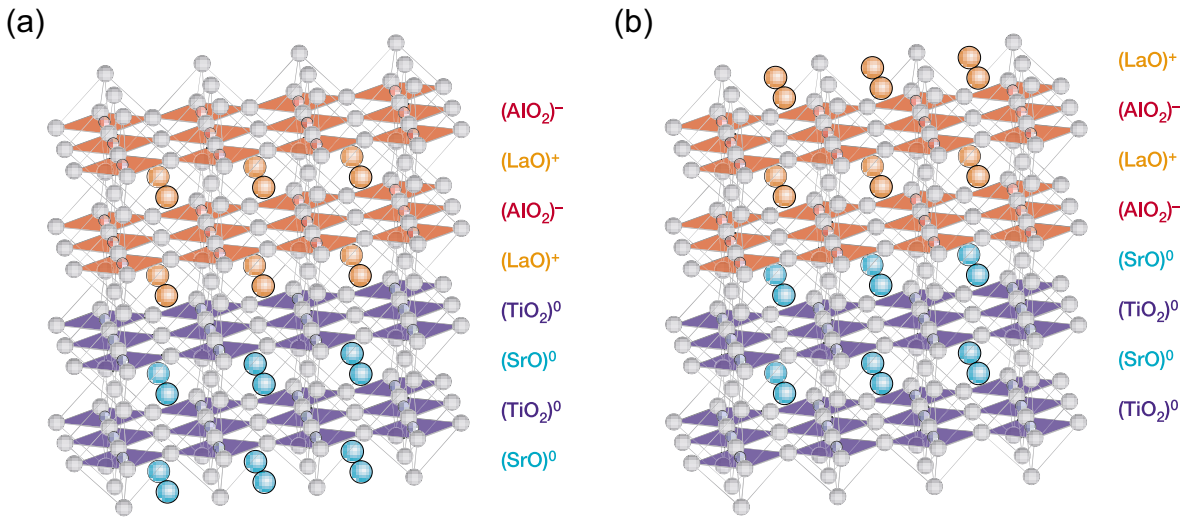

Figure 1.4: Schematic diagrams of the two types of $LaAlO_3/SrTiO_3$ interface, taken from A. Ohtomo and H. Y. Hwang [19]. (a) The N-type $(LaO)^+/(TiO_2)^0$ interface, showing the composition and the ionic state of each layer. (b) The P-type $(AlO_2)^-/(SrO)^0$ interface.

novel physical properties, not found in conventional semiconductors. Therefore this topic has invoked intense interest [20].

1.3.1 Heterointerface Between Insulators

The discovery of a metallic interface between the two insulating oxides $SrTiO_3$ and $LaAlO_3$ in 2004 [19] demonstrated that a quasi two-dimensional high-mobility electron gas can be formed at the interface. This has been explained by a change in the valence state of the Ti ions at the interface due to the polar discontinuity existing between the two insulators. The polar discontinuity has been known in conventional semiconductor interfaces, where the interface cannot be abrupt between non-polar and polar materials [21]. In those cases, however, multivalent states are not available, unlike the case of the transition metal oxides, and electron or hole doping cannot be used instead of atomic rearrangements to remove the potential divergence. This oxide interface has become a central topic in solid-state physics at the present time, with many interesting physical properties revealed, such as nano-scale lithography [22] and interfacial controllable superconductivity [23].

In bulk, $SrTiO_3$ and $LaAlO_3$ are perovskite band insulators, whose band gaps are 3.2 eV and 5.6 eV respectively. They have similar lattice constants ($SrTiO_3$: 3.905 Å, $LaAlO_3$: 3.789 Å), so that epitaxial heterojunctions of the two materials can be realized, as shown in Fig. 1.4. In the {100} orientations, $SrTiO_3$ can be thought of as alternating neutral planes of $(SrO)^0$ and $(TiO_2)^0$, while $LaAlO_3$ consists of polar planes, $(LaO)^+$

and $(AlO_2)^-$.[1] Thus, two kinds of heterointerface, the $(LaO)^+/(TiO_2)^0$ interface, and the $(AlO_2)^-/(SrO)^0$ interface can be created, which have different characteristics according to the polar discontinuity picture, as shown in Fig. 1.5.

The unreconstructed interface has no net charges (ρ) in planes of $SrTiO_3$, but alternate charged layers exist in the planes of $LaAlO_3$. At the $(LaO)^+/(TiO_2)^0$ interface, this produces discontinuity, causing a divergence of the electron potential (V) for thick $LaAlO_3$ layers (Fig. 1.5 (a)). The potential divergence at the interface can be avoided when half an electron is added to the top Ti layer (Fig. 1.5 (b)). This interface, with electron doping is thus called the N-type interface. In the $(AlO_2)^-/(SrO)^0$ case, on the other hand, the potential diverges with the opposite sign (Fig. 1.5 (c)), and can thus be avoided by removing half an electron from the SrO plane (Fig. 1.5 (d)). This interface can be expected to be doped with holes, and is called the P-type interface. Experimentally, the N-type interface is found to be electron doped, and conducting as the theory proposed, but the P-type interface insulating. The N-type interface of the $LaAlO_3/SrTiO_3$ has been studied by many groups and found to have interesting properties. On the other hand, the P-type interface has barely been investigated, due to lack of the conduction. In Chap. 4, we will report some measurements of the photoconductivity properties of the P-type interface, in addition to similar characterization of the non-polar (110) interface.

The thickness of the conducting interface, has been a difficult question to address so far. It was shown that the thickness can be probed in cross-section by a conducting-tip atomic force microscope (CT-AFM) technique [24], as shown in Fig. 1.6. By this technique, a three dimensional-like broad carrier distribution in the $SrTiO_3$ side was obtained for an interface grown in low O_2 partial pressure, indicating the existence of a large amount of oxygen vacancies. However, with high O_2 pressure post-annealing, the thickness of the conducting layer was $\sim$ 7 nm, which is about same scale of the spacial resolution limit of CT-AFM, as shown in Fig. 1.6 (c). However in these types of measurements, the surface state compared to the bulk, and the pre-treatment of the sample before the AFM measurement gives some uncertainty about the reliability of these data.

Recently, a novel technique of using AFM lithography in the $LaAlO_3/SrTiO_3$ interface has attracted much intention. By this technique, the formation of nanometer scale wires is possible, together with reversible writing and erasing [22]. Figs. 1.7 (a-b) shows writing nanowire at the $LaAlO_3/SrTiO_3$ interface with an $LaAlO_3$ thickness of three unit cells,[2] applying a positive voltage to the interface. The technique has also been applied to create

[1] This is in an ideal ionic limit, and in fact there is probably some covalent character in the bonds, but this will only quantitatively, not qualitatively change the argument.

[2] Insulating, as grown, consistent with the critical thickness of 4 unit cells required for conductivity [25].

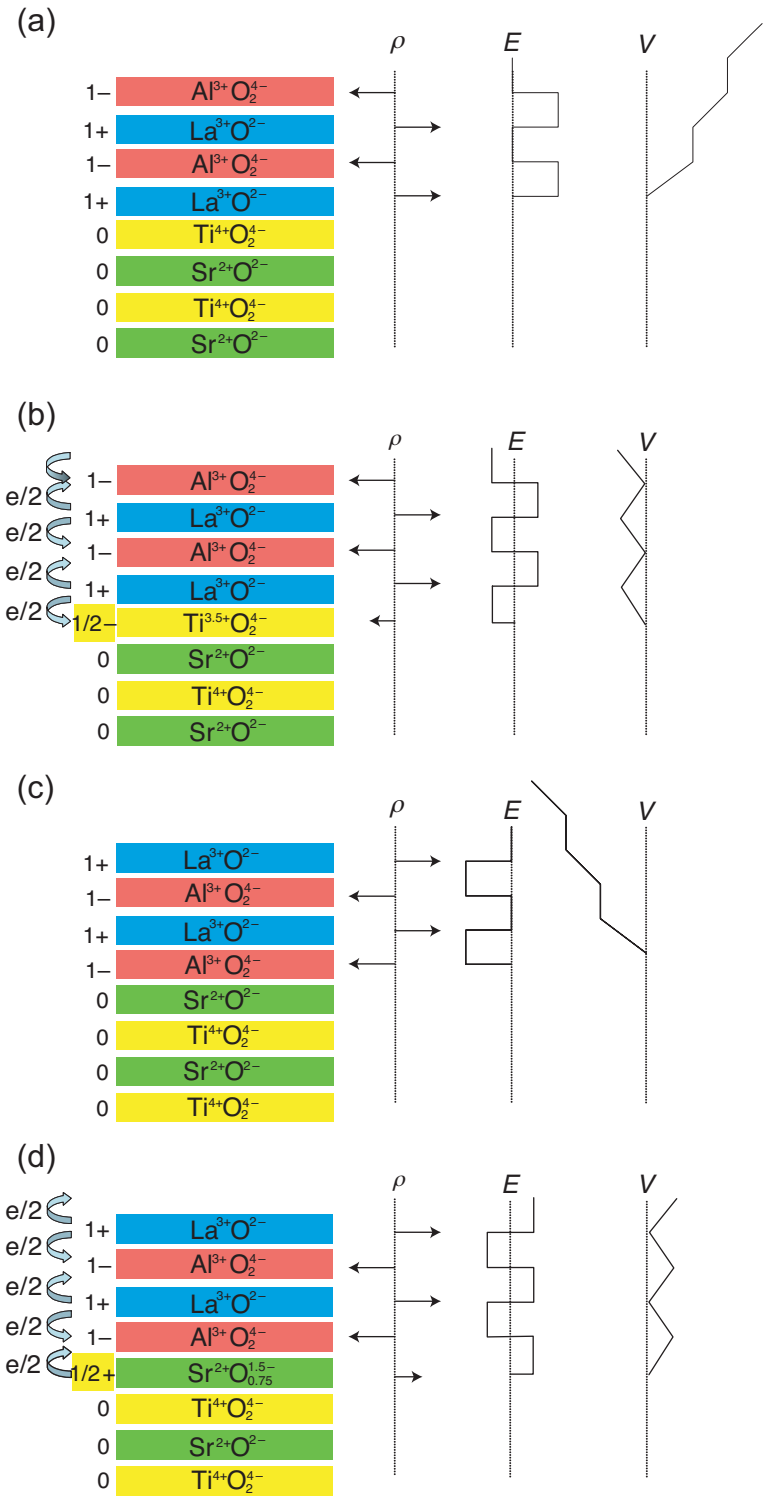

Figure 1.5: The polar discontinuity illustrated for the two types of $LaAlO_3/SrTiO_3$ interface, taken from N. Nakagawa *et al.* [26]. (a) The unreconstructed case of the $(LaO)^+/(TiO_2)^0$ (N-type) interface, causing the polar catastrophe. (b) The reconstructed case of the N-type interface by adding half an electron to the top Ti layer. (c) Negative potential divergence in the P-type interface. (d) Reconstructed P-type interface by removing half an electron from the SrO plane. Abbreviations in the figure: net charges (ρ), electric field (E) and electron potential (V) defined for positive test charges.

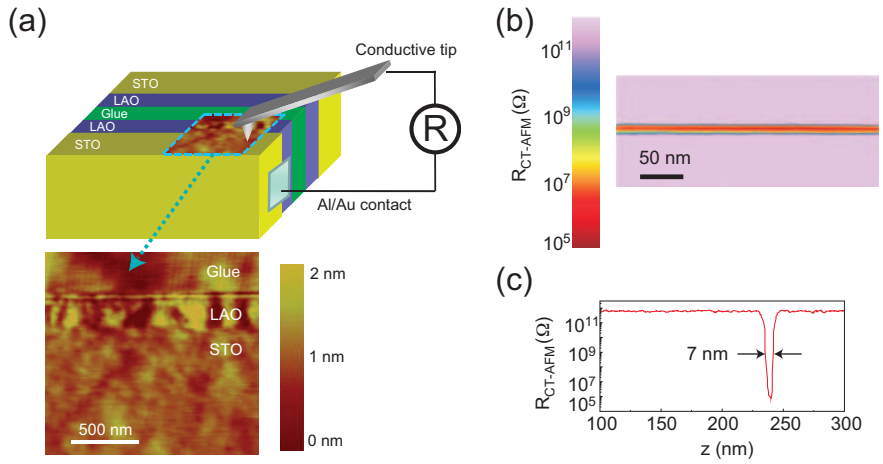

Figure 1.6: Mapping the spatial distribution of charge carriers in the $LaAlO_3/SrTiO_3$ interface, modified from M. Basletic *et al.* [24]. (a) Schematic diagram of a conducting-tip atomic force microscope (CT-AFM) experiment. As the tip is swept across the interface, the surface topography and the local resistance are mapped simultaneously. (b) CT-AFM resistance mapping. (c) Resistance profile across the $LaAlO_3/SrTiO_3$ interface extracted from (b).

further device structures with nanometer size, as shown in Figs. 1.7 (c-e).

Thus, several interesting properties are also found: the $LaAlO_3/SrTiO_3$ interface is found to be a superconductor [28]. The ground state can be controlled by a gate bias, and tuned through a quantum phase transition [23]. Some superconducting properties of the $LaAlO_3/SrTiO_3$ interface are shown in Fig. 1.8. The as grown transition temperature is found to be $\sim$ 200 mK, and showed characteristics of two-dimensional superconductivity (superconducting layer is thinner than the Ginzburg-Landau coherence length of the superconductor). In a two-dimensional superconductor, thermally excited of vortex-antivortex pairs control the transition. This is known as a Berezinskii-Kosterlitz-Thouless (BKT) transition. In the case of superconductivity at the $LaAlO_3/SrTiO_3$ interface, this transition was inferred from the characteristic broadening of the $R(T)$ transition, and scaling of the I-V curves, as shown in Fig. 1.8. The BKT transition will be discussed further in Sec. 5.5, and two-dimensional superconductivity in Chap. 5.

1.3.2 Field-Effect Transistors

The low-dimensional carriers can be induced by applying an electric field across a gate electrode to the surface. This is known as a Field-Effect Transistor (FET). The FET can tune the carrier density without introducing lattice disorder that is present in the case of chemical doping. Because many exotic phases in the oxides depend on the carrier density, this is an attractive carrier density tuning method [29]. For example, $SrTiO_3$ is

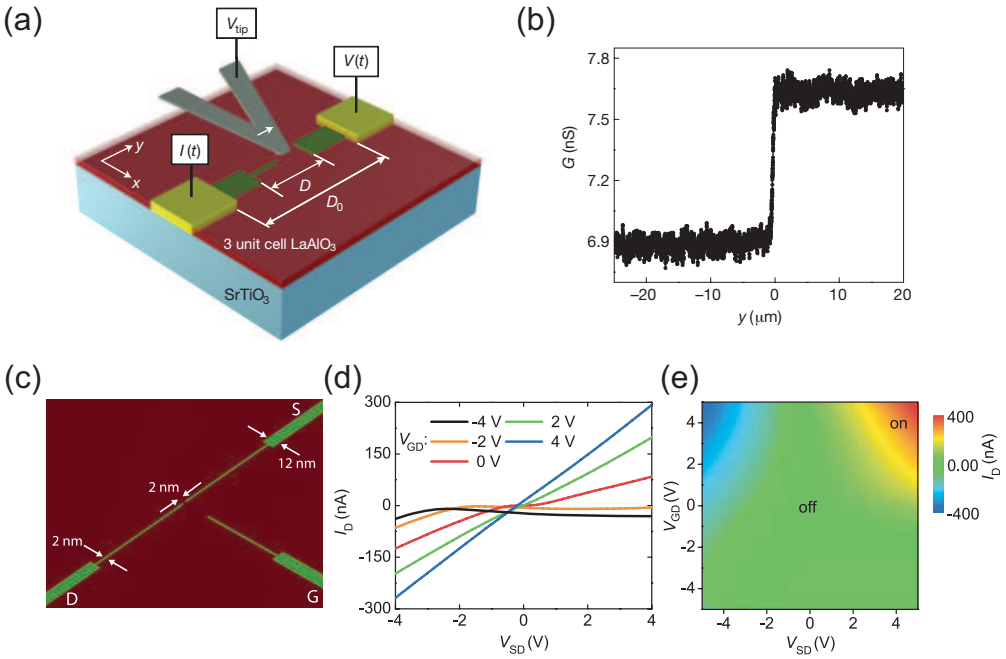

Figure 1.7: Writing nanowires and field-effect transistor (FET) devices at the $LaAlO_3/SrTiO_3$ interface, taken from C. Cen *et al.* [22,27]. (a) Schematic diagram of the writing process. (b) Conductance between the two electrodes measured as a function of the tip position while writing the wire. (c) Schematic diagram of the "SketchFET." S, source electrode; D, drain electrode; G, gate electrode. (d) I-V characteristic between source and drain for different gate biases V_{GD}. (e) Contour plot of I_{D} (V_{SD}, V_{GD}).

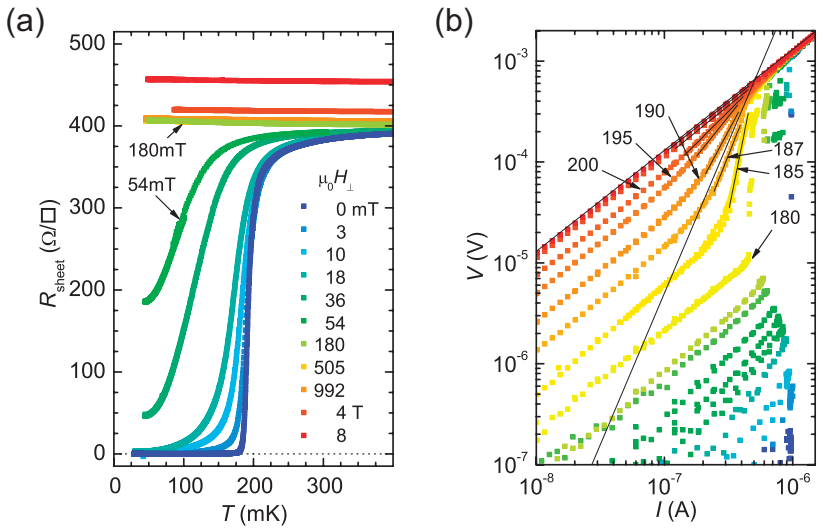

Figure 1.8: Superconducting properties of the $LaAlO_3/SrTiO_3$ interface, taken from N. Reyren *et al.* [28]. (a) Sheet resistance of the $LaAlO_3/SrTiO_3$ interface plotted as a function of T for various magnetic fields ($\mu_0 H_\perp$) applied perpendicular to the interface. (b) $V(I)$ curves on a logarithmic scale for various T from 30 mK to 300 mK. The numbers refers to mK, at which the curves were taken. The long black line corresponds to $V \sim I^3$ dependency.

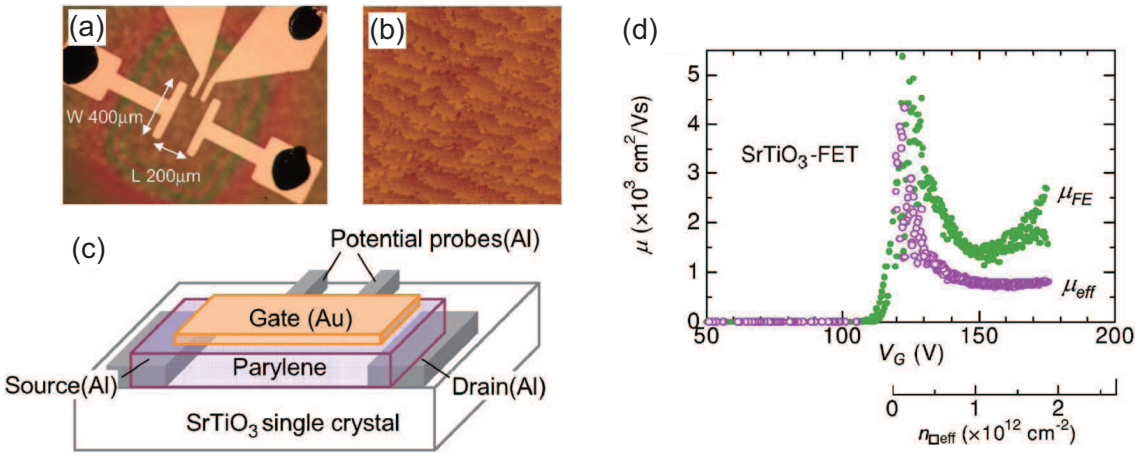

Figure 1.9: $SrTiO_3$ field-effect transistor (FET), taken from H. Nakamura *et al.* [30]. (a) Photograph of the $SrTiO_3$ FET device. (b) Image of the $SrTiO_3$ (100) surface taken by AFM before device fabrication. Displayed area is 2×2 μm. (c) Schematic diagram of the $SrTiO_3$ FET. (d) Mobility is plotted against the gate voltage V_G.

known as a superconducting semiconductor at low carrier concentrations between 10^{18} and 10^{19} cm^{-3}. Since this is an accessible range of electrostatic carrier doping, $SrTiO_3$ based FETs have been studied, aiming to control the superconducting state with a gate bias [30, 31].

One experimental difficulty is the decline of FET operation due to trap states at the gate-insulator/$SrTiO_3$ interface [32]. However, successful FET operation [30] with high-mobility (> 1000 cm^{2}V^{-1}s^{-1}) carriers at low temperatures has been achieved by adapting an organic polymer, parylene, as the gate insulator, as shown in Fig. 1.9. The large threshold voltage over 100 V, indicates a high density of traps (of order 10^{12} cm^{-2}) located at the $SrTiO_3$ surface. These trap states, which are also found at the $LaAlO_3/SrTiO_3$ interface, will be discussed in Chap. 4.

Another example is the Electric-Double-Layer (EDL) FET [31], shown in Fig. 1.10. In this case carrier doping up to 10^{14} cm^{-2} could be achieved by using an electrolyte as the gate insulator. A clear superconducting transition with transition temperature of $\sim$ 400 mK was found. A subband calculation using a triangular potential approximation estimated the thickness of the superconducting layer as $\sim$ 16 nm, which is smaller than the superconducting coherence length of the system, $\sim$ 50 nm, meaning this is a two-dimensional superconductor. This result is a good reference for the two-dimensional superconductivity realized in $SrTiO_3$, which will be discussed in Chap. 5.

Although the FET is a useful technique to control the carrier concentration of a film after the growth, it is beyond the scope of this Thesis. However, many results seen in these systems are closely related. We will discuss these similarities and differences

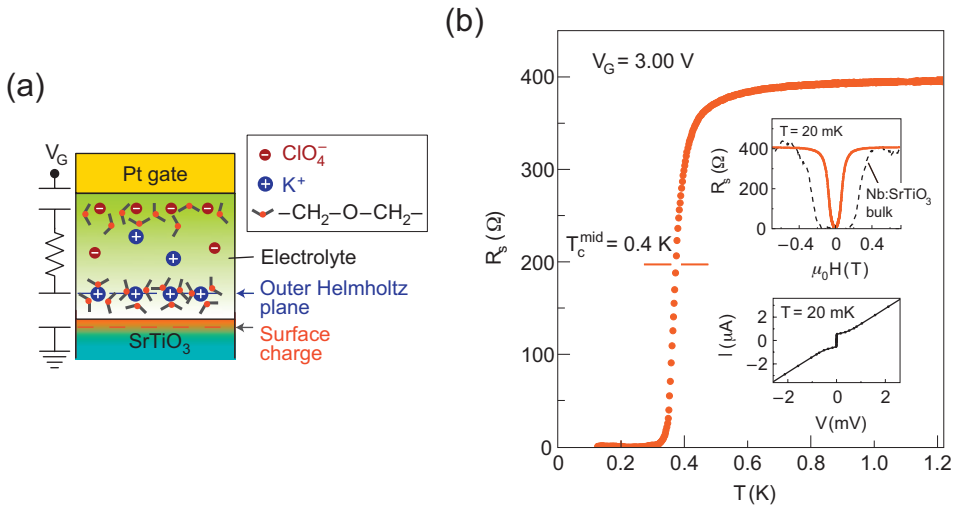

Figure 1.10: $SrTiO_3$ electric-double-layer (EDL) FET, taken from K. Ueno *et al.* [31]. (a) Schematic diagram of an EDL formed at an electrolyte/$SrTiO_3$ interface. By applying a positive gate bias, cations (K^+) in the electrolyte are adsorbed on the $SrTiO_3$ surface. A negative charge is induced in the $SrTiO_3$ surface layer, forming an EDL capacitor. (b) T dependence of R_s. The dashed line denotes the mid-point of the superconducting transition. The upper inset is the magnetic-field ($\mu_0 H$) dependence of R_s with a reference of a 0.2% at. Nb:$SrTiO_3$ bulk single crystal (dotted line, normalized) at 20 mK. The lower inset is the I-V curve at 20 mK.

throughout the Thesis.

1.3.3 Delta-Doping Technique

Delta-doping means the selective growth of the dopant atoms in a narrow region whose thickness is smaller than the other characteristic length scales in the system. Precise control of the doping region is feasible for the design of various complex heterostructures, for example delta-doped superlattices and selectively delta-doped structures. This can lead to emergent physical properties in oxide heterostructure: for example atomic-scale $LaTiO_3/SrTiO_3$ superlattices, reproduced in Fig. 1.11 (a), shows an increased spatial distribution of the extra electrons on the titanium sites [33]. Also superconductivity in a one unit cell layer of selectively doped copper-oxide was reported [34], as shown in Fig. 1.11 (b). Despite their novel properties due to monolayer doping, however, the other relevant length scales are also close to the lattice constant in these systems due to the high carrier density [35]. This highlights the strong constraint due to the material properties in the search for two-dimensional physics.

The two-dimensional confinement of electrons with well-resolved quantization of energy levels has been studied in conventional semiconductors [36, 37], where the typical carrier density is a few orders of magnitude lower than that of the oxides. Fig. 1.12 (a)

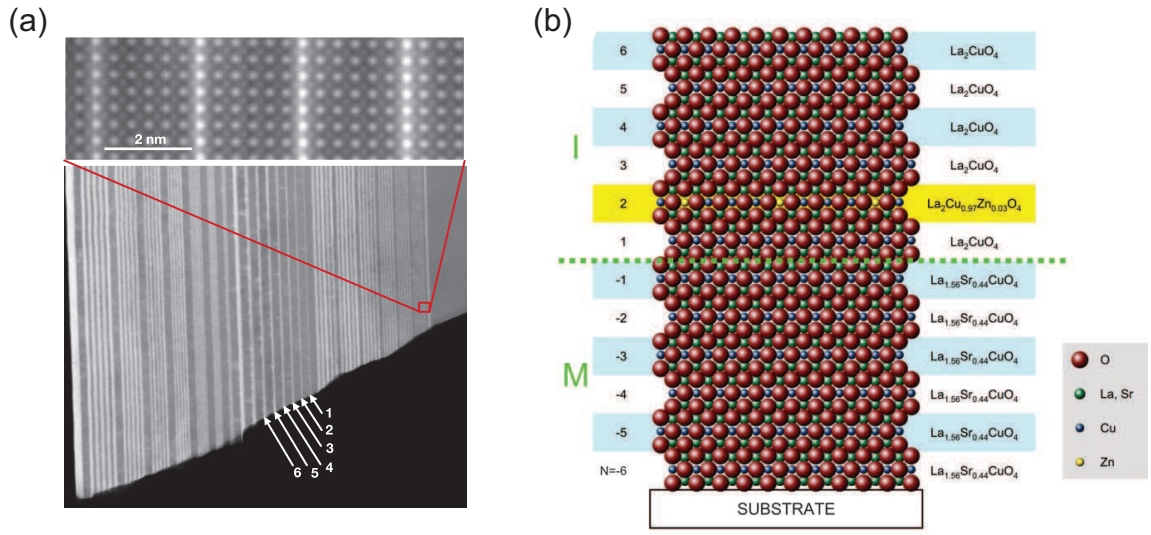

Figure 1.11: Delta-doped systems in oxides. (a) High-angle annular dark-field image of $LaTiO_3$ layers (bright areas) of varying thickness spaced by $SrTiO_3$ layers. The top part shows an enlarged view of a section of the image, with repetition of 1 unit cell of $LaTiO_3$ and 5 unit cells of $SrTiO_3$, taken from A. Ohtomo *et al.* [33]. (b) Schematic diagram of delta-doping in the cuprates. The green letters I, M refer to insulator and metal. Zn atoms are delta-doped at the N = 2 CuO_2 plane, taken from G. Logvenov *et al.* [34].

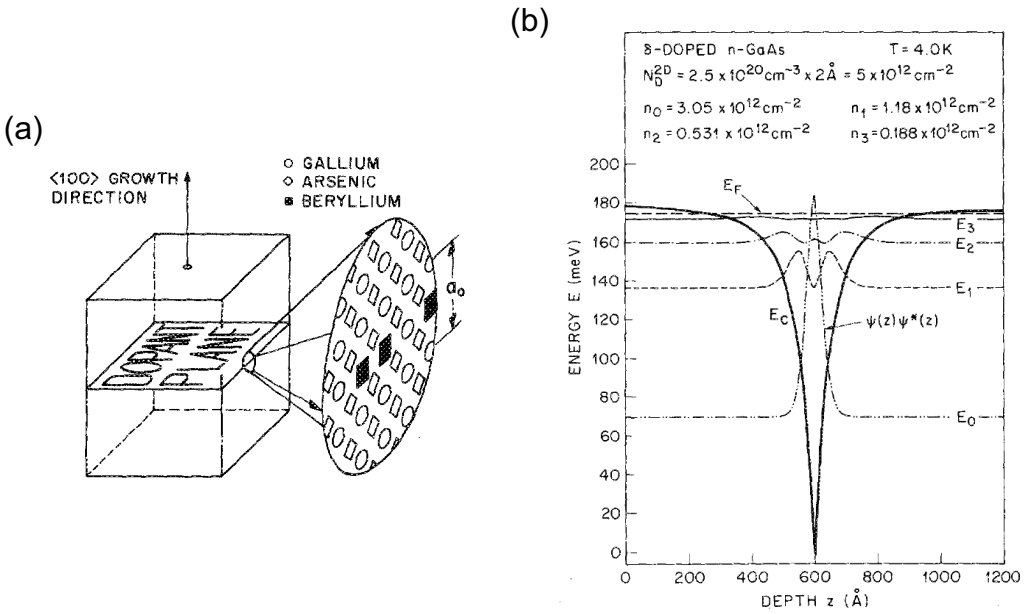

Figure 1.12: Schematic diagram of delta-doping in GaAs, taken from E. F. Schubert [36]. (a) Schematic illustration of a semiconductor grown along the <100> direction containing Be impurities in a single Ga plane of the GaAs zincblende structure. (b) Charge distribution in a delta-doped potential well obtained from a self-consistent solution of Poisson's and Schrodinger's equations, at a doping density of 5×10^{12} cm^{-2}.

shows previous literature where Be atoms were delta-doped in the GaAs host material. The carriers are likely to migrate away from their dopants due to diffusion. In a classical picture, electrostatic attraction occurs between carriers and dopants, which balances the diffusive motion in the equilibrium state. In the quantum regime, this can be fully understood by considering the electron wavefunctions confined by the Coulomb potential of the donor plane. The electron distribution in the well was calculated self-consistently solving Poisson's and Schrodinger's equations, as shown in Fig. 1.12 (b). The electronic structure of delta-doped systems is found to be rather unaffected by the width of the doping distribution, as long as the spread of dopants is smaller than the spatial extent of the ground-state wave function.

Delta-doping has been studied mainly for delta-doped FET structures, where large transconductance is expected. Several other features are revealed as follows:

- Large carrier concentration doped within a thin region is possible, which may crucial for inducing superconductivity and strongly correlated phenomena.
- High-mobility carriers can exist because the electron wavefunction spreads out of the dopant layer [38]. The outer part of the wavefunction suffers less scattering from the dopants. Thus, the mobility can be enhanced, compared to the homogeneously doped system with the same dopant density.

As will be discussed in Chaps. 5 and 6, delta-doping is a fascinating technique for $SrTiO_3$. Firstly, $SrTiO_3$ has the lowest known carrier density to show superconductivity. With delta-doping in a thin region, the delta-doped superconductor is expected to show novel properties (Chap. 5). Secondly, the high-mobility electrons confined in two-dimensional delta-doped layer can show quantum transport effects such as Shubnikov-de Haas oscillations (Chap. 6). One of the merits of delta-doping is that the electrons are located in an essentially continuous host material without an obvious surface or interface, unlike the FET and heterointerface structures mentioned above, where electrons can be scattered diffusively and loose coherence. From these features, it may be possible to demonstrate the interplay between superconductivity and quantum oscillations in a cleaner $SrTiO_3$ heterostructures, where novel physical properties may occur.

References

[1] G. E. Moore, Cramming More Components onto Integrated Circuits, *Electronics* **38**, 114 (1965).

[2] P. S. Peercy, The Drive to Miniaturization, *Nature* **406**, 1023 (2000).

[3] International Technology Roadmap for Semiconductors, *2007 Edition Executive Summary*, (ITRS, 2007). Available on-line at http://www.itrs.net.

[4] M. Imada, A. Fujimori, and Y. Tokura, Metal-Insulator Transitions, *Rev. Mod. Phys.* **70**, 1039 (1998).

[5] N. F. Mott, *Metal-Insulator Transitions*, (Taylor and Francis, London/Philadelphia, 1990).

[6] S. Jin, T. H. Tiefel, M. McCormack, R. A. Fastnacht, R. Ramesh, and L. H. Chen, Thousandfold Change in Resistivity in Magnetoresistive La - Ca - Mn - O Films, *Science* **264**, 5157 (1994).

[7] J. G. Bednorz and K. A. Muller, Possible High T_c Superconductivity in the Ba - La - Cu - O System, *Z. Phys. B.* **64**, 189 (1986).

[8] J. G. Bednorz and K. A. Muller, Perovskite-Type Oxides - the New Approach to High-T_c Superconductivity, Nobel Lecture, December 8, 1987.

[9] M. Cardona, Optical Properties and Band Structure of $SrTiO_3$ and $BaTiO_3$, *Phys. Rev.* **140**, A651 (1965).

[10] C. S. Koonce, M. L. Cohen, J. F. Schooley, W. R. Hosler, and E. R. Pferifer, Superconducting Transition Temperatures of Semiconducting $SrTiO_3$, *Phys. Rev.* **163**, 380 (1967).

[11] M. A. Saifi and L. E. Cross, Dielectric Properties of Strontium Titanate at Low Temperature, *Phys. Rev. B* **2**, 677 (1970).

[12] T. Sakudo and H. Unoki, Dielectric Properties of $SrTiO_3$ at Low Temperatures, *Phys. Rev. Lett.* **26**, 851 (1971).

[13] K. A. Muller and H. Burkard, $SrTiO_3$: An Intrinsic Quantum Paraelectric below 4 K, *Phys. Rev. B* **19**, 3593 (1979).

[14] O. N. Tufte, and P. W. Chapman, Electron Mobility in Semiconducting Strontium Titanate, *Phys. Rev.* **155**, 796 (1966).

[15] H. Uwe, R. Yoshizaki, T. Sakudo, A. Izumi, and T. Uzumaki, Conduction Band Structure of $SrTiO_3$, *Jpn. J. Appl. Phys.* **24S2**, 335 (1985).

[16] T. Ando, A. B. Fowler, and F. Stern, Electronic Properties of Two-Dimensional Systems, *Rev. Mod. Phys.* **54**, 437 (1982).

[17] M. Rasolt and Z. Tesanovic, Theoretical Aspects of Superconductivity in Very High Magnetic Fields, *Rev. Mod. Phys.* **64**, 709 (1992).

[18] P. W. Anderson, Interlayer Tunneling Mechanism for High-T_c Superconductivity: Comparison with c Axis Infrared Experiments, *Science* **268**, 1154 (1995).

[19] A. Ohtomo and H. Y. Hwang, A High-Mobility Electron Gas at the $LaAlO_3/SrTiO_3$ Heterointerface, *Nature* **427**, 423 (2004).

[20] J. Heber, Materials Science: Enter the Oxides, *Nature* **459**, 28 (2009).

[21] W. A. Harrison, E. A. Kraut, J. R. Waldrop, and R. W. Grant, Polar Heterojunction Interfaces, *Phys. Rev. B* **18**, 4402 (1978).

[22] C. Cen, S. Thiel, G. Hammerl, C. W. Schneider, K. E. Andersen, C. S. Hellberg, J. Mannhart, and J. Levy, Nanoscale Control of an Interfacial Metal-Insulator Transition at Room Temperature, *Nature Mater.* **7**, 298 (2008).

[23] A. D. Caviglia, S. Gariglio, N. Reyren, D. Jaccard, T. Schneider, M. Gabay, S. Thiel, G. Hammerl, J. Mannhart, and J. -M. Triscone, Electric Field Control of the $LaAlO_3/SrTiO_3$ Interface Ground State, *Nature* **456**, 624 (2008).

[24] M. Basletic, J. -L. Maurice, C. Carretero, G. Herranz, O. Copie, M. Bibes, E. Jacquet, K. Bouzehouane, S. Fusil, and A. Barthelemy, Mapping the Spatial Distribution of Charge Carriers in $LaAlO_3/SrTiO_3$ Heterostructures, *Nature Mater.* **7**, 621 (2008).

[25] S .Thiel, G. Hammarl, A. Schmehl, C. W. Schneider, and J. Mannhart, Tunable Quasi-Two-Dimensional Electron Gases in Oxide Heterostructures, *Science* **313**, 1942 (2006).

[26] N. Nakagawa, H. Y. Hwang, and D. A. Muller, Why Some Interfaces Cannot be Sharp, *Nature Mater.* **5**, 204 (2006).

[27] C. Cen, S. Thiel, J. Mannhart, and J. Levy, Oxide Nanoelectronics on Demand, *Science* **323**, 1026 (2009).

[28] N. Reyren, S. Thiel, A. D. Caviglia, L. Fitting Kourkoutis, G. Hammerl, C. Richter, C. W. Schneider, T. Kopp, A. -S. Ruetschi, D. Jaccard, M. Gabay, D. A. Muller, J. -M. Triscone, and J. Mannhart, Superconducting Interfaces Between Insulating Oxides, *Science* **317**, 1196 (2007).

[29] C. H. Ahn, J. -M. Triscone, and J. Mannhart, Electric Field Effect in Correlated Oxide Systems, *Nature* **424**, 1015 (2003).

[30] H. Nakamura, H. Takagi, I. H. Inoue, Y. Takahashi, T. Hasegawa, and Y. Tokura, Low Temperature Metallic State Induced by Electrostatic Carrier Doping of $SrTiO_3$, *Appl. Phys. Lett.* **89**, 133504 (2006).

[31] K. Ueno, S. Nakamura, H. Shimotani, A. Ohtomo, N. Kimura, T. Nojima, H. Aoki, Y. Iwasa, and M. Kawasaki, Electric-Field-Induced Superconductivity in an Insulator, *Nature Mater.* **7**, 855 (2008).

[32] K. Ueno, I. H. Inoue, H. Akoh, M. Kawasaki, Y. Tokura, and H. Takagi, Field-Effect Transistor on $SrTiO_3$ with Sputtered Al_2O_3 Gate Insulator, *Appl. Phys. Lett.* **83**, 1755 (2003).

[33] A. Ohtomo, D. A. Muller, J. L. Grazul, and H. Y. Hwang, Artificial Charge-Modulation in Atomic-Scale Perovskite Titanate Superlattices, *Nature* **419**, 378 (2002).

[34] G. Logvenov, A. Gozar, and I. Bozovic, High-Temperature Superconductivity in a Single Copper-Oxygen Plane, *Science* **326**, 699 (2009).

[35] H. Y. Hwang, Atomic Control of the Electronic Structure at Complex Oxide Heterointerfaces, *MRS Bulletin* **31**, 28 (2006).

[36] E. F. Schubert, Delta Doping of III-V Compound Semiconductors: Fundamentals and Device Applications, *J. Vac. Sci. Technol. A* **8**, 2980 (1990).

[37] E. F. Schubert, *Delta-Doping of Semiconductors*, (Cambridge Univ. Press, Cambridge, 1996).

[38] H. -J. Gossmann and F. C. Unterwald, Dopant Electrical Activity and Majority-Carrier Mobility in B- and Sb-δ-doped Si thin films, *Phys. Rev. B* **19**, 12618 (1992).

Chapter 2

Scope of the Research

The motivation of this Thesis is to investigate the low-dimensional electronic properties of oxide heterostructures. Two systems are chosen, namely, the $LaAlO_3/SrTiO_3$ heterointerface and $SrTiO_3/Nb{:}SrTiO_3/SrTiO_3$ heterostructures. These different structures are shown schematically in Fig. 2.1. The scope of the research is explained briefly below.

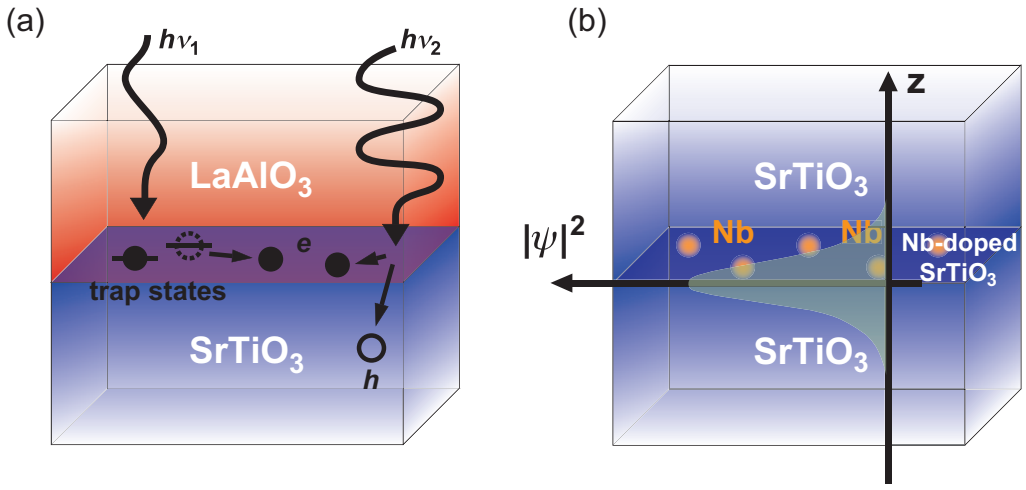

Figure 2.1: Schematic diagrams of two types of low-dimensional systems based on oxide heterostructures. (a) The $LaAlO_3/SrTiO_3$ heterointerface. (b) The $SrTiO_3/Nb{:}SrTiO_3/SrTiO_3$ heterostructure with a thin layer of $Nb{:}SrTiO_3$.

1. **Properties of photo-induced carriers at insulating $LaAlO_3/SrTiO_3$ interfaces.**

   At the $LaAlO_3/SrTiO_3$ interface, the interfacial properties can be changed drastically depending on the interface-termination. From the viewpoint of understanding termination control, the insulating P-type and (110) $LaAlO_3/SrTIO_3$ interfaces are as important as the conducting N-type interface. We will investigate the physical properties of these two interfaces by inducing photocarriers at the interface and

measuring their transport properties. Through investigating the electronic states of the interfaces, we aim to clarify the existence of interfacial states in these systems.

2. **Superconducting properties of $SrTiO_3$/Nb:$SrTiO_3$/$SrTiO_3$ heterostructures.**

   The superconducting properties of electron-doped $SrTiO_3$ are of great interest because of its low carrier density. However, confining the superconducting layers to the nanometer scale has been extremely challenging. We will investigate the superconducting properties of $SrTiO_3$/Nb:$SrTiO_3$/$SrTiO_3$ heterostructures. As the thickness of the Nb:$SrTiO_3$ layer is reduced, we can expect a crossover of the superconductivity from three dimensional to two dimensional.

3. **Normal-state transport properties of $SrTiO_3$/Nb:$SrTiO_3$/$SrTiO_3$ heterostructures.**

   It is known that surface or interface scattering can prevent the electrons from showing quantum oscillations. When the doped layer in the $SrTiO_3$/Nb:$SrTiO_3$/$SrTiO_3$ heterostructure is reduced to a few atomic planes, similar to the delta-doped structure in conventional semiconductors, a cleaner two-dimensional system can be made, free from the above scattering mechanisms. We will investigate the low-temperature electronic transport properties in delta-doped $SrTiO_3$ heterostructures which are expected to show two-dimensional quantum oscillations in the high magnetic field regime.

Chapter 3

Equipment and Methods

3.1 Pulsed Laser Deposition

Pulsed laser deposition (PLD) is conceptually a simple the thin film growth techniques. Fig. 3.1 shows a schematic diagram of the experimental setup used to fabricate all of the samples in this thesis. Films are deposited in an ultra high vacuum chamber by ablating a bulk target using an ultraviolet pulsed laser. When the laser radiation is absorbed by the target, a thin layer of the material is evaporated forming a plume via a complex laser-target interaction. The plume rapidly expands into the vacuum and the evaporated particles are crystallized on the substrate. This process has many advantages, including flexibility of the target material, as well as disadvantages such as the presence in some cases of micron-sized particulates, and a difficulty of large-area growth. With the appropriate choice of laser condition and other parameters such as temperature, substrate-target distance, gas pressure during growth, PLD is a versatile method to grow thin films of any kind of material, including complex oxide thin films.

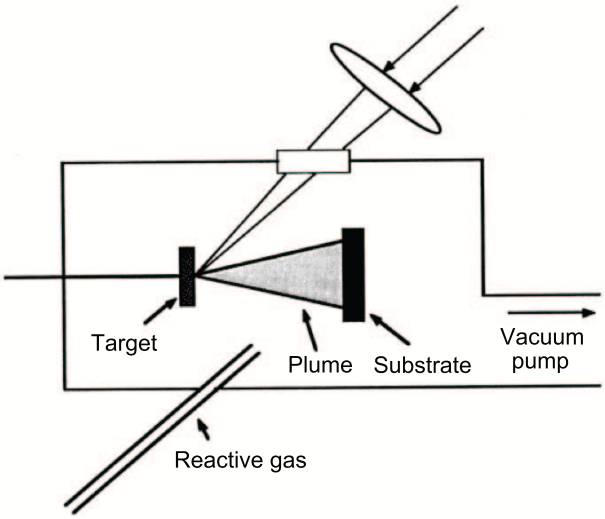

Figure 3.1: Schematic diagram of a plused laser deposition apparatus, modified from [1].

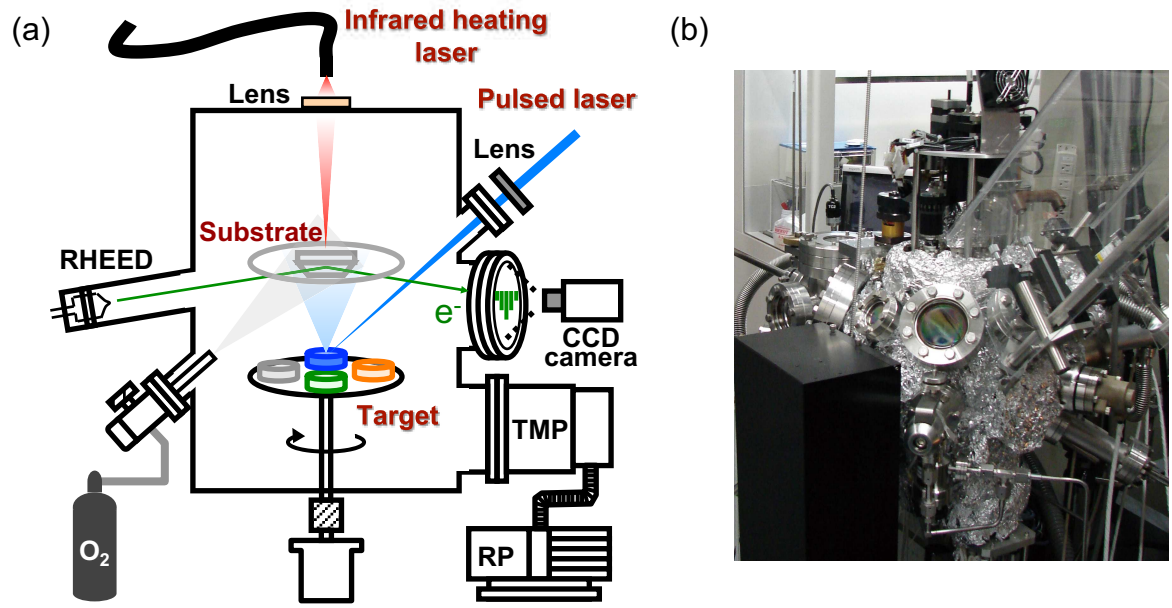

Figure 3.2: (a) Schematic diagram of the growth chamber (courtesy of Y. Kozuka). (b) Photograph of the chamber.

Two chamber systems are used in this research, each has a different heating method of the substrate: a lamp heater for the $LaAlO_3/SrTiO_3$ samples discussed in Chap. 4 and infrared laser heating for the Nb doped $SrTiO_3$ samples discussed in Chap. 5 and 6. The main characteristics of the two chambers are similar, thus the chamber with infrared laser heating is discussed below, as shown in Fig. 3.2. The main chamber is evacuated by a turbo molecular pump to a base pressure of around 10^{-8} Torr. The temperature of the substrate is varied by the output of the heating infrared laser, reaching a maximum temperature of 1300 °C. A graphite plate is used as the substrate holder, with the sample fixed by Inconel wire. The temperature of the substrate is measured by an optical pyrometer located outside of the chamber. The oxygen pressure inside the main chamber is manually controlled by a needle valve and the chamber pressure is measured by an ion gauge. A pulsed KrF excimer laser is used for ablation of the target with a wavelength of 248 nm and a pulse duration time of $\sim$ 25 ns. The repetition rate of the laser is in the range of 1 - 10 Hz, but is typically 5 Hz for the samples grown in this thesis. Reflection High-Energy Electron Diffraction (RHEED) is used to monitor the film growth *in-situ*, which will be discussed in Sec. 3.1.1.

3.1.1 Reflection High-Energy Electron Diffraction

Reflection High-Energy Electron Diffraction (RHEED) is widely used for surface structural analysis and *in-situ* monitoring of epitaxial growth because it can provide informa-

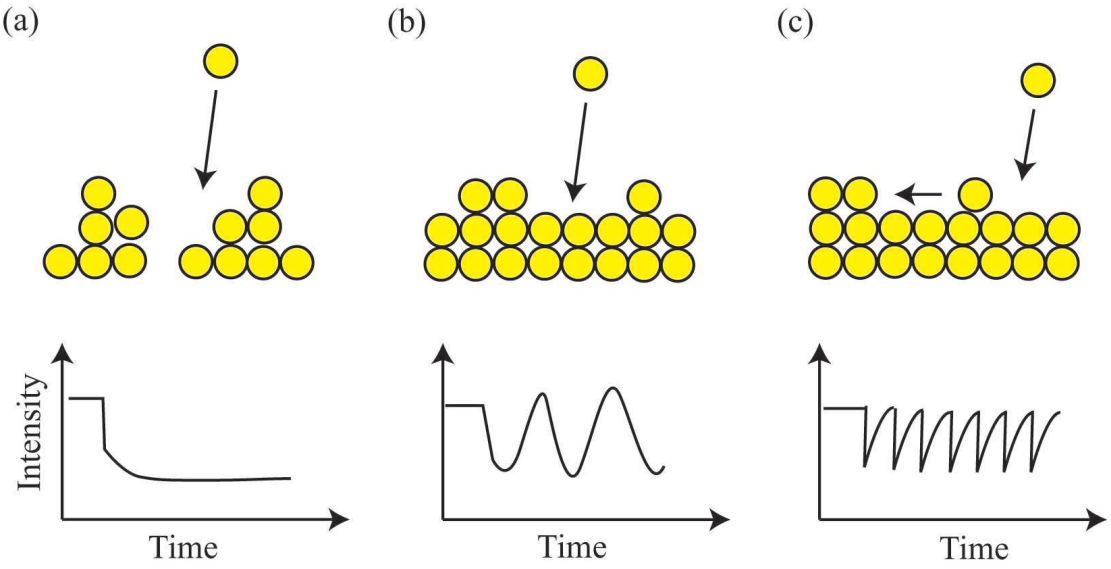

Figure 3.3: Different schematic traces of RHEED intensity (courtesy of Y. Kozuka). (a) Three-dimensional growth mode. (b) Layer-by-layer growth mode. (c) Step-flow growth mode.

tion about the morphology of the topmost surface layer. As shown in Fig. 3.2 (a), the electron beam is irradiated with a kinetic energy of a few tens of kV, and reflected at the sample surface and forms a diffraction pattern on the phosphor screen located inside the chamber. The intensity of these bright regions on the screen is monitored in real time by a CCD camera outside of the chamber. Similar to bulk x-ray diffraction, the points in the reflection pattern arise when the Ewald sphere intersects the reciprocal wave vector. It should be noted that in the case of RHEED, the points become vertical streaks because of the two dimensional diffraction [2].

Depending on the growth mode of the thin films, the trace of the RHEED pattern with time can be divided into three basic types as shown in Fig. 3.3. When the growth is three-dimensional, the intensity decreases because the roughness of the sample surface rapidly increases, and the scattering of the electron beam is increased. In the layer-by-layer growth mode, the percent coverage of the growing layer changes from 0 to 100 % periodically during growth. Thus the intensity oscillation corresponds to the surface coverage of the deposited material: at 50 % coverage, there is maximum electron scattering, and the RHEED intensity is minimum. In this growth mode, the number of grown layers can be known simply by counting the number of RHEED oscillations. Finally, in the step-flow mode, the intensity is reduced after each laser pulse, but recovers as the atoms move from the terrace to the step faces.

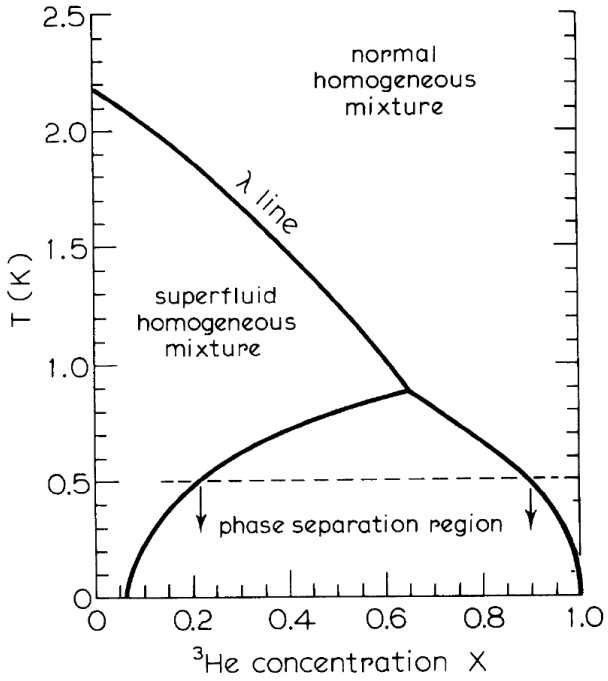

Figure 3.4: Phase diagram of the ^{3}He-^{4}He mixture, taken from D. S. Betts [3].

3.2 Dilution Refrigerator

The dilution refrigerator is a popular method of cooling in the mK temperature range due to the fact that the cooling process can be made to run continuously in contrast to, for example, adiabatic demagnetization. The cooling power at low temperatures can be sufficiently large for electrical measurements to be possible [4]. The cooling mechanism of the dilution refrigerator is intimately related to the physical properties of ^{3}He and ^{4}He, well-known for their superfluid properties. The principle of the dilution refrigerator was put forward by H. London [5] in 1951 and developed to its present form by H. London *et al.* [6] in 1962. London suggested to make use of the expansion of ^{3}He when diluted with ^{4}He. Due to the entropy of mixing of ^{3}He and ^{4}He at low temperatures, cooling down to the mK region would be possible.

Fig. 3.4 shows a phase diagram of the ^{3}He-^{4}He mixture. When a mixture of the two isotopes of He is cooled below the critical temperature, it separates into two phases. The arrow on the right of Fig. 3.4 indicates the concentrated phase, which is rich in ^{3}He, and the arrow on the left shows the dilute phase, which is ^{4}He rich. The cooling effect is provided by the evaporation of ^{3}He from the concentrated phase into the dilute phase in order to match the enthalpy difference of the ^{3}He in the two phases. The process can be maintained at low temperatures because the ^{3}He concentration in the dilute phase is 6.6 % at 0 K, and a finite cooling power can be obtained even approaching 0 K. One

can derive the cooling power from the calculation of enthalpy balance in the mixing chamber [7]. The dilution refrigerator used in this work is an Oxford Kelvinox MX400, which has a cooling power of ~ 400 μW at 100 mK, and a base temperature of ~ 10 mK, as calibrated by a nuclear orientation thermometer.

A schematic diagram of the dilution refrigerator is shown in Fig. 3.5. In order that the process be continous, ^{3}He must be removed from the dilute phase in the still and returned to the concentrated phase in the mixing chamber. Conventional room-temperature pumping can remove ^{3}He preferentially from the liquid surface in the still because the vapor pressure of ^{3}He is much higher than that of ^{4}He. After ^{3}He is removed, it is returned to the refrigerator via a gas handling system, using liquid N_2 and liquid He cold traps for impurity filtering. The inflowing gas is cooled by the liquid He bath down to 4.2 K and condensed by the 1 K pot. A primary and a secondary impedance in the form of a capillary tube are used to maintain a sufficiently high pressure such that the gas is condensed fully by the 1 K pot. Before enter the mixing chamber, because phase separation occurs only below the tri-critical point at 0.86 K, additional cooling is provided by the heat exchanger connected to the still, where evaporation of ^{3}He occurs so that it can be cooled down to 0.7 K. It is important that the ^{3}He concentration and volume of the mixture are chosen correctly, so that the phase boundary occurs inside the mixing chamber and the liquid surface lies in the still. The experimental apparatus is connected to the copper plate where the mixing chamber is mounted ensuring sufficient thermal contact.

In Chap. 5 and 6, we will discuss the low temperature measurements using the dilution refrigerator. Despite the low base temperature of the system and high cooling power, the small heat capacity of superconducting thin film samples is known to cause problems in effectively cooling the electrons in the system significantly below 60 mK [8]. This we also find in our samples. Also, for the rotation experiments (see Secs. 5.3 and 6.4), and applying a magnetic field, care must be taken that the sample and mixing chamber are not warmed by friction in the case of rotation and eddy current heating for changing the magnetic field. For the latter case, the magnetic field ramp rate was kept below 0.05 mT/min for all measurements, which was found not to cause significant heating at 50 mK. For the rotation experiments, a RuO_2 thermometer was placed next to the sample in the rotating holder, and was used to calibrate the local temperature. Despite the fast cooling rate of the mixing chamber after rotation, it was found that even for small rotations of ~ 0.1 °, a waiting time of 3 hours was needed to cool back to 50 mK inside the rotating holder.

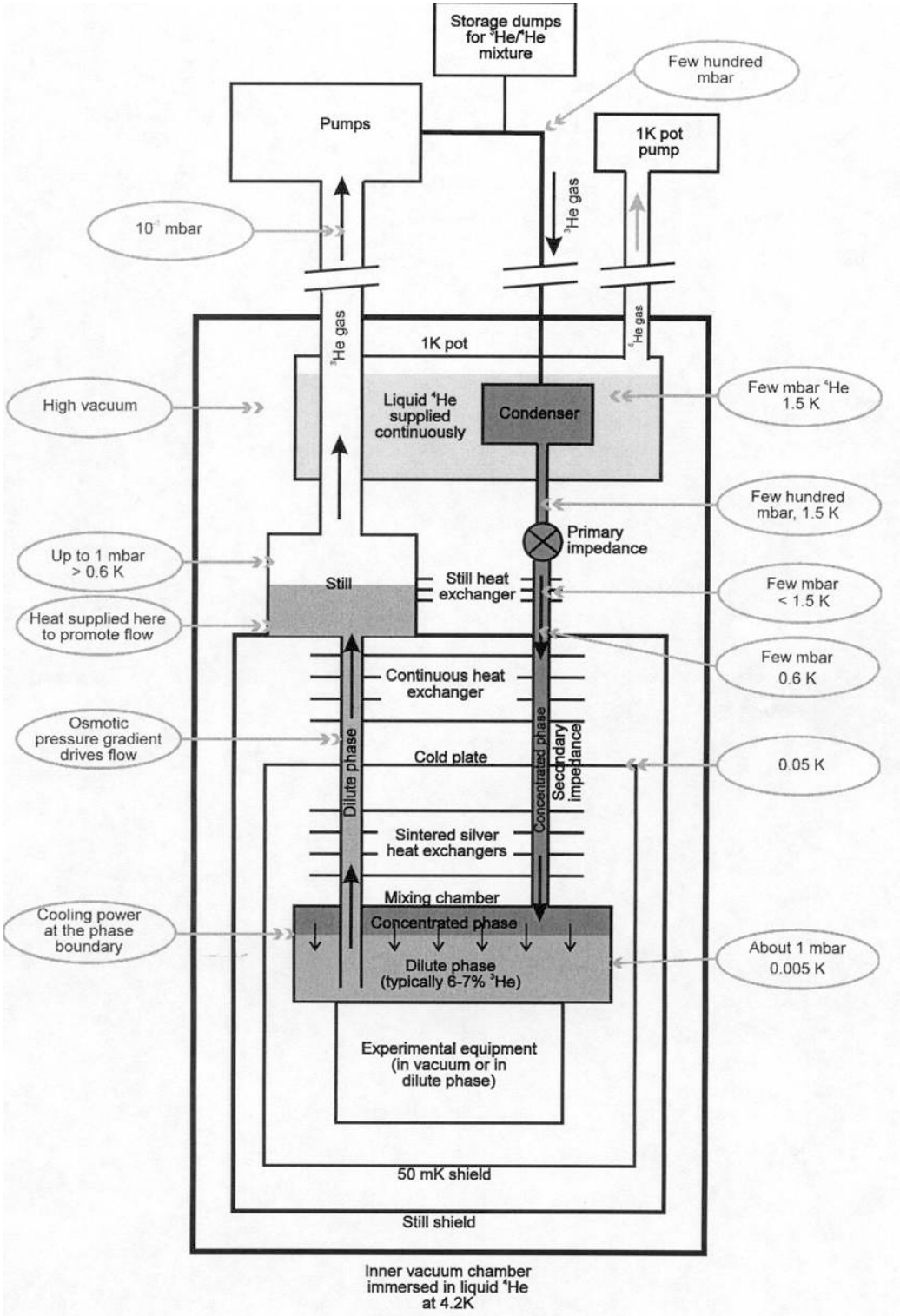

Figure 3.5: Schematic diagram of a dilution refrigerator taken from the operator's handbook of Oxford Instruments.

3.3 Optics and Photoconductivity Measurement

Photoconductivity at the $LaAlO_3/SrTiO_3$ interface, which will be discussed in Chap. 4, is measured using two different systems. The first system is a Halogen lamp with a grating monochromater, and is shown schematically in Fig. 3.6 (a). It can irradiate a wide range of wavelengths of light from 1800 nm ($E_{\text{photon}} = 0.69$ eV) to 300 nm ($E_{\text{photon}} = 4.14$ eV) with an intensity of ~ 1 μW/mm^2. The intensity has a wavelength dependence and becomes very weak below 380 nm as shown in Fig. 3.7. The sample is placed in a cryostat equipped with a 14 T superconducting magnet (PPMS, Quantum Design Co.), and a base temperature of 2 K. The light is guided through optical fibers to the sample mounted at the bottom of the home-made probe. The lowest temperature it can achieve is restricted to 10 K due to the increased heat load of the probe. During light irradiation, the d.c. photocurrent is measured by using an electrometer (Model 6517, Keithley Co.) under a d.c. bias voltage applied via a voltage source (Model 7651, Yokoyama Co.). An electromagnetically controlled shutter (Model F77-4, Suruga seiki Co.) with a maximum switching time of 8 ms was used to switch the light on and off. In the measurement of highly resistive samples, a proper choice of the cable and the connections between the various equipment played an important role in reducing the external noise [9]. Here, several treatments were used in order to reduce the background current noise level $<$ pA as follows. To reduce the thermo-electric noise of the probe, co-axial cable was installed between the sample and the connector at the upper part of the probe, instead of twisted pairs. In order to shield noise caused by electro-magnetic interference, the connections between the coax cable from the probe and the three lug of the tri-axial cable from the electrometer was made inside a mu-metal box, where the inner shielding box of the mu-metal box was connected to the ground of the electrometer.

The second set up is a Xe lamp with band-pass filters as shown in Fig. 3.6 (b). This can irradiate in the ultraviolet region from 380 nm ($E_{\text{photon}} = 3.26$ eV) to 300 nm ($E_{\text{photon}} = 4.14$ eV) with a maximum intensity ~ 10 μW/mm^2, which is much higher than the intensity of the Halogen lamp. The light is irradiated to the sample via a fiber bundle. Because the sample puck and the probe are disconnected, there is no loss of cooling power and the lowest temperature of the sample is 2 K in this case, limited only by the PPMS. Since the resistance of the photo-induced sample, which will be discussed in Sec. 4.4, is < 1 kΩ, the PPMS resistance bridge was also used to make Hall effect measurements.

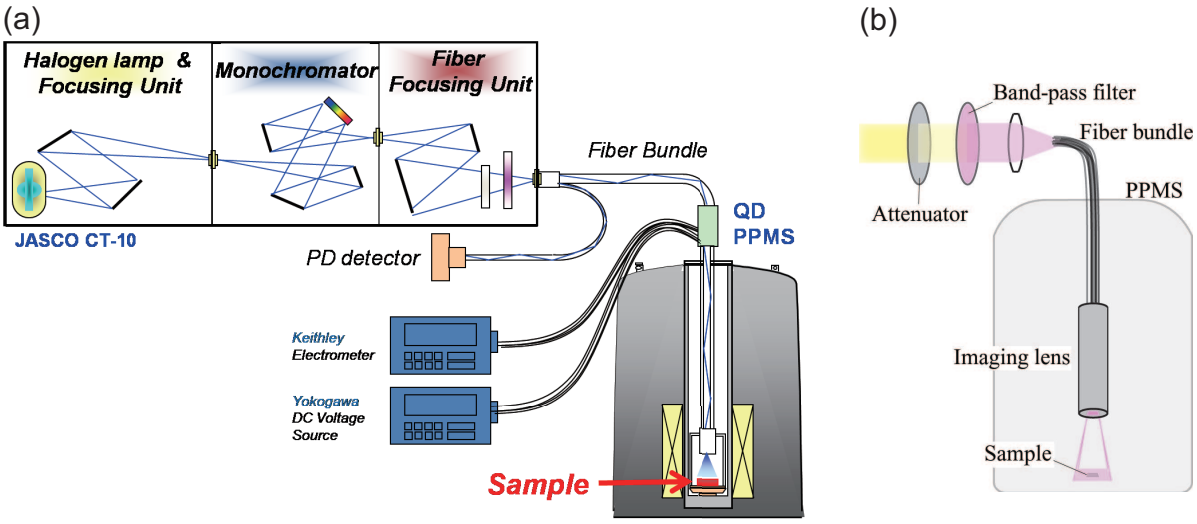

Figure 3.6: Photocurrent measurement setup. (a) Halogen lamp with monochromater guided via optical fiber into the PPMS (courtesy of Y. Hikita). The co-axial cables from the sample stage are connected to the measurement equipments via BNC connectors at the top of the probe. (b) Xe lamp with band-pass filters inside the PPMS (courtesy of Y. Kozuka). Electrical signals are accessed via the internal PPMS connections.

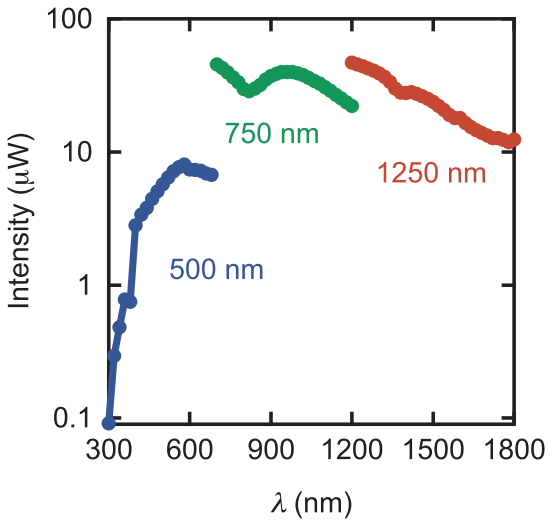

Figure 3.7: Intensity profile of the halogen lamp. The output intensity of a single fiber measured by a Ge and Si photo diode detector is plotted as a function of wavelength the λ. The points in different color correspond to gratings with different Blaze wavelength (500 nm, 750 nm, 1250 nm, respectively).

References

[1] D. B. Chrisey and G. K. Hubler, *Pulsed Laser Deposition of Thin Films*, (Wiley-Interscience, New York, 1994).

[2] W. Braun, *Applied RHEED : Reflection High-energy Electron Diffraction During Crystal Growth*, (Springer, Berlin, 1999).

[3] D. S. Betts, *An Introduction to MilliKelvin Technology*, (Cambridge Univ. Press, Cambridge, 1989).

[4] G. K. White and P. J. Meeson, *Experimental Techniques in Low-Temperature Physics*, 4th ed., (Oxford Univ. Press, Oxford, 2002).

[5] H. London, *Proceedings of the lnternational Conference on Low Temperature Physics*, (Oxford Univ. Press, Oxford, 1951).

[6] H. London, G. R. Clarke, and E. Mendoza, Osmotic Pressure of He^3 in Liquid He^4, With Proposals for a Refrigerator to Work below 1 °K, *Phys. Rev.* **128**, 1992 (1962).

[7] G. Frossati, Experimental Techniques: Methods for Cooling Below 300 mK, *J. Low Temp. Phys.* **87**, 595 (1992).

[8] K. A. Parendo, K. H. Sarwa, B. Tan, and A. M. Goldman, Electrostatic and Parallel-Magnetic-Field Tuned Two-Dimensional Superconductor-Insulator Transitions, *Phys. Rev. B*, **73**, 174527 (2006).

[9] Keithley Instruments, Inc., *Low Level Measurements Handbook*, 6th ed., (Keithley, 2004).

Chapter 4

Photoconductivity Effect of Various $LaAlO_3/SrTiO_3$ Interfaces

Two different insulating oxide interfaces, the $LaAlO_3/SrTiO_3$ P-type and (110) interfaces, are investigated via photoconductivity from the infrared to ultraviolet region at low temperatures. The broadened interface states at $\sim$ 2.3 eV in the P-type interface, and high-density interface states at $\sim$ 2.3 eV with shallow states in the (110) interface are found from the photocurrent spectroscopy measurement at 10 K. The relaxations can be well fitted by a stretched exponential form, manifesting the various trapping centers of the interfaces. Possible long lifetimes of photo-carriers over an hour in the P-type interface will be discussed with photo-Hall measurement at 2 K.

4.1 Introduction

It is well known that at the interface between two materials or the surface of a single material, the energy landscape formed is different from the bulk due to the discontinuity of the atomic array [1]. Depending on the details of the microscopic atomic structures of the interface, it is expected that these interface states should have different characteristic distribution and energy levels. The interface states also play an important role in the Si/SiO_2 field-effect transistor in which operation is considerably degraded by the interface states [2]. Thus, interface engineering is an imperative technique in the research of solid-state materials.

Recently, novel effects of the interface was discovered between the insulators $SrTiO_3$ and $LaAlO_3$ [3]. The $LaAlO_3/SrTiO_3$ interface has three kinds of interfaces, N-type, P-type, and (110) interface, depending on the crystal orientation and the interface termination layer. The N-type interface formed with a TiO_2 terminated (100) $SrTiO_3$ substrate surface shows metallic conductivity, but the insertion of one unit cell of SrO forms an insulating P-type interface. Similarly, the (110) interface is grown on the polar surface

of $SrTiO_3$ but with no polar discontinuity [4]. Most of the recent experimental effort has been focused on the conducting N-type interface [5], and the insulating P-type and (110) interfaces have attracted less interest in the recent literature. These interfaces, while not possessing metallic conductivity, may give a key aspect of the interface engineering concept in the $LaAlO_3/SrTiO_3$ interface.

In this chapter, in order to investigate the electronic states present at these insulating interfaces, the dynamics of photo-carriers are measured at low temperatures. Through the generation and relaxation of the photo-carriers, information of the interface states can be obtained. Additionally, possible band bending is also an important phenomena at the interface, separating electron and hole pairs. These long lived carriers are connected to persistent photoconductivity (see Appendix A). Thus, the concept of interface engineering is also applicable in the fabrication of controllable interfacial conductivity by changing the details of atomic termination at a heterointerface.

4.1.1 $LaAlO_3/SrTiO_3$ P-type and (110) interface

The $LaAlO_3/SrTiO_3$ interface has two kinds of interface in the [100] crystal direction, the N-type (LaO/TiO_2) and the P-type (AlO_2/SrO) interface (see Sec. 1.3.1). The P-type interface is made by inserting a monolayer of a SrO before the growth of the $LaAlO_3$ layers on the TiO_2-terminated (100) $SrTiO_3$ substrate. In the polar continuity picture, holes should be doped in the interface in this case, in order to resolve the polar catastrophe. The interface is found to be insulating, however. At the atomic scale, the difference between the N-type and P-type interfaces was investigated by N. Nakagawa *et al.* [6]. It was found that the P-type interface is more abrupt than the N-type interface, and oxygen vacancies exists at the P-type interface. From the result, it has been concluded that the polar catastrophe was resolved by the oxygen vacancies because the energy cost for hole-doping is larger than the energy for introducing oxygen vacancies.

In the (110) orientation, $SrTiO_3$ is composed of $(SrTiO)^{+4}$ and $(O_2)^{-4}$ stacks, as shown in Fig. 4.2 (a). One difficulty in obtaining an atomically flat surface of the (110) $SrTiO_3$ is that the chemical treatment to obtain the atomically flat surface in the (100) $SrTiO_3$ is applicable to the (110) direction due to its polar nature. It was reported in 2005 that an atomically flat (110) surface of $SrTiO_3$ can be achieved using a two step annealing procedure [4]. In the first step, the (110) $SrTiO_3$ substrate is annealed at high temperature and in a low oxygen pressure to obtain the step and terrace structure. In the second step, the substrate is annealed at relatively low temperature and in a high oxygen pressure to fill oxygen vacancies. While heteroepitaxy of $LaAlO_3$ on the (110) surface was also reported in the paper, the detail of transport measurements was not

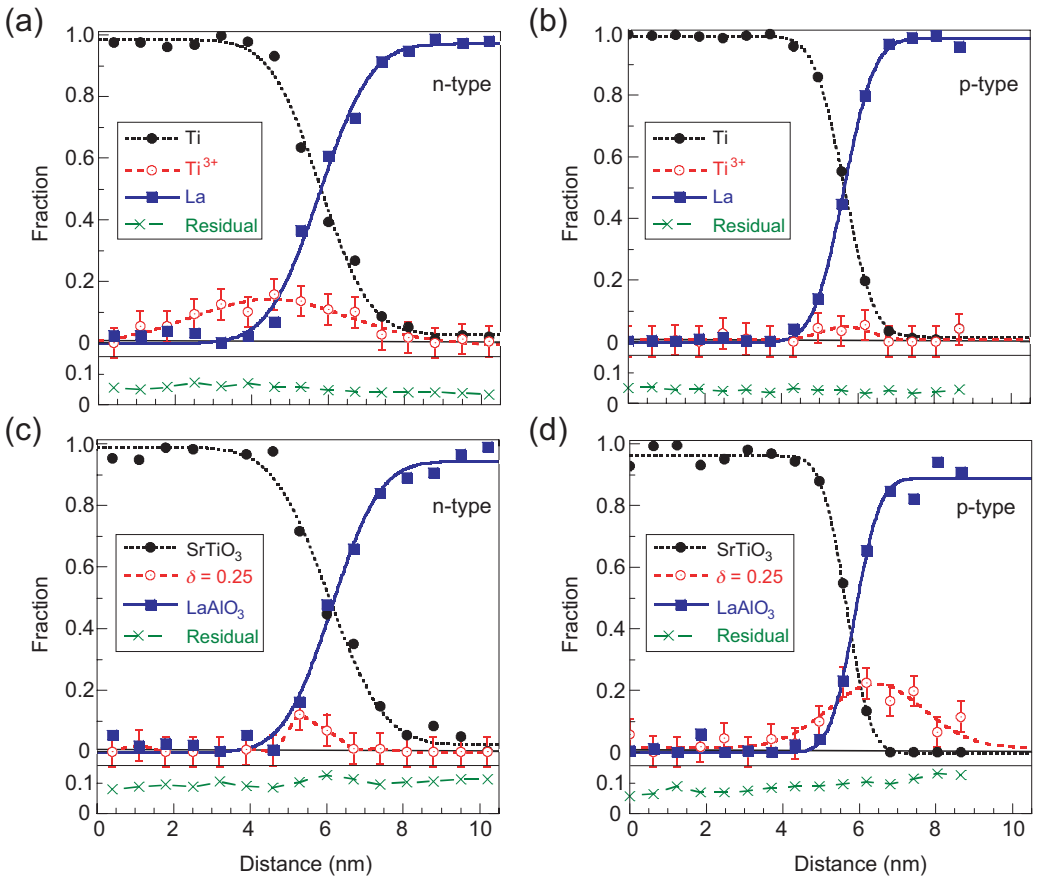

Figure 4.1: Electron energy loss spectroscopy (EELS) profiles of the $LaAlO_3/SrTiO_3$ N-type and P-type interfaces, taken from N. Nakagawa *et al.* [6]. The La, Ti, and Ti^{+3} fraction calculated from the La-M and Ti-L edges in the $LaAlO_3/SrTiO_3$ (a) N-type interface and (b) P-type interface. The fraction of $SrTiO_3$, oxygen vacancy ($SrTiO_{3-\delta}$, δ = 0.25 assumed), and $LaAlO_3$ calculated from the O-K edge in the $LaAlO_3/SrTiO_3$ (c) N-type interface and (d) P-type interface.

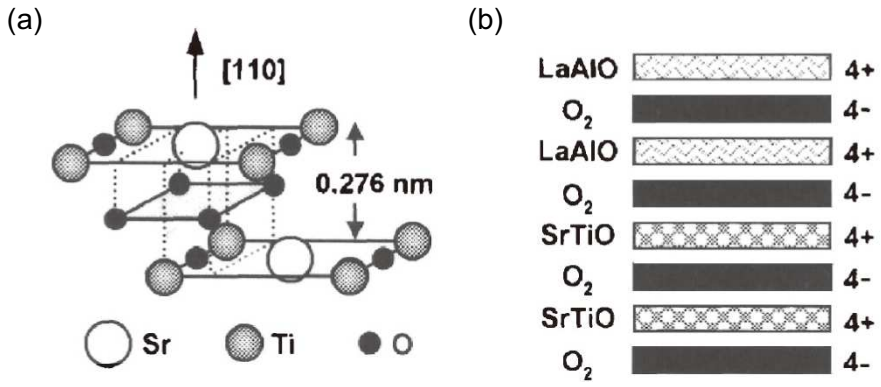

Figure 4.2: Schematic diagram of the $SrTiO_3$ (110) surface and the $LaAlO_3/SrTiO_3$ (110) interface, taken from Y. Mukunoki *et al.* [4]. (a) Atomic structure of the $SrTiO_3$ (110) surface. (b) The $LaAlO_3/SrTiO_3$ (110) interface.

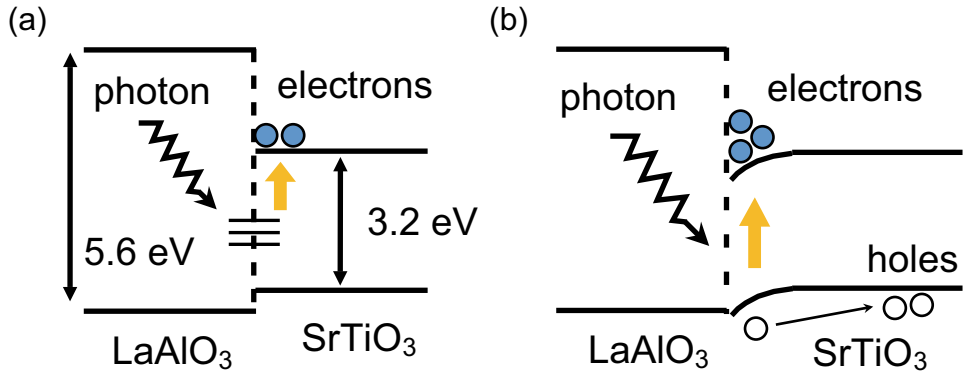

Figure 4.3: Expected photoconductivity effects at the $LaAlO_3/SrTiO_3$ interface. (a) Photo-activation of interface states. (b) Separation of electrons and holes by the band-bending.

investigated. The one characteristic of the the $LaAlO_3/SrTiO_3$ (110) interface is that a polar discontinuity does not occur unlike the (100) orientation, because $SrTiO_3$ and $LaAlO_3$ have the same stacking of charge in the $[1\bar{1}0]$ direction as shown in Fig. 4.2 (b).

4.1.2 Photoconductivity at interfaces

Photoconductivity is defined as the conductivity of carriers created by external photons. It is a fine tool in tuning the conductivity (or carrier density) of the system intrinsically or extrinsically [7]. Intrinsic photoconductivity is obtained from the generation of electron-hole pairs when the irradiating light has an energy larger than the band gap of the material. In contrast, extrinsic photoconductivity can be obtained when the photon energy of the incident light is sufficient to ionize the impurities. Thus impurity ionization energies can be measured with photoconductivity.

For the case of the $LaAlO_3/SrTiO_3$ interface, two scenarios of obtaining photoconductivity are expected, as shown in Fig. 4.3. Here we assumed that the properties of the $SrTiO_3$ in these heterointerfaces dominate any conductivity due to its smaller band gap relative to $LaAlO_3$. First, the photo-activation of interface states gives excess electrons in the conduction band, as shown in Fig. 4.3 (a). As the photon energy of the incident light changes, the information of the energy levels and their distribution can be obtained. This photocurrent spectroscopy measurement will be discussed in Sec. 4.3.1, and is widely used for analyzing defect levels, for example, recently in GaN heterostructures [8, 9] and CdSe alloys [10]. Secondly, photoconductivity can be obtained using photons having an energy in excess of the bandgap of the material, as shown in Fig. 4.3 (b). The photoconductivity study of bulk $SrTiO_3$ using ultra-violet light shows large photoconductivity where the conduction is dominated by electrons while holes are trapped [11]. Additionally, the

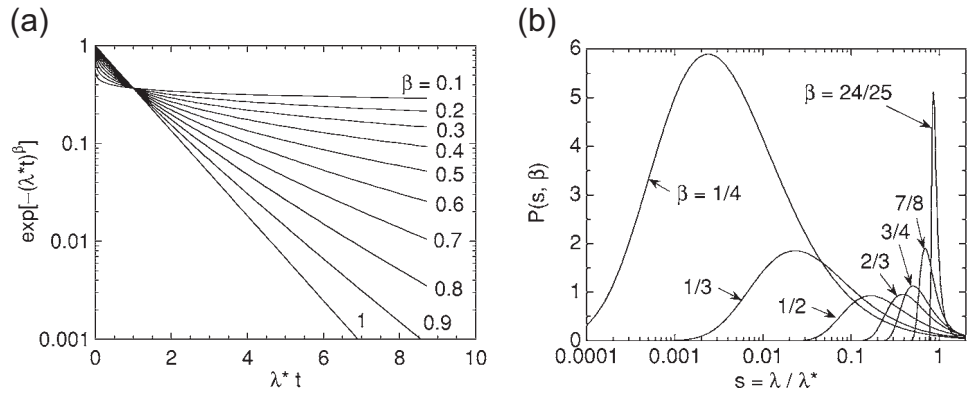

Figure 4.4: Stretched exponential model for a relaxation system, taken from D. C. Johnston [12]. (a) Log-linear plot of the stretched exponential function in Eq. 4.1 versus λt for various β values. The relaxation rate λ is the reciprocal of τ. (b) Semi-log plot of the probability density, which weight the integration of relaxation time versus normalized relaxation rate s for several rational values of β.

possible band-bending at the interface may cause the confinement of electrons near the interface and their separation from holes. This leads to a long life time of photocarriers at low temperatures [13], giving the possibility of persistent photoconductivity (see Appendix A), and non-exponential relaxation of the photocarriers. This will be discussed in the next section, and examined experimentally in Sec. 4.4.

4.1.3 Non-exponential Relaxation Phenomena

The relaxation of excited systems towards the equilibrium state often follows a time evolution which is not exponential. In those relaxations, the rate of change is initially rapid, but becomes continually slower as time progresses. This phenomena is known to appear in various disordered and quenched electronic and molecular systems [14] as well as at heterointerfaces [15, 16]. The relaxations can be described phenomenologically by the stretched exponential form,

$$A(t) = A(0)\exp\left(-\left(\frac{t}{\tau}\right)^{\beta}\right), \tag{4.1}$$

where A is the observed physical parameter, τ is the characteristic relaxation time, and β is the stretching critical component in the range of $0 < \beta < 1$. Fig. 4.4 (a) shows the stretched exponential function. When β is equal to unity, the relaxation will be a pure exponential decay, plotted as a straight line in the figure.

One interpretation of an observed stretched exponential relaxation is in terms of the global relaxation of a system containing many independently relaxing species, each of which decays exponentially in time with a specific fixed relaxation rate $\lambda = 1/\tau$ [12].

Then one can write the stretched exponential function as a sum of pure exponential decays, with a particular probability distribution p of λ values for a given value of β as shown in Fig. 4.4 (b). In such a probability distribution, the characteristic relaxation rate λ^* from a normalization of λ can be given as

$$e^{-(\lambda^* t)^\beta} = \int_0^\infty P(s,\beta) e^{-s\lambda^* t} ds, \tag{4.2}$$

Where $s = \lambda/\lambda^*$ is the normalized relaxation rate, $P(s,\beta)$ is the probability density. From this background, we will discuss the relaxation phenomena of photo-carriers at the $LaAlO_3/SrTiO_3$ interfaces in Sec. 4.3.2.

4.2 Sample Growth and Measurement

The samples were grown by the PLD method (see Sec. 3.1). Three $LaAlO_3/SrTiO_3$ interfaces were investigated: two P-type interfaces having a different $LaAlO_3$ thickness, and a (110) interface. An annealed (100) $SrTiO_3$ substrate for reference was also prepared. The growth conditions are summarized in Tab. 4.1. The $SrTiO_3$ (100) substrates with chemically prepared TiO_2 surfaces [17] are pre-annealed at 950 °C as measured by an external optical pyrometer, for 30 minutes in an oxygen environment of 5×10^{-6} Torr. Following this anneal, one substrate was cooled to room temperature and used as a reference. For the P-type interfaces, the substrate temperature was reduced to the growth temperature T_g, and the oxygen deposition pressure was set. The one unit cell of SrO was grown, followed by $LaAlO_3$ with a thickness of 32 unit cells for P-type (CB) and 16 unit cells for P-type (ST) sample, as monitored using *in-situ* RHEED (see Sec. 3.1.1). The repetition rate of the KrF laser was 2 Hz. For the (110) interface, due to the lack of chemical treatments to define an atomically sharp (110) surface on $SrTiO_3$, we used a previously reported method to achieve a well defined interface using high temperature anneal (1000 °C for one hour) at a relatively low oxygen pressure (5×10^{-7} Torr), followed by a lower temperature re-oxidation (one hour, 500 °C, 1×10^{-4} Torr). After these steps, 32 unit cells of $LaAlO_3$ layers were grown in the conditions shown in Tab. 4.1.

In measurements of photocurrent dynamics (Sec. 4.3) including spectroscopy and relaxation phenomena, the photoconductivity of samples was measured using the Halogen lamp and the Xenon lamp set-ups explained in Sec. 3.3. The samples were ultrasonically wirebonded with Al wire and the resistances of all samples were found to be above 10^{12} Ω at 10 K without irradiation. The photocurrent I_{photo} was measured by the two-probe method with the electrometer at an interval of 250 ms, under the bias voltage of d.c. 5 V. During the measurements, the temperature of the samples was kept at 10 K. I_{photo} is measured in the range 0.7 eV $< E_{\text{photon}} <$ 4.1 eV from the low to high photon

Table 4.1: Growth conditions of the samples used in Chap. 4.

Sample Name	Pre-anneal			Growth		
	T_{sub} (°C)	P_{O_2} (Torr)	t (min)	T_g (°C)	P_{O_2} (Torr)	Fluence (J/cm^2)
Subs.	950	5×10^{-6}	30	-	-	-
P-type (CB)	950	5×10^{-6}	30	800	1×10^{-5}	1.6
P-type (ST)	950	5×10^{-6}	30	600	1×10^{-5}	1.4
(110) interface	1000	5×10^{-7}	60	600	2×10^{-3}	1.6
	500	1×10^{-4}	60			

energy region. After the irradiation of the light for 100 secs, the shutter is closed and the relaxation is measured without irradiation for another 100 secs. Normalized photocurrent (NPC) is defined in this study as the value of I_{photo} 60 secs after the shutter opened, normalized by the intensity at the photo diode detector shown in Fig. 3.7.

The photo-Hall measurement (Sec. 4.4) was made using the Xenon lamp with the PPMS resistance bridge at 2 K using the four-probe method. At first, the sample was cooled to 2 K and the light of wavelength 380 nm was irradiated for one hour. Then the Photo-Hall measurement is made during the irradiation of the light. After the Hall measurement, the light was turned off and the sample was left for one hour followed by the magnetoresistance measurement.

4.3 Photocurrent Dynamics

Photocurrent dynamics are measured in three samples, the P-type (CB), (110) interface, and annealed $SrTiO_3$ substrate. The typical result of I_{photo} dynamics is shown in Fig. 4.5. Two interfaces showed slow dynamics, where an increase and a decrease of I_{photo} are not saturated within the scale of 100 secs. In contrast, the substrate shows much faster dynamics than the two interfaces. The (110) interface shows I_{photo}, about four orders of magnitude larger than that of the P-type interface and the substrate. A negative transient photocurrent is found in the P-type interface: a fast initial decrease or increase of the photocurrent as soon as the light is turned on or off, only in the range of $E_{photon} <$ 1.8 eV. This phenomenon has been also reported in other systems [18], but will not be discussed further in this study.

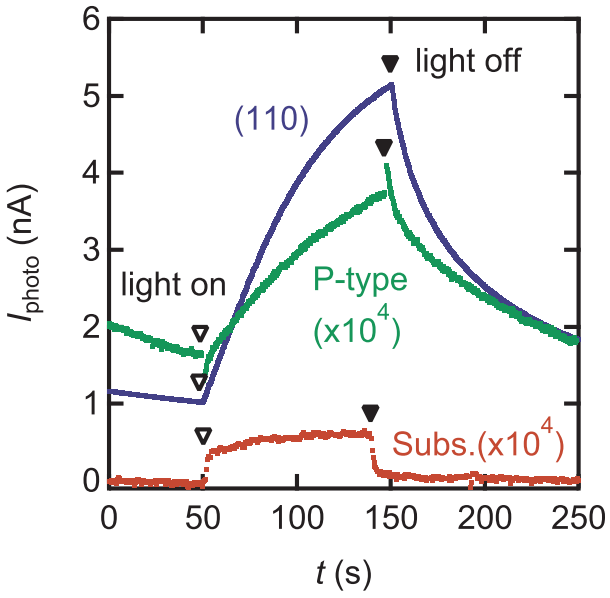

Figure 4.5: Typical photocurrent dynamics of the $LaAlO_3/SrTiO_3$ interfaces. The photon energy used was 1.8 eV, and the temperature was 10 K. Blue, green, and red points are the (110) interface, the P-type interface, and annealed (100) $SrTiO_3$ substrate, respectively. Open triangles show when irradiation of the samples started, and closed triangles indicate when the irradiation stopped.

4.3.1 Photocurrent Spectroscopy

The photocurrent spectra of the samples are shown in Fig. 4.6. An abrupt increase above 3.2 eV due to the fundamental absorption of $SrTiO_3$ is found for three samples. The annealed substrate shows almost no variation with E_{photon} below the bandgap energy of $SrTiO_3$. The P-type interface shows an increase from $\sim$ 2.0 eV with saturation around 2.7 eV. In the low energy region ($E_{\text{photon}} < 2$ eV), the photocurrent was too small for the assignment of clear features in the spectrum. The (110) interface showed an increase of normalized I_{photo} almost exponentially increasing with E_{photon} up to $\sim$ 2.5 eV before again saturating around 2.7 eV, similar to the P-type interface. From these results, it can be concluded that compared to the substrate, the two interfaces have interface states within the band gap. At the P-type interface, the interface states are located at 2.3 eV below the conduction band minimum as shown in Fig. 4.7 (a). However, their energy levels are non-discrete and broadened from 2.0 eV to 2.7 eV. The (110) interface shows a more broad increase of NPC as E_{photon} increases. Thus, the (110) interface is expected to have broad interface states as well as many shallow states within the band gap, as shown in Fig. 4.7 (b).

It is known that many levels of interface traps closely spaced in energy cannot be distinguished as separate levels and actually appear as a continuum over the band-gap of

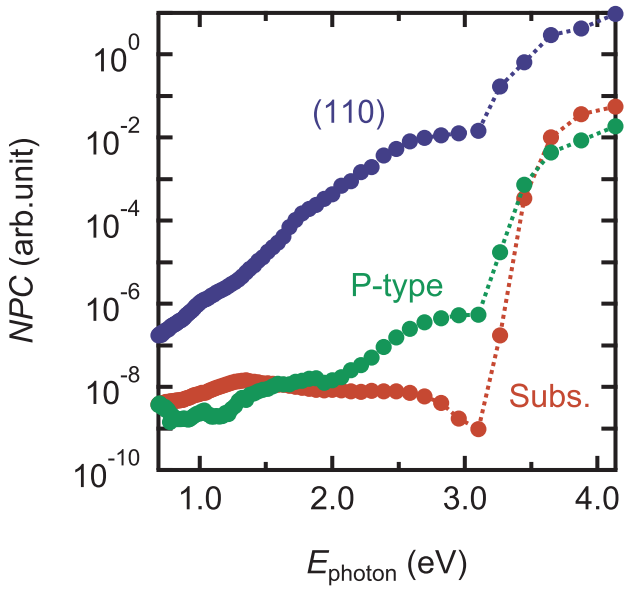

Figure 4.6: Photocurrent spectroscopy of the P-type and (110) interface and annealed $SrTiO_3$ substrate. Normalized photocurrent (NPC) refers to the photocurrent normalized by the relative intensity. NPC is plotted as a function of E_{photon}. The temperature is 10 K.

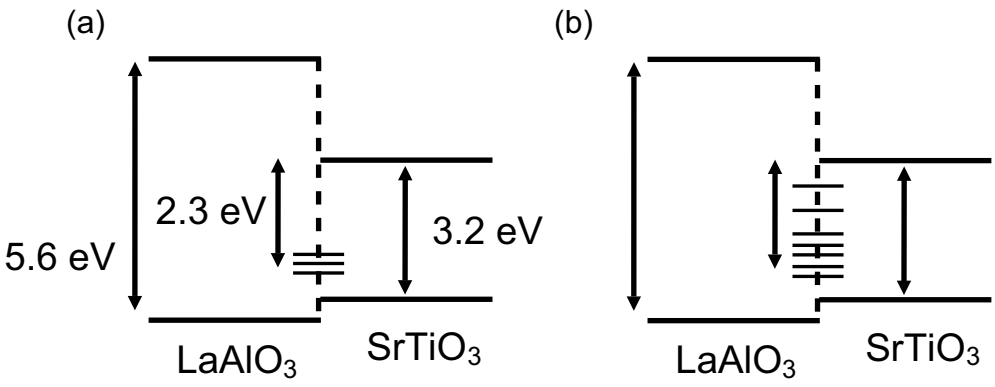

Figure 4.7: Schematic band diagrams of the (a) P-type and (b) (110) interfaces, based on the result of transient photocurrent spectroscopy.

the semiconductor, as revealed at the Si-SiO_2 interface [2]. In the case of interfaces with $SrTiO_3$, it was reported that trap states exist around 2.3 eV in amorphous $CaHO_3/SrTiO_3$ interface probed by photoconductivity measurement, with were attributed to oxygen vacancies [19]. This can be one possible explanation of the experimental results, considering the P-type interface has oxygen vacancies at the interface compensating the polar discontinuity [6]. The origin of the high density of interface states in the (110) interface is not clear at present. There is a possibility that some carriers had existed before the irradiation, which we know from the fact that the conductivity level of the (110) interface in dark was a few orders higher than that of the P-type interface, caused nontrivial effects in the photocurrent experiment. Further study on the (110) interface will be needed to understand the origin for these observations.

4.3.2 Non-Exponential Relaxation of Photocarriers

Next, we discuss the relaxation of I_{photo}. The results of the photocurrent relaxation of the P-type and (110) interface are shown in Fig. 4.8. The annealed substrate shows much faster decay, whose relaxation time is below the measurement resolution. While the relaxation in the (110) interface becomes faster as E_{photon} decreases in the entire energy range as shown in Fig. 4.8 (b), in the P-type interface an anomalous change of the relaxation is observed as shown in Fig. 4.8 (a). The normalized I_{photo} decays faster as E_{photon} decreases for the energy region, 3.3 eV $< E_{\mathrm{photon}} <$ 4.1 eV. However, in the range of 2.1 eV $< E_{\mathrm{photon}} <$ 3.3 eV, the decay becomes slower as E_{photon} decreases. Below 2.1 eV, it becomes faster again.

We found that the relaxations at both interfaces are well fitted by Eq. 4.1, showing the typical fitting results at $E_{\mathrm{photon}} = 1.8$ eV in Fig. 4.9 (a). From the fitting, the characteristic relaxation time τ and the critical component β are obtained, as shown in Figs. 4.9 (b) and (c), respectively.

For 1.8 eV $< E_{\mathrm{photon}} <$ 3.1 eV, the change of β at both interfaces is rather small, but the decrease of τ for increasing E_{photon} is notable at both interfaces, particularly the P-type interface. This result indicates that the interface states of $\sim$ 2.3 eV, revealed in the last section, affects the relaxation phenomena. When E_{photon} is lower than the energy of interface states $\sim$ 2.3 eV, the photo-carriers are captured by the shallow trapping states, causing the longer lifetime [20]. However, when the interface states are activated, the major relaxation traffic passes through the interface states and the trapping of photo-carriers is accelerated. This can explain the result of the P-type interface, revealed to have relatively few shallow states and many interface states from the spectroscopy, causing the remarkable change of τ. The fact that the (110) interface has a high density of shallow

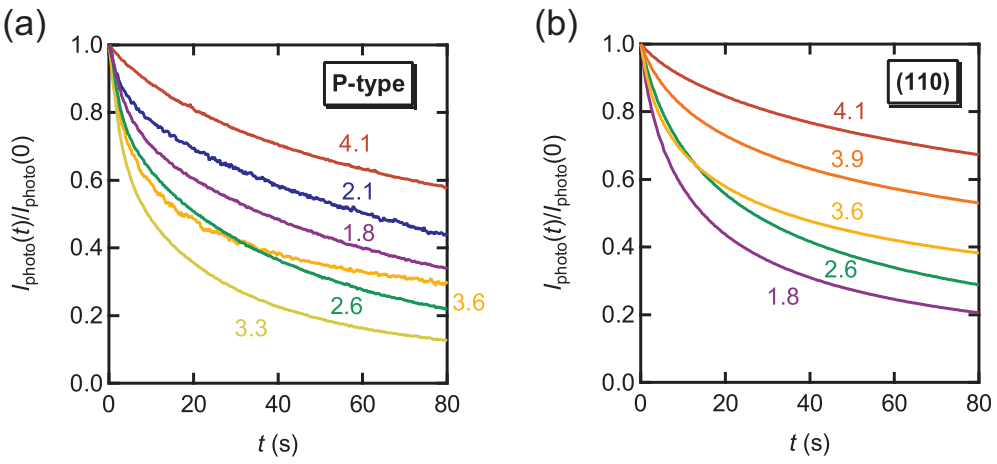

Figure 4.8: The relaxation of the normalized photocurrent of the $LaAlO_3/SrTiO_3$ interfaces at 10 K. (a) the P-type interface and (b) the (110) interface. Photocurrents $I_{\text{photo}}(t)$ are normalized by the initial value $I_{\text{photo}}(0)$ of the relaxation. Numbers in the figures correspond to E_{photon} in eV unit.

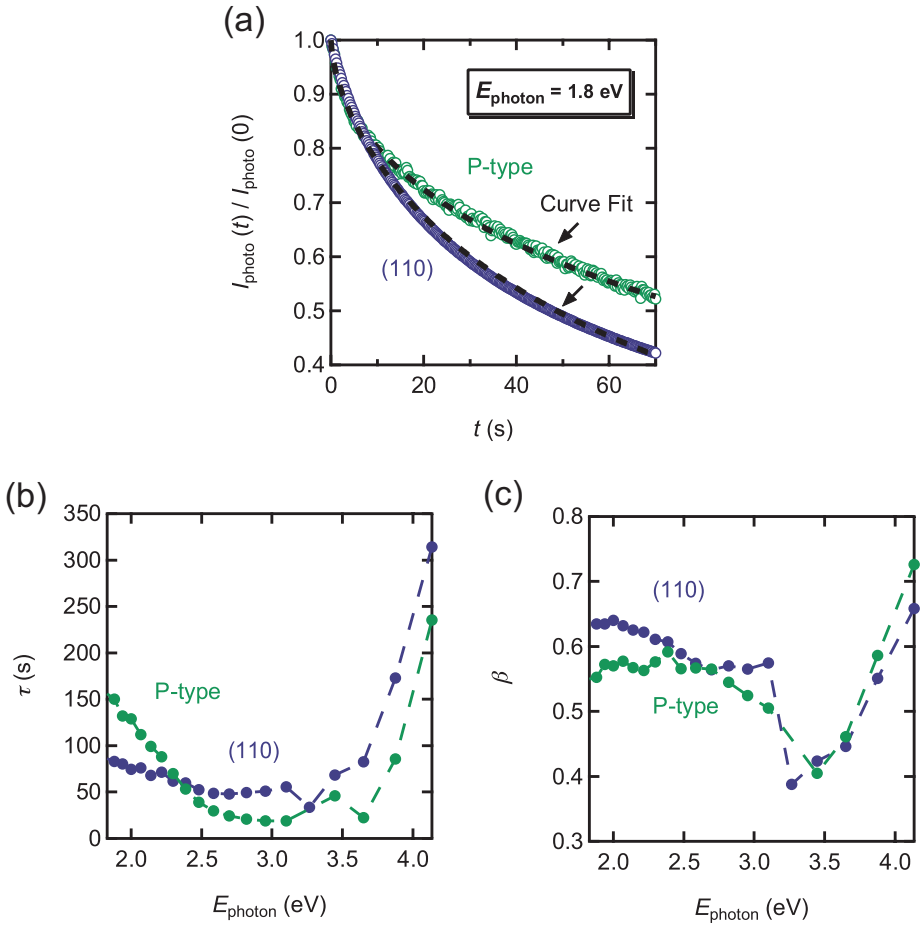

Figure 4.9: The stretched exponential fit of the P-type (green) and (110) interface (blue). (a) The relaxation of normalized photocurrent at $E_{\text{photon}} = 1.8$ eV at 10 K. The black dotted line is a fitting curve using Eq. 4.1. The parameter obtained from the fit, (b) τ and (c) β of the P-type and (110) interface.

states can also be explained by the relatively small change of τ.

Above $E_{\mathrm{photon}} > 3.3$ eV, both interfaces show similar variation of β and τ with E_{photon}. As the band gap is approached, after an initial decrease, β increases in tandem with τ. The intrinsic photoconductivity effect with generation of electron-hole pair in $SrTiO_3$ becomes dominant and the relaxation phenomena is changed drastically from the below bandgap region, showing longer τ, over a few hundreds sec and a larger β close to unity as E_{photon} increases. It should be noted that in this region, increasing $I_{\mathrm{photo}}(0)$ nontrivially affects the relaxation dynamics of the photo-carriers [10] because the background photo-carriers are so large and cannot be neglected by the 100 secs of the relaxation process. However, the large τ value at the ultraviolet region indicates the slow relaxation process of the photo-carriers. This will be further investigated by the photo-magnetotransport measurement in the next section.

4.4 Photo-Hall measurement of P-type interface

The photo-Hall measurement is performed using the P-type interface (ST) with the irradiation of the ultraviolet light ($E_{\mathrm{photon}} = 3.3$ eV). The (110) interface became insulating too fast after the light had turned off to allow a magnetoresistance measurement to be made. Thus, only the P-type interface will be discussed here. The measurement results are summarized in Fig. 4.10 and Tab. 4.2. As is clear from Fig. 4.10 (a), ρ_{xx} after the irradiation is ~ 17 times larger than during the irradiation. Positive magnetoresistance is found in both cases, however the shape of magnetoresistance in the low field regime shows a distinct change in curvature during irradiation, whereas no such feature is found after irradiation. From the Hall measurement, as shown in Fig. 4.10 (b), a clear nonlinearity of ρ_{xy} is found during irradiation, as found in photocarrier-doped bulk $SrTiO_3$ [11]. After the irradiation, however, the nonlinearity disappeared. The sheet carrier density N_{s}, which was calculated from the low-field region (< 0.1 T), is almost constant ($\sim 1.8\times10^{13}$ cm^{-2}) during and after the irradiation. However, the mobility decreased from 4530 to 273 cm^2/Vs.

There are two questions to be addressed from the result: first, why did the mobility decrease after the irradiation? Second, how can the photo-carriers survive more than an hour? The macroscopic change of the interfacial properties can be one of the origins for the reduction in the mobility, such as the increase of the permittivity by ultra-violet light reported in bulk $SrTiO_3$ [21]. If this is the case, the permittivity of $SrTiO_3$ is reduced after the irradiation, causing less screening of the impurities and hence the decreasing the electron mobility. In fact, the mobility modulation in photo-induced measurements is reported in other oxide heterostructures [22], not consisting of high permittivity such

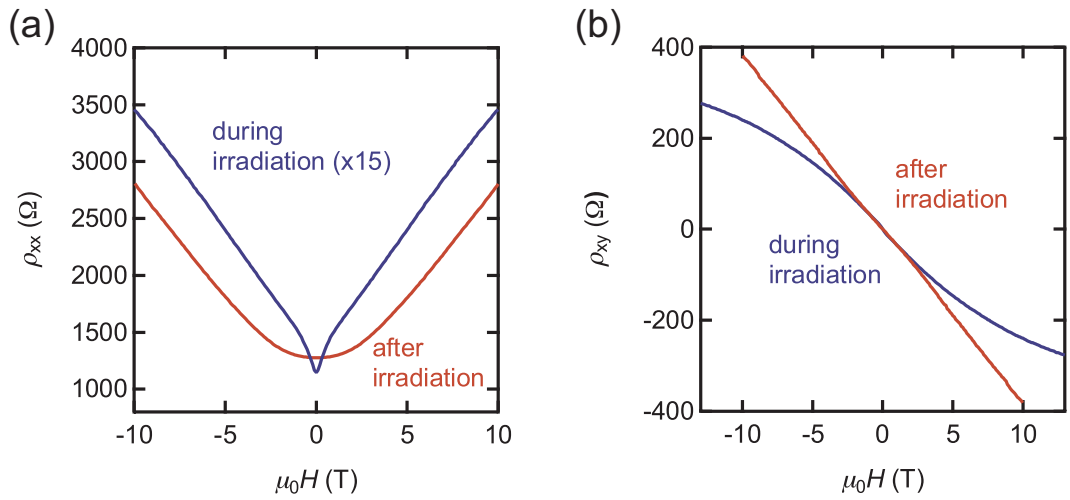

Figure 4.10: The magnetoresistance of the P-type interface during (blue line) and after (red line) the irradiation at 2 K. E_{photon} of the light irradiated to the sample was 3.3 eV. (a) Longitudinal sheet resistivity. (b) Hall resistivity.

Table 4.2: The characteristic electronic parameters during and after the irradiation in the P-type interface.

-	ρ_{xx} ($\Omega/\square$) at 0 T	N_{s} (cm^{-2})	μ ($\mathrm{cm}^2/\mathrm{Vs}$)
During the irradiation	76.4	1.83×10^{13}	4530
After the irradiation	1275.2	1.80×10^{13}	273

as $SrTiO_3$. We can also consider the decreased mobility from a microscopic perspective: after the irradiation, for example, the low-mobility regions are partially created in the sample and the mobility of the sample decreases [23]. This inhomogeneity of the sample is indicated from the fact that the $LaAlO_3/SrTiO_3$ P-type interface has many compensated oxygen vacancies, as discussed in Sec. 4.1.1.

The more remarkable issue would be that the unchanged carrier density, meaning the enhancement of the lifetime of the photo-carriers longer than one hour. A naive interpretation of the result would be the band-bending picture at the interface, which was discussed in Sec. 4.3. The electrons are confined to the interface, while the holes moved to the substrate causing the physical separation of the electron-hole pair and preventing the recombination. The fact that this would be the N-type like band-bending, i.e. conduction and valence band are bent downward at the interface, is not consistent with the polar discontinuity. There is another possibility that oxygen vacancies were created from the ultra-violet irradiation. If the oxygen vacancy is created permanently, however, the change of mobility cannot be easily explained in this scenario and no significant

difference during and after irradiation would be expected. Although we cannot fully understand the exact reason of the long lifetime, it is obvious from the result that longer lifetime of the photo-carriers, suggests the possibility of persistent photoconductivity at lower temperature of $\sim$ 20 mK.

4.5 Summary

In this chapter, the physical properties of the $LaAlO_3/SrTiO_3$ P-type and (110) interfaces were investigated via photoconductivity effects from the infrared to ultraviolet region at low temperatures. We made the photocurrent spectroscopy and relaxation measurement at 10 K, and found that the P-type interface has broad interface states at $\sim$ 2.3 eV below the conduction band minimum of $SrTiO_3$, whereas the (110) interface has a high density of interface states at $\sim$ 2.3 eV with broader shallow states. The photocurrent relaxations of both interfaces could be well fitted by a stretched exponential form, showing the characteristic relaxation to the energetically distributed trap states at each interface. From these results, the different distribution of the interface states in each interface demonstrates the importance of the atomic engineering of the $LaAlO_3/SrTiO_3$ interface. The lifetimes of the photo-carriers over a few hundred seconds were found using ultraviolet light in both interfaces. In the photo-Hall measurement using high-intensity ultraviolet light at 2 K, the long lifetime of the photo-carriers over one hour are found in the P-type interface, indicating the possibility of persistent photoconductivity.

References

[1] W. Shockley, On the Surface States Associated with a Periodic Potential, *Phys. Rev.* **56**, 317 (1939).

[2] S. M. Sze, *Physics of Semiconductor Devices*, 2nd ed., (Wiley-Interscience, New York, 1981).

[3] A. Ohtomo and H. Y. Hwang, A High-Mobility Electron Gas at the $LaAlO_3/SrTiO_3$ Heterointerface, *Nature* **427**, 423 (2004).

[4] Y. Mukunoki, N. Nakagawa, T. Susaki, and H. Y. Hwang, Atomically Flat (110) $SrTiO_3$ and Heteroepitaxy, *Appl. Phys. Lett.* **86**, 171908 (2005).

[5] M. Huijben, A. Brinkman, G. Koster, G. Rijnders, H. Hilgenkamp, and D. H. Blank, Structure-Property Relation of $SrTiO_3/LaAlO_3$ interfaces, *Adv. Mater.* **21**, 1665 (2009).

[6] N. Nakagawa, H. Y. Hwang, and D. A. Muller, Why Some Interfaces Cannot be Sharp, *Nature Mater.* **5**, 204 (2006).

[7] P. Y. Yu and M. Cardona, *Fundamentals of Semiconductors*, 3rd ed., (Springer, Berlin, 2005).

[8] X. Z. Dang, C. D. Wang, E. T. Yu, K. S. Boutros, and J. M. Redwing, Persistent Photoconductivity and Defect Levels in n-type AlGaN/GaN Heterostructures, *Appl. Phys. Lett.* **72**, 2745 (1998).

[9] P. B. Klein, S. C. Binari, J. A. Freitas, Jr., and A. E. Wickenden, Photoionization Spectroscopy of Traps in GaN Metal-Semiconductor-Field-Effect Transistors, *J. Appl. Phys.* **88**, 2843 (2000).

[10] H. X. Jiang and J. Y. Lin, Persistent Photoconductivity and Related Critical Phenomena in $Ze_{0.3}Cd_{0.7}Se$, *Phys. Rev. B* **40**, 10025 (1989).

[11] Y. Kozuka, T. Susaki, and H. Y. Hwang, Vanishing Hall Coefficient in the Extreme Quantum Limit in Photocarrier-Doped $SrTiO_3$, *Phys. Rev. Lett.* **101**, 096601 (2008).

[12] D. C. Johnston, Stretched Exponential Relaxation Arising From a Continuous Sum of Exponential Decays, *Phys. Rev. B* **74**, 184430 (2006).

[13] H. J. Queisser, Nonexponential Relaxation of Conductance near Semiconductor Interfaces, *Phys. Rev. Lett.* **54**, 234 (1985).

[14] J. C. Phillips, Stretched Exponential Relaxation in Molecular and Electronic Glasses, *Rep. Prog. Phys.* **59**, 1133 (1996).

[15] H. J. Queisser and D. E. Theodorou, Decay Kinetics of Persistent Photoconductivity in Semiconductors, *Phys. Rev. B* **33**, 4027 (1986).

[16] J. R. Nesbitt and A. F. Hebard, Time-dependent Glassy Behavior of Interface States in Al-AlO_x-Al Tunnel Junctions, *Phys. Rev. B* **75**, 195441 (2007).

[17] M. Kawasaki, K. Takahashi, T. Maeda, R. Tsuchiya, M. Shinohara, O. Ishiyama, T. Yonezawa, M. Yoshimoto, and H. Koinuma, Atomic Control of the $SrTiO_3$ Crystal Surface, *Science* **266**, 1540 (1994).

[18] C. M. Penchina, J. S. Moore, and N. Holonyak, Jr., Energy Levels and Negative Photoconductivity in Cobalt-Doped Silicon, *Phys. Rev.* **143**, 634 (1966).

[19] T. Uozumi, *Growth and Characterization of Scandate Insulator Films for Oxide Field-Effect Devices*, Master Thesis, The University of Tokyo, 2006.

[20] A. Rose, Recombination Process in Insulators and Semiconductors, *Phys. Rev.* **97**, 322 (1955).

[21] T. Hasegawa, S. Mouri, Y. Yamada, and K. Tanaka, Giant Photo-Induced Dielectricity in $SrTiO_3$, *J. Phys. Soc. Jpn.* **72**, 41 (2003).

[22] A. Tsukazaki, A. Ohtomo, M. Nakano, and M. Kawasaki, Photoinduced Insulator-to-Metal Transition in $ZnO/Mg_{0.15}Zn_{0.85}O$ Heterostructures, *Appl. Phys. Lett.* **92**, 052105 (2008).

[23] R. H. Bube, Interpretation of Hall and Photo-Hall Effect in Inhomogeneous Materials, *Appl. Phys. Lett.* **13**, 136 (1968).

Chapter 5

Superconducting Properties of $SrTiO_3$/Nb:$SrTiO_3$/$SrTiO_3$ Heterostructures

In this chapter, the superconducting properties of $SrTiO_3$/Nb:$SrTiO_3$/$SrTiO_3$ heterostructures are discussed. With the precise control of high-quality $SrTiO_3$ thin films, a few hundreds to a few nanometer of superconducting layers are fabricated. A crossover of superconductivity from three dimensional to two dimensional behavior is found around a critical thickness of $\sim$ 100 nm, consistent with estimates of the Ginzburg-Landau coherence length. Near the thin limit of the narrow doping layer, the electron wavefunction quantum mechanically spreads into the cleaner undoped regions giving rise to an enhancement of the electron mean free path. Several novel properties are found such as the violation of the paramagnetic limit, and an increase of the superconducting transition temperature. We also discuss the BKT transition measured in the two-dimensional and three-dimensional superconducting samples. These results indicate that delta-doping is a feasible technique to study two-dimensional superconductors.

5.1 Introduction

Intense research into the superconductivity in oxide materials has been performed following the discovery of high T_c superconductivity. The fact that these high-T_c materials are layered superconductors [1] with strong anisotropy between the a-b plane and c-axis direction, invokes interest in the fundamental properties of low-dimensional superconducting thin films. $SrTiO_3$, the representative perovskite oxide is well known as the parent material of the cuprate superconductors [2]. $SrTiO_3$ can be made metallic with chemical doping (n-type) and becomes superconducting with the lowest carrier density of all known materials [3]. It has been studied continuously from the 1960's, more than 20 years before the discover of high T_c superconductivity. Much research has focused

on the high permittivity and the superconducting properties. Recently, superconducting n-$SrTiO_3$ thin films have been reported by several groups, but their film quality was degraded from the bulk and it was hard to approach the nanometer scale of electron-doped $SrTiO_3$ thin films. In this chapter, with the recent establishment of high-quality growth techniques, we investigate the superconducting properties of $SrTiO_3$/Nb:$SrTiO_3$/$SrTiO_3$ heterostructures with a Nb concentration of 1 atomic %, and the thinnest doped layer of $\sim$ 3.9 nm. As the doped $SrTiO_3$ layer between the undoped layers decreases, a dimensional crossover of superconductivity is expected when the thickness of the doped layer becomes smaller than the Ginzburg-Landau coherence length. In the thin limit, a two-dimensional superconductor with a small number of atomic layers may be realized, leading to novel delta-doping effects such as spreading of the superconducting electron wavefunction out from the dopant plane. We also find a violation of the in the Pauli paramagnetic limit, and an increase of superconducting transition temperature indicating the possibility of unconventional behavior, for example a topological change of the Fermi surface, in the delta-doped superconductor.

5.1.1 Basic Superconducting Properties

According to the Bardeen-Cooper-Schrieffer (BCS) theory, the superconducting transition temperature T_c is given as

$$T_c = 1.14\frac{\hbar\omega_D}{k_B}\exp\left(-\frac{1}{N(0)V}\right), \tag{5.1}$$

where $\hbar$ is Plank's constant divided by 2π, ω_D is the Debye frequency, k_B is Boltzmann's constant, $N(0)$ is the density of states at the Fermi surface and V is the electron-phonon coupling potential. Eq. 5.1 assumes the weak coupling limit in the superconductor where $N(0)V \ll 1$.

The McMillan formula for the strong coupling case ($N(0)V = \lambda \approx 1$) gives the more complex formula

$$T_c = \frac{\hbar\omega_D}{1.45k_B}\exp\left(-\frac{1.04(1+\lambda)}{\lambda-\mu^*(1+0.62\lambda)}\right), \tag{5.2}$$

where μ^* is the screened and retarded Coulomb repulsion parameter, which is generally found to be in the range $0.1 \sim 0.15$. The quantity λ involves the details of the phonon density $F(\omega)$, and the electronic matrix elements $\alpha^2(\omega)$ and is given by

$$\lambda = 2\int_0^\infty \frac{\alpha^2(\omega)F(\omega)}{\omega}\mathrm{d}\omega = \frac{N(0)\langle I^2\rangle}{M\langle\omega^2\rangle}. \tag{5.3}$$

Here $\langle I^2\rangle$ is a Fermi-surface momentum average over the electronic matrix elements, M is the nuclear mass, $\langle\omega^2\rangle$ is an average over the phonon frequencies, $\alpha^2(\omega)F(\omega)$ is the electron-phonon spectral function which can be obtained from tunnelling measurements.

The BCS theory explains superconductivity in terms of a condensation of many overlapping Cooper pairs with the same superconducting phase. In the simplest case, each Cooper pair consists of two electrons with opposite spin and momentum, with time-reversal symmetry.[1] The Cooper pair has an energy scale of the BCS superconducting gap $\Delta_0 = 1.76 k_{\rm B} T_{\rm c}$. This can be converted to a distance via the wave number, $\delta k \approx k_{\rm F}(\Delta_0/\epsilon_{\rm F}) \approx \Delta_0/\hbar v_{\rm F}$, where $v_{\rm F}$ is the Fermi velocity. The length scale in real space corresponding to δk is thus given by

$$\xi_{\rm BCS} = \frac{\hbar v_{\rm F}}{\pi \Delta_0}, \tag{5.4}$$

where $\xi_{\rm BCS}$ is called the BCS coherence length. A superconductor can be characterized by the ratio between the electron mean free path l and the BCS coherence length $\xi_{\rm BCS}$ of the material. If the mean free path is larger than the BCS coherence length $l \gg \xi_{\rm BCS}$, the sample is in the *clean limit*. If the BCS coherence length is larger than the mean free path $l \ll \xi_{\rm BCS}$, it is in the *dirty limit*.

5.1.2 Superconducting Thin Films

In 1959, P. W. Anderson explained that nonmagnetic impurities have no considerable effect on $T_{\rm c}$ by pointing out that Cooper pairs are formed out of time-reversed eigenstates, whose density of states is not strongly affected by disorder [5]. Subsequently experiments showed a depression of $T_{\rm c}$ in ultra thin films [6], as shown in Fig. 5.1 (a), and anomalous upper critical field [7] behavior with increasing disorder. Thus the two-dimensional superconductor-insulator transition [8, 9] has been widely studied by using amorphous or polycrystalline metal thin films. These thin films are dirty superconductors where $l \ll \xi_{\rm BCS}$, and give a model system to induce a large amount of disorder either on the atomic or mesoscopic scale. As the thickness of a metal film decreases, the electrons suffer more scattering and tend to be localized, breaking the superconductivity. As a result, the transition temperature decreases as shown in Fig. 5.1 (a). Fig. 5.1 (b) shows a drastic reduction of the mean free path for decreasing thickness in Pb films, so most thin metal films are in the dirty limit, including recent studies of ultra thin metal alloys [10].

5.1.3 Tinkham's Model

The theory of the magnetic response of two-dimensional superconductors was proposed by M. Tinkham [13, 14], based on a linearized form of the Ginzburg-Landau theory considering flux quantization. When the thickness of a superconducting film d is less than

[1] Unconventional superconductivity often breaks the time-reversal symmetry of Cooper pairs. This will be discussed briefly in Sec. 5.4.3.

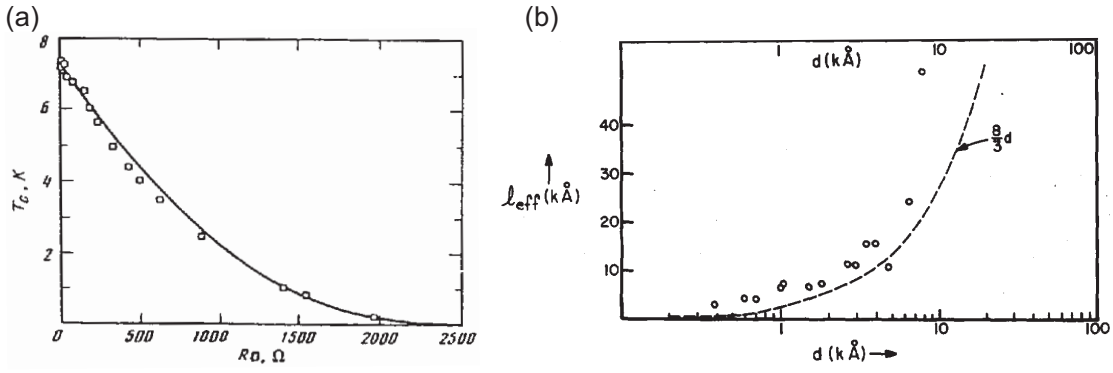

Figure 5.1: Metallic and superconducting properties in metal thin films. (a) Suppression of superconductivity in homogeneous amorphous $Mo_{79}Ge_{21}$ films [6]. The solid line is a theoretical fit to a model based on weakening of the Coulomb screening by disorder [11]. (b) The mean free path of electrons in Pb *vs* thickness [12].

the Ginzburg-Landau coherence length ξ_{GL}, which refers to the size of the normal core of a vortex, the dimensionality is reduced from three dimensions to two dimensions and the fundamental properties, for example the upper critical fields, change drastically.

When the external magnetic field is applied parallel to the superconducting thin films, the width of the supercurrent loop is limited by film thickness (Fig. 5.2 (a)). In perpendicular field geometry, however, size of the loop can adjust depending on field strength so as to minimize energy (Figs. 5.2 (b) and (c)). This causes a different free energy increase, giving the temperature dependence of the upper critical field in each field geometry as

$$H_{\mathrm{c2}}^{\perp}(T) = \frac{\Phi_0}{2\pi\xi_{\mathrm{GL}}(0)}\left(1-\frac{T}{T_{\mathrm{c}}}\right), \tag{5.5}$$

$$H_{\mathrm{c2}}^{\parallel}(T) = \frac{\Phi_0\sqrt{12}}{2\pi\xi_{\mathrm{GL}}(0)d_{\mathrm{Tinkham}}}\left(1-\frac{T}{T_{\mathrm{c}}}\right)^{\frac{1}{2}}, \tag{5.6}$$

where $\Phi_0 = h/2e = 2.07\times10^{-15}$ Wb is flux quantum, $\xi_{\mathrm{GL}}(0)$ is Ginzburg-Landau coherence length extrapolated to $T = 0$ K, and d_{Tinkham} is the thickness of superconducting layer. Note that $H_{\mathrm{c2}}^{\perp}$ shows a linear temperature dependence, while $H_{\mathrm{c2}}^{\parallel}$ shows a square root dependence. This will be used in Sec. 5.3.1 as a main diagnostic of the dimensionality of the superconducting films.

From the same assertions, the angular dependence of the upper critical field can be shown to be

$$\left|\frac{H_{\mathrm{c2}}(\theta)\sin\theta}{H_{\mathrm{c2}}^{\perp}}\right| + \left(\frac{H_{\mathrm{c2}}(\theta)\cos\theta}{H_{\mathrm{c2}}^{\parallel}}\right)^2 = 1, \tag{5.7}$$

where θ is the angle between the magnetic field and the sample plane. Also we can

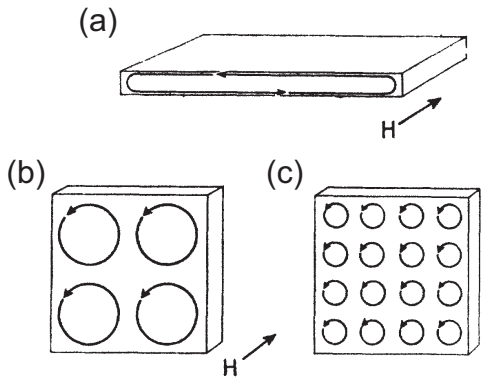

Figure 5.2: Schematic diagram of the current configurations in the parallel and perpendicular field cases, taken from M. Tinkham [13]. (a) Parallel field geometry. Configuration (c) corresponds to higher field strength than (b). Each loop contains one flux quantum.

calculate the superconducting layer thickness be combining Eqs. 5.5 and 5.6 to give

$$d_{\mathrm{Tinkham}} = \sqrt{\frac{6\Phi_0 H_{c2}^{\perp}}{\pi (H_{c2}^{\parallel})^2}}. \tag{5.8}$$

Thus d_{Tinkham} can be found by measurement of the perpendicular and parallel upper critical fields of a sample experimentally. This will be discussed in Sec. 5.3.2.

5.2 Sample Growth and Measurement

$SrTiO_3$/Nb:$SrTiO_3$/$SrTiO_3$ heterostructures were deposited by PLD as introduced in Sec. 3.1, in a low oxygen partial pressure of less than 10^{-7} Torr, followed by post-annealing in a moderate oxidizing condition to fill oxygen vacancies. The high-temperature growth above $\sim$ 1050 °C was chosen, in which high-quality $SrTiO_3$ film can be grown by considering the defect chemistry, to manage strontium and oxygen vacancies [15]. On a TiO_2 terminated $SrTiO_3$ (100) substrate, a 100 nm undoped $SrTiO_3$ buffer layer is first grown. After that, 1 at. % Nb doped $SrTiO_3$ is grown for various thicknesses in the range 3.9 nm $< d <$ 457 nm. A 100 nm undoped $SrTiO_3$ cap layer is grown above the doped layer, to prevent surface depletion [16]. The thicknesses of the films were calibrated by a stylus profiler.

Transport measurements were made using a standard four-probe method with sample cooling achieved using both a PPMS and a dilution refrigerator with an *in-situ* rotator. When the superconducting critical fields at low temperatures are being measured, a quasi d.c. current was used, which was kept far below the critical current I_c of the samples, typically $I \leq 0.05 I_c$ except for the bulk crystal measurement. The alignment for $\theta =$ 0 ° was better than 0.05 °, which is known from the minimum of the Hall voltage in

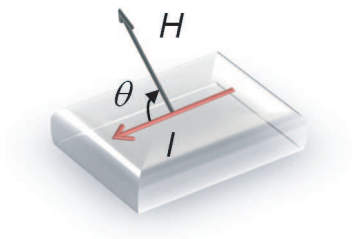

Figure 5.3: The definition of θ in the magnetoresistance measurement. H refers to the magnetic field, and I the current.

the parallel geometry. The samples were rotated with respect to the magnetic field as shown in Fig. 5.3, so that the current and magnetic field direction will be parallel at 0 ° to eliminating possible effects from the Lorentz force.

5.3 Dimensional Crossover of Superconductivity

Here, we will discuss the dimensionality of superconductivity in the samples, as probed by magnetotransport measurements in the dilution refrigerator. All samples are found to be superconducting with a transition temperature, T_c, in the range 250 mK $< T_c <$ 370 mK, and 10 %-90 % transition widths typically 24 mK, as shown in Fig. 5.4 (a). T_c was defined as the temperature at which the resistance fell to 50 % of the normal-state value. Careful treatment to eliminate a residual magnetic field was conducted before the measurement within an accuracy of $\pm$ 0.1 mT. Samples with thickness $d \geq 8.8$ nm showed relatively low T_c ($\sim$ 260 mK) with sharp 10 %-90 % widths ($\sim$ 10 mK). On the other hand, thinner samples with $d < 8.8$ nm showed a increased T_c with broadened 10 %-90 % widths, as shown in Fig. 5.4 (b). This increase will be discussed further in Sec. 5.4.2.

5.3.1 Temperature Dependence of the Upper Critical Field

At first, the temperature evolution of the upper critical field was measured for the perpendicular field geometry (θ = 90 °) and the parallel field geometry (θ = 0 °). The results are shown in Fig. 5.5. The upper critical field was defined as the field at which the resistance was half that of the normal state. In the perpendicular field geometry, all samples showed a linear temperature dependence, consistent with Eq. 5.5. In the parallel field geometry, one thick sample with d = 457 nm, and the bulk substrate showed the same linear temperature dependence as the perpendicular field geometry. For $d \leq 99$ nm, however, the temperature dependence was changed to a square root dependence as described by Eq. 5.6. This is a manifestation of the two-dimensional superconductor. Thus, it can be concluded that the dimensionality of superconductivity is changed from

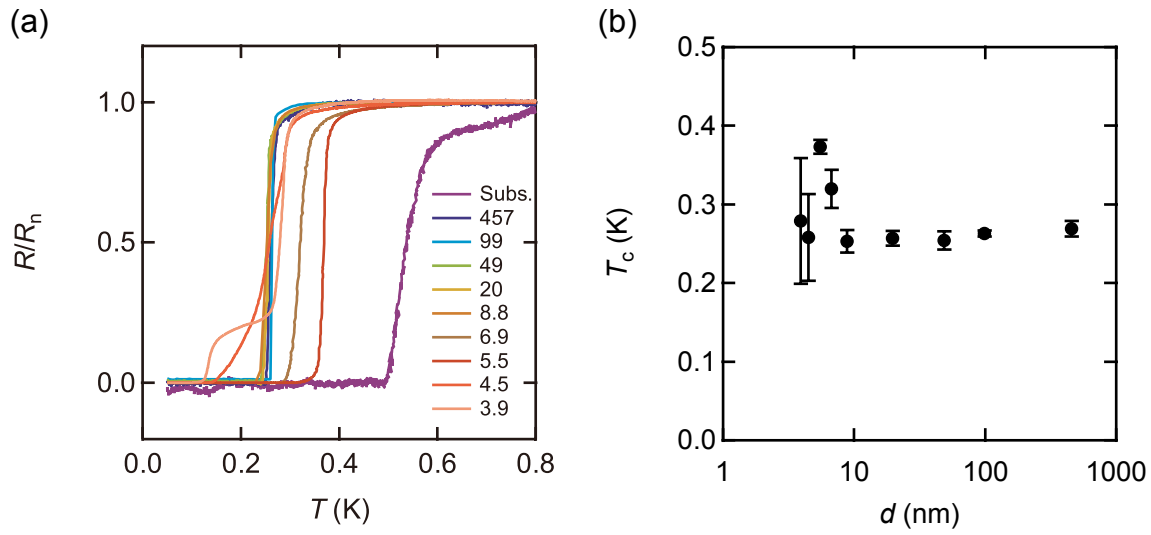

Figure 5.4: R-T curve and superconducting transition temperature. (a) Sheet resistance R normalized by the normal-state value $R_{\rm n}$ plotted as a function of temperature. Numbers in a legend refer to the thickness in nm. (b) Superconducting transition temperature $T_{\rm c}$ *vs* thickness d. $T_{\rm c}$ is defined by the half value of normal-state resistance, 10 %-90 % width of resistance is shown as an error bar of the temperature.

three dimensions to two dimensions for $d \leq 99$ nm.

5.3.2 Anisotropy of the Upper Critical Field

The anisotropy of the upper critical field was investigated by rotating the sample with respect to the magnetic field at $T = 50$ mK. The results are shown in Fig. 5.6 (a). As the growth thickness d decreases, a clear modulation of the upper critical field as a function of θ was found. Except for the bulk substrate, it was possible to fit the experimental data by Eq. 5.7. For the $d = 457$ nm sample, however, the calculated thickness of superconducting layer $d_{\rm Tinkham} = 218$ nm from Eq. 5.8, showed an inconsistency with the growth thickness. This indicates the failure of Tinkham's theory for this sample. This is expected from the result of the temperature dependence of the upper critical field, given that this sample is a three-dimensional superconductor.

Tinkham's model for the two-dimensional superconductor only stands when $d_{\rm Tinkham}$ is smaller than $\xi_{\rm GL}$. In Fig 5.6 (b), $d_{\rm Tinkham}$ and $\xi_{\rm GL}$ obtained from the the extrapolation of $H_{\rm c2}^{\perp}$ to $T = 0$ K, are plotted together. We found $\xi_{\rm GL} \approx 100$ nm for all samples, with a slight decrease for the thinner samples. Thus, the critical thickness for the three-dimensional to two-dimensional superconductivity crossover is estimated as $d_{\rm Tinkham} \sim \xi_{\rm GL} \sim 100$ nm, which is consistent with the measurement results of the temperature dependence of $H_{\rm c2}^{\parallel}$.

For thin films with $d \leq 8.8$ nm, the calculated superconducting layer thickness was slightly larger than the growth thickness. This can be understood because of the electron

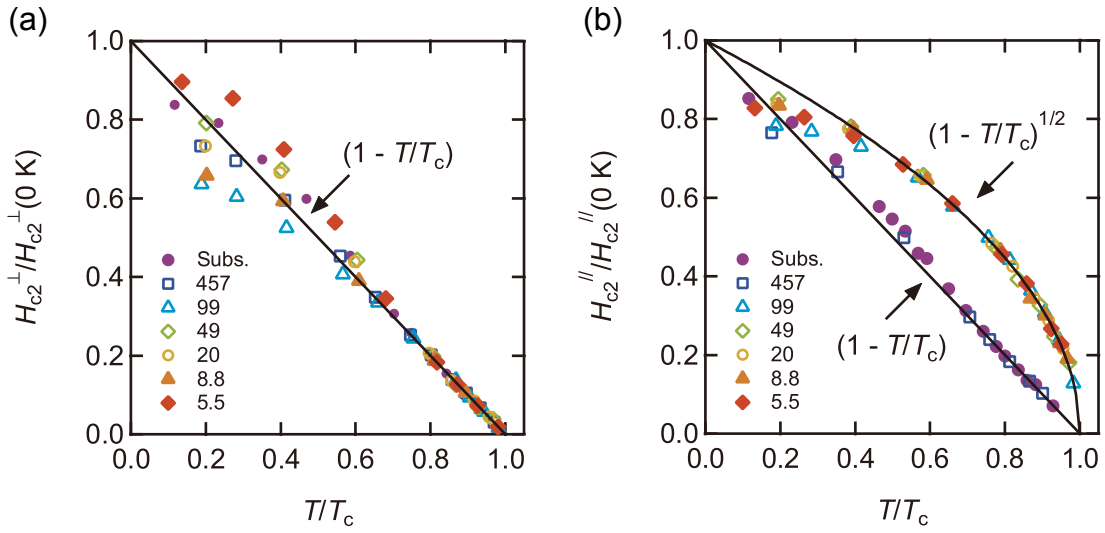

Figure 5.5: Temperature dependence of the upper critical field. Numbers in legends refer to the thickness in nm. (a) Normalized perpendicular upper critical field $H_{c2}^{\perp}/H_{c2}^{\perp}(0\ \mathrm{K})$ plotted as a function of the reduced temperature T/T_c. $H_{c2}^{\perp}(0\ \mathrm{K})$ was obtained by an extrapolated value to $T = 0$ K obtained from a fitting to Eq. 5.5 for (a) over the range of $0.7 < T/T_c < 1$. (b) Normalized parallel upper critical field with same fitting procedure using Eq. 5.6. A clear square root dependence is visible for samples with $d \leq 99$ nm.

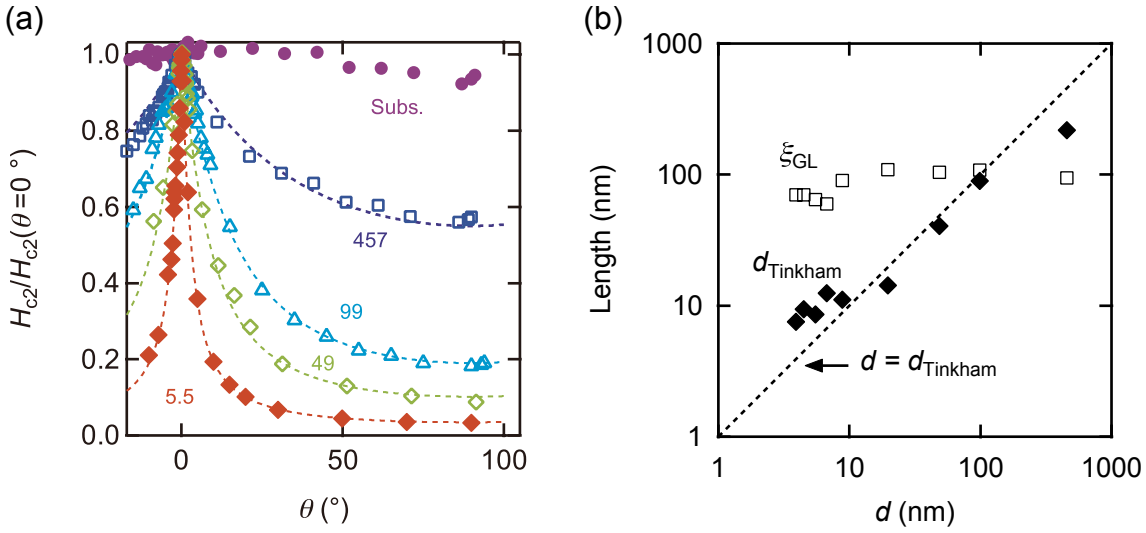

Figure 5.6: (a) Angular dependence of the upper critical field at 50 mK, normalized by the value at $\theta = 0$ °. As the thickness decreases, the anisotropy of the upper critical field becomes evident. Dotted lines are fits to Eq. 5.7. Numbers refer the growth thickness in nm. (b) Ginzburg-Landau coherence length ξ_{GL} (open squares) and $d_{Tinkham}$ (closed diamonds) *vs* growth thickness d. Dotted line is $d = d_{Tinkham}$.

wavefunction spreading outside of the dopant layer, due to the delta-doping effect. This will be discussed further in Sec. 5.4.

5.4 Novel Properties of the Delta-Doped Superconductor

Next, we will discuss the superconducting properties of the thinnest, delta-doped, $SrTiO_3$ heterostructure. We connect the findings in thin samples including the increase of the transition temperature and the increase of superconducting layer thickness beyond the growth thickness discussed in the above sections, to the novel properties of the delta-doped structure in terms of the mean free path.

5.4.1 Mean Free Path

In order to investigate the normal-state transport properties, measurements of magnetoresistance and Hall resistance were made at 2 K, as shown in Fig. 5.7. The sheet carrier density N_{2D} decreases and the mobility μ increases as the the thickness decreases. Supposing a three-dimensional Fermi sphere as a first approximation, the mean free path l was calculated for all samples from the Hall mobility and the three-dimensional Fermi velocity. This is plotted in Fig. 5.7 (b) along with the three-dimensional carrier density N_{3D}. We found that l increases as the thickness decreases, and N_{3D} decreases for $d < 20$ nm. The reduction of N_{3D} may mean that Nb atoms are less activated when the dopant layer is thinner, because Nb atoms in the outer part of the dopant layer face undoped $SrTiO_3$, allowing electrons to become more easily localized [17].

The increase of l is an important result, and contrary to conventional metal films, where l is strongly suppressed for decreasing thickness, as discussed in Sec. 5.1.2. The difference between the two systems can be understood as follows: electrons suffer diffusive scattering in metal thin films (Fig. 5.8 (a)), because they have an obvious interface or surface. However our system does not have a well defined interface or surface, so the electrons can scatter specularly from the Coulomb potential well without losing momentum (Fig. 5.8 (b)).

Additionally, the experiment results (Fig. 5.6 (b)) showing that the growth thickness d is less than the superconducting layer thickness d_{Tinkham} only for the thinner samples ($d \leq 8.8$ nm) indicates that the penetration effect of the electron wavefunction gives an increase of the width, as shown in schematically Fig. 5.8 (c). Because the width of the electron wavefunction is larger than the width of the dopant layer, the outer part of electron wavefunction may suffer less impurity scattering and as a result, the mean

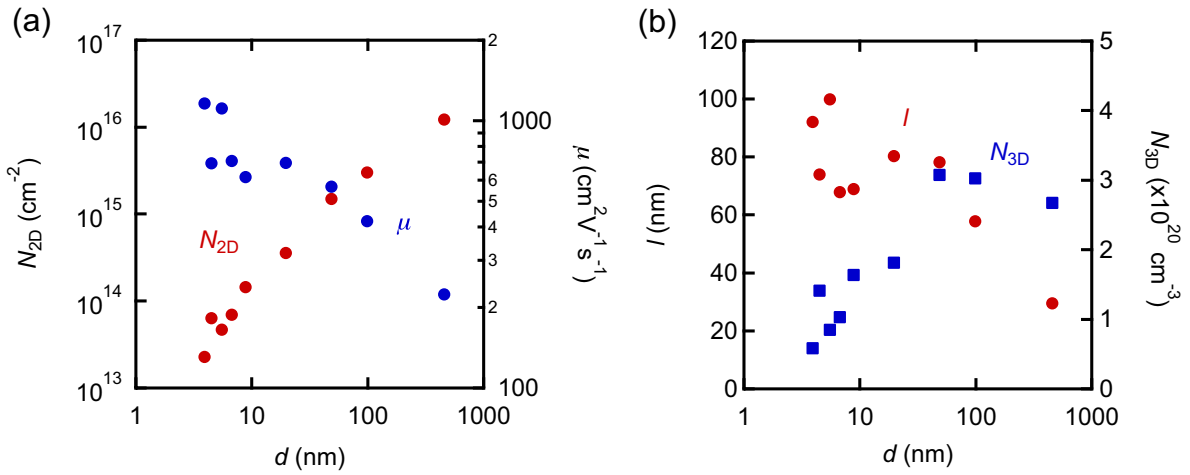

Figure 5.7: (a) Sheet carrier density N_{2D} and Hall mobility μ at 2 K, as a function of the growth thickness d. (b) Mean free path l and three-dimensional carrier density N_{3D} *vs* the growth thickness d. N_{3D} is calculated using the growth thickness d.

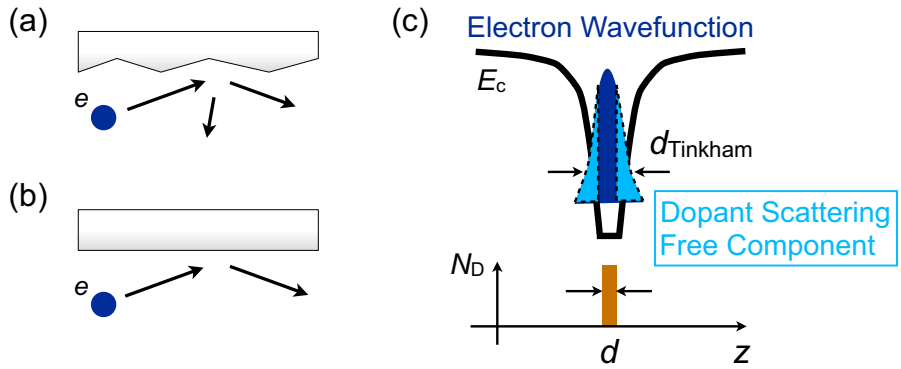

Figure 5.8: Schematic diagram of electron scattering in the delta-doped structure. (a) Diffusive scattering where the electrons lose momentum. (b) Specular scattering where the electrons scatter without a loss of momentum. (c) Penetration effect of the electron wavefunction in the delta-doped structure. N_D, dopant density, E_c, the conduction band, z, the growth direction.

free path increases. This result suggests that our samples are in a similar regime to delta-doped GaAs [18], as shown previously in Fig. 1.12 (b).

In reality, diffusion of Nb atoms may give similar effects to those described above. However, this is scenario may be ruled out from the following arguments. Theoretically, Nb atoms are relatively slow to diffuse because it is doped at the Ti-site of $SrTiO_3$, where the atom is bonded strongly with oxygen atoms [19]. Experimentally, no such increase of d_{Tinkham} was found for thicker samples (20 nm $< d <$ 100 nm), while more diffusion of Nb atoms is expected due to the longer growth times. An upper limit to the diffusion could be set by a second ion mass spectroscopy (SIMS) measurement: a film grown in the same conditions showed the diffusion of Nb atoms smaller than the resolution of the measurement $\sim$ 5 nm [20]. Further study, for example using cross-sectional scanning tunneling microscope (STM) [21], may give additional information to clarify this question.

5.4.2 Transition Temperature

In order to compare our results with the bulk superconducting phase diagram of bulk doped $SrTiO_3$, T_c as a function of $N_{2D}/d = N_{3D}$ and $N_{2D}/d_{\mathrm{Tinkham}}$ are plotted in Fig. 5.9. In thick samples with 8.8 nm $< d <$ 457 nm, T_c did not change although N_{3D} showed some variation. In samples with $d <$ 8.8 nm, the maximum of T_c is located at $N_{3D} = 10^{20}$ cm^{-3}, but shifted to the lower density region for the blue data points because d_{Tinkham} is larger than d. These data indicate that the change of T_c does not follow the bulk phase diagram, meaning that a simple change of the local three-dimensional carrier density is not the origin of the change in T_c.

One possibility is that the phonon structure has been altered in thin samples. While our sample does not have the granular problem, as in some metal thin films where increases in T_c have been reported [22], the nonlinear permittivity of $SrTiO_3$ can changes the phonon structure drastically. In theoretical subband calculations, which will be discussed in Sec. 6.5, as the electric field is increased, at a certain width of the potential well, the permittivity collapsed simultaneously from $>$ 20,000 to less than 100. Because the electron wavefunction exists inside and outside of the well, the different phonon structure it experiences could significantly change the net effective electron-phonon interaction. However, the superconductivity of bulk electron doped $SrTiO_3$ is an unresolved problem, and it is likely that the simple theory given by Eq. 5.2 is not appropriate. Thus it is not easy to obtain a quantitative link with the increase of T_c in our case. As a future perspective, tunneling experiments could provide important information about the phonon frequencies involved in superconductivity, and may be useful to reveal the mechanism of superconductivity in the delta-doped $SrTiO_3$ heterostructures.

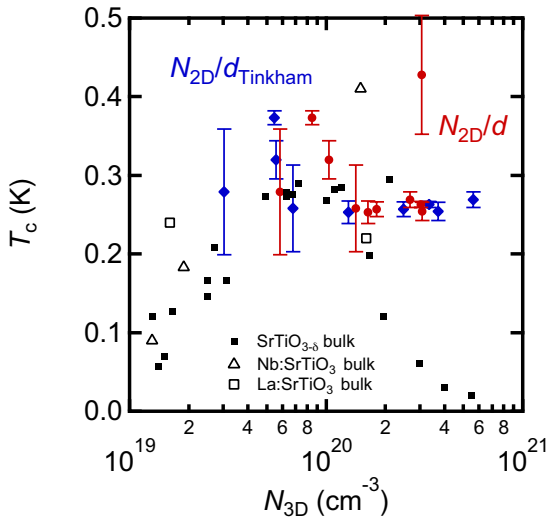

Figure 5.9: Superconducting phase diagram. Red points are N_{2D} divided by the growth thickness d. Blue points are N_{2D} divided by the superconducting thickness d_{Tinkham}. Error bars are the 10 %-90 % width of the R-T curve. Black closed squares are reduced $SrTiO_3$ (bulk) and opened triangles are bulk Nb:$SrTiO_3$, both taken from C. S. Koonce *et al.* [23]. Open squares are bulk La:$SrTiO_3$, taken from H. Suzuki *et al.* [24].

Another important change occurring in the thinner samples is a change in the topology of the Fermi surface from a three-dimensional Fermi sphere to a two-dimensional Fermi surface. Every relevant length scale of the thinnest sample ($d = 3.9$ nm) is larger than the thickness of superconducting layer, including the de-Broglie wavelength: $\lambda_{\mathrm{F}} = 5.3$ nm (assuming two dimensions). Thus, a two-dimensional Fermi surface is expected to appear, and experimentally has been confirmed from the two-dimensional quantum oscillations which will be discussed in Sec. 6.4. Although evidence that this affects T_{c} is not clear at present, this result opens up new possibilities to clarify the influence of the topology of the Fermi surface on superconductivity.

5.4.3 Violation of the Pauli Paramagnetic Limit

As discussed above, the usual case of BCS superconductivity assumes that the Cooper pairs are formed in spin-singlet states with opposite momentum. If a sufficiently large magnetic field is applied to the superconductor, the electron spins will tend to align parallel to the field, and the spin singlet Cooper pairs will be broken. If the energy gain from the applied field becomes larger than the superconducting condensation energy, superconductivity will be destroyed. This is called the Clogston-Chandrasekar limit or Pauli paramagnetic limit [25, 26]. The Pauli paramagnetic limiting field is given as

$$\mu_0 H_{\mathrm{c}}^{\mathrm{para}} = \Delta_0/\sqrt{2}\mu_{\mathrm{B}}, \tag{5.9}$$

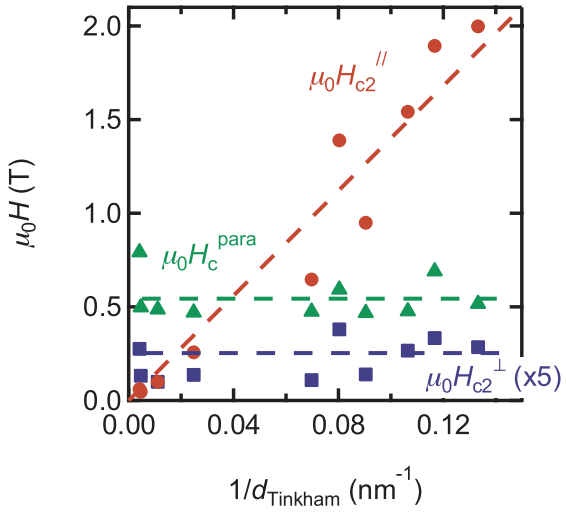

Figure 5.10: Upper critical fields and the violation of the Pauli paramagnetic limit. $H_{c2}^{\parallel}$ (red) and $H_{c2}^{\perp}$ (blue, scaled by factor of five). Green points show the Pauli paramagnetic limit H_c^{para} obtained from Eq. 5.9. Dashed lines are guides to the eye. $H_{c2}^{\parallel}$ increases proportionally to $1/d_{\mathrm{Tinkham}}$, whereas $H_{c2}^{\perp}$ and H_c^{para} remain almost the same. In the thinnest sample, $d = 3.9$ nm, H_c^{para} is about four times smaller than $H_{c2}^{\parallel}$.

where μ_0 is the vacuum permeability, $\mu_B = e\hbar/2m_e$ is the Bohr magneton, m_e is the electron mass, and $\Delta_0 = 1.76 k_B T_c$ is the BCS superconducting gap .

In the upper critical field measurements, we found a violation of the Pauli paramagnetic limit. The trend of $H_{c2}^{\parallel}$ and $H_{c2}^{\perp}$ as a function of the inverse superconducting layer thickness $1/d_{\mathrm{Tinkham}}$ is shown in Fig. 5.10. As d_{Tinkham} is reduced, $H_{c2}^{\parallel}$ becomes four times larger than the Pauli paramagnetic limit in the thinnest sample, while $H_{c2}^{\perp}$ remains almost same. The linear increase of $H_{c2}^{\parallel}$ with the inverse superconducting layer thickness can be derived from Eq. 5.8 if $H_{c2}^{\perp}$ is assumed to be constant. At present, however, the physical origin of the violation of the Pauli paramagnetic limit is not clear.

The violation of the Pauli paramagnetic limit has been found in many other systems, but its physical origin is still under discussion. One caution would be Eq. 5.9 is based on the most simple form of BCS theory. Considering that the superconducting properties of $SrTiO_3$ cannot be explained by conventional BCS theory (Eq. 5.1) or McMillan's formula (Eq. 5.2), the discrepancy with Eq. 5.9 is not unreasonable. One way, for example, to overcome the paramagnetic limit, is for the Cooper pairs to form with a different symmetry such as a triplet (p-wave) state thought to exist in Sr_2RuO_4 [27], or in systems with strong spin-orbit coupling which causes a spin-triplet superconductor component to be induced in the wavefunction [28]. Recently heavy fermion superconductors having no inversion symmetry are intensively studied because of its large upper critical field [29]. However, in our system the symmetrical potential of the delta-doping structure has no

effective electric field causing Rashba-type spin-orbit interaction [30]. Thus, it may not be the spin-orbit interaction that is the origin for the observed violation of the Pauli limit.

For future measurements, it would be interesting to see how large the upper critical field can be in the delta-doped structure by using a higher doping concentration of Nb:$SrTiO_3$, and thinner dopant layers. On the other hand, electric-field effect experiments with the current samples are also interesting, because the inversion symmetry can be broken and tuned by the external source.

5.5 Survey of the BKT Transition

The Berezinskii-Kousterlitz-Thouless (BKT) transition is a topological transition in two-dimensional superconductors driven by the long range interaction of vortex-antivortex pairs [31,32]. As a vortex-antivortex pair is produced by thermal excitation, the screening of the interaction between the vortex and antivortex pair can be increased by other pairs. Thus, the separation of the pairs occurs cooperatively, similar to the plasma transition. For $T > T_{\mathrm{BKT}}$, the density of the pairs, n_{f}, is given by [33]

$$n_{\mathrm{f}} \propto \exp\left[-2b\left(\frac{T_{\mathrm{c0}} - T_{\mathrm{BKT}}}{T - T_{\mathrm{BKT}}}\right)^{1/2}\right], \tag{5.10}$$

where b is a parameter reflecting the strength of the vortex-antivortex interaction, T_{c0} is the BCS critical temperature and T_{BKT} is the BKT transition temperature. This square-root-cusp temperature dependence is one of the characteristics of the BKT transition.

When a current is driven through the system, the direction of Lorentz force acting on a vortex and an antivortex is opposite, and a separation of the pair occurs at sufficiently high current density. When the temperature is equal to T_{BKT}, the critical exponent of the current-voltage characteristic jumps from 1 to 3, leading to $I \propto V^3$. This has been used as one of the common methods of identifying the value of T_{BKT}. The characteristic change in the I-V curves has been recently discussed in the case of two-dimensional superconductivity at the $LaAlO_3/SrTiO_3$ interface [34], as shown in Fig. 5.11, where good agreement between T_{c0}, and T_{BKT} measured via the $R(T)$ and I-V curves was found.

In a delta-doped sample ($d = 5.5$ nm) and a thick sample ($d = 457$ nm), I-V characteristics were measured and the results are shown in Fig. 5.12. In both samples, we could find a region with non-linear I-V close to the transition temperature. The changes of the critical exponent are rather continuous similar to the result of the $LaAlO_3/SrTiO_3$ shown in Fig. 5.11 (b). For the thicker sample, this is rather unexpected result if one thinks that the BKT transition is found only in two-dimensional superconducting transitions.

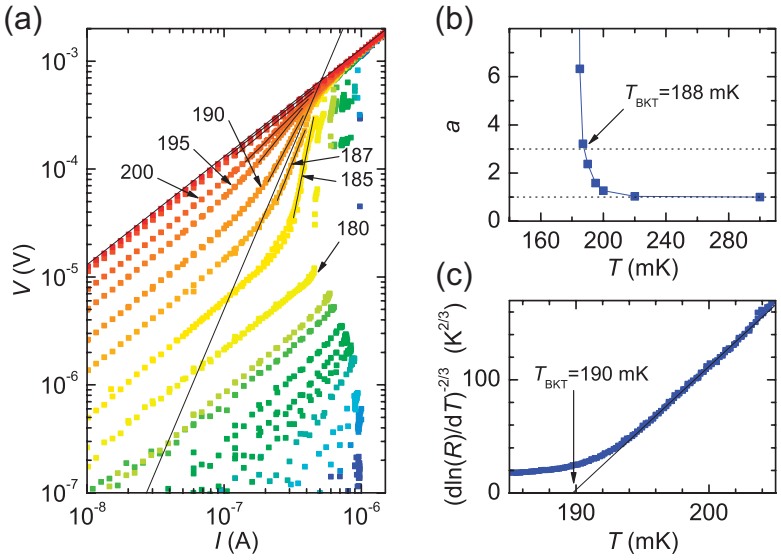

Figure 5.11: BKT transition in the $LaAlO_3/SrTiO_3$ interface, taken from N. Reyren *et al.* [34]. (a) I-V curves on a logarithmic scale. The numbers give T, measured in mK. The short black lines are fits of the data in the transition. The long black line corresponds to $V \sim I^3$, and show that 187 mK $< T_{\mathrm{BKT}} <$ 190 mK. (b) Temperature dependence of the power-law exponent a, as deduced from the fits shown in (a). (c) R(T) dependence. The solid line is the behavior expected for a BKT transition with $T_{\mathrm{BKT}} = 190$ mK.

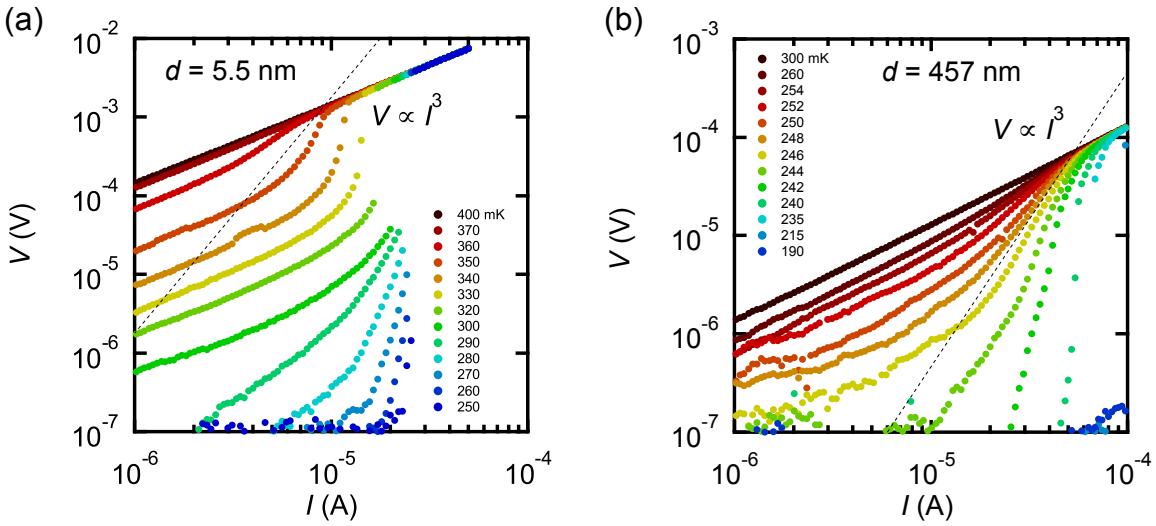

Figure 5.12: I-V characteristics of $SrTiO_3/Nb{:}SrTiO_3/SrTiO_3$ Heterostructures. (a) Sample with $d = 5.5$ nm. (b) Sample with $d = 457$ nm sample. In both samples, near the transition temperature, nonlinear I-V is seen. Dotted line is $I \propto V^a$ for $a = 3$.

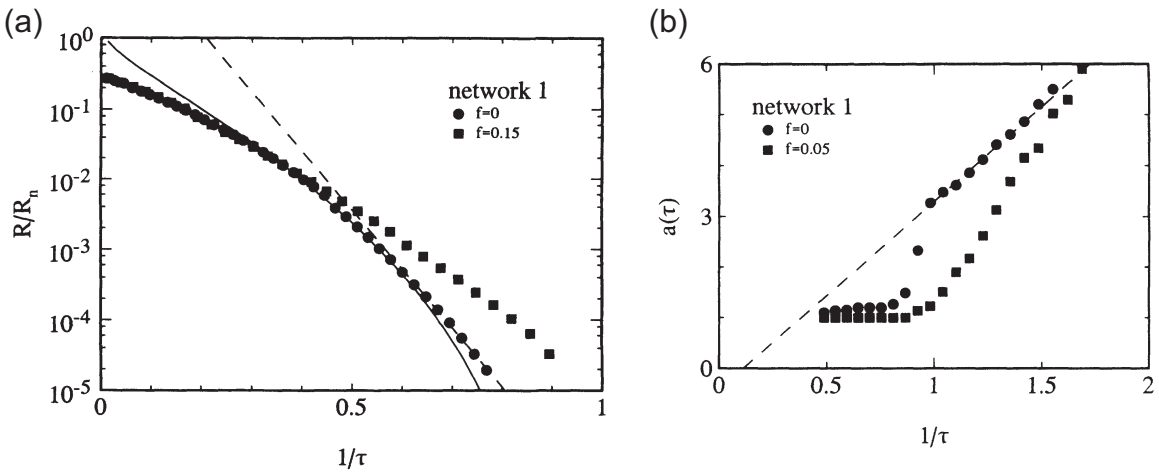

Figure 5.13: Characteristics of the BKT transition in a superconducting wire network having large normal-state resistance, taken from H. S. J. van der Zant *et al.* [35]. f is the applied flux per cell divided by the flux quantum, τ is a normalized temperature, which is unity at $T = T_{\mathrm{BKT}}$. (a) Temperature dependence of the resistance, which is fitted by the square-root-cusp temperature dependence of the vortex-antivortex pair for $T > T_{\mathrm{BKT}}$. (b) The universal jump of the critical component from 1 to 3 is shown at T_{BKT}.

Considering also that the BKT transition should show the critical component of the current jumped from 1 to 3, as shown in Fig. 5.13, it is concluded that BKT transition may not be consistent with our observations from the I-V measurements. This inconsistency may come from the temperature dependence of the order parameter, which cannot be neglected in superconducting thin films [36].

5.6 Summary

In this chapter, the superconducting properties of $SrTiO_3$/Nb:$SrTiO_3$/$SrTiO_3$ heterostructures were investigated. As the doped layer became thinner, a crossover of superconductivity from three-dimensional to two-dimensional was found with a critical thickness of $\sim$ 100 nm consistent with estimates of ξ_{GL}. As the doped layer thickness reached a few nm, several interesting properties were found: an enhancement of the mean free path was clear, indicating reduced scattering in the delta-doped structure, i.e. the wavefunction spreading out from the dopant plane. An increase of T_{c} was also found, which may be explained by a change in the the phonon structure or the topology of the Fermi surface. In the thinnest sample (d = 3.9 nm) we found that parallel upper critical field is four times larger than the Pauli paramagnetic limiting field. Finally, we found the non-linearity of the I-V characteristics near the transition temperature in both the two-dimensional and three-dimensional superconducting samples, which may not consistent with the conventional BKT transition.

From this study, we successfully doped a few nm of thickness of $SrTiO_3$ to form a superconductor, demonstrating the delta-doping technique is feasible in this system. It is possible to realize more complex heterostructures with the delta-doping technique, for example a delta-doped superconductor superlattice, in analogy to the copper-oxide superconductors, which are layered superconductors. The role of inter-layer coupling between the two-dimensional superconductor layers may be elucidated with careful control of the inter-layer distance between the superconducting layers.

References

[1] P. W. Anderson, Interlayer Tunneling Mechanism for High-T_c Superconductivity: Comparison with c Axis Infrared Experiments, *Science* **268**, 1154 (1995).

[2] J. G. Bednorz and K. A. Muller, Perovskite-Type Oxides - the New Approach to High-T_c Superconductivity, Nobel Lecture, December 8, 1987.

[3] J. K. Hulm, M. Ashkin, D. W. Deis, and C. K. Jones, Superconductivity in Semiconductor and Semimetals, *Prog. Low Temp. Phys.* **6**, 205 (1970).

[4] K. Ueno, S. Nakamura, H. Shimotani, A. Ohtomo, N. Kimura, T. Nojima, H. Aoki, Y. Iwasa, and M. Kawasaki, Electric-Field-Induced Superconductivity in an Insulator, *Nature Mater.* **7**, 855 (2008).

[5] P. W. Anderson, Theory of Dirty Superconductors, *J. Phys. Chem. Solids.* **11**, 26 (1959).

[6] J. M. Graybeal and M. R. Beasley, Localization and Interaction Effect in Ultrathin Amorphous Superconducting Films, *Phys. Rev. B* **29**, 4167 (1984).

[7] A. F. Hebard and M. A. Paalanen, Pair-Breaking Model for Disorder in Two-Dimensional Superconductors, *Phys. Rev. B* **30**, 4063 (1984).

[8] A. M. Goldman and N. Markovic, Superconductor-Insulator Transitions in the Two-Dimensional Limit, *Phys. Today* **226**, 39 (1998).

[9] P. Phillips and D. Dalidovich, The Elusive Bose Metal, *Science* **302**, 243 (2003).

[10] M. M. Ozer, Y. Jia, Z. Zhang, J. R. Thompson, and H. H. Weitering, Tuning the Quantum Stability and Superconductivity of Ultrathin Metal Alloys, *Science* **316**, 1594 (2007).

[11] A. M. Finkelstein, Suppression of Superconductivity in Homogeneously Disordered Systems, *Physica B* **197**, 636 (1994).

[12] G. J. Dolan, Critical Thicknesses for the Transition from Intermediate- to Mixed-State Behavior in Superconducting Thin Films of Pb, Sn, and In, *J. Low Temp. Phys.* **15**, 133 (1973).

[13] M. Tinkham, Effect of Fluxoid Quantization on Transitions of Superconducting Films, *Phys. Rev.* **129**, 2413 (1963).

[14] F. E. Harper and M. Tinkham, The Mixed State in Superconducting Thin Films, *Phys. Rev.* **172**, 441 (1968).

[15] Y. Kozuka, M. Kim, C. Bell, B. G. Kim, Y. Hikita, and H. Y Hwang, Two-Dimensional Normal-State Quantum Oscillations in a Superconducting Heterostructure, *Nature* **462**, 487 (2009).

[16] A. Ohtomo and H. Y. Hwang, Surface Depletion in Doped $SrTiO_3$ Thin Films, *Appl. Phys. Lett.* **84**, 1716 (2004).

[17] H. -J. Gossmann and F. C. Unterwald, Dopant Electrical Activity and Majority-Carrier Mobility in B- and Sb-δ-doped Si thin films, *Phys. Rev. B* **19**, 12618 (1992).

[18] E. F. Schubert, *Delta-Doping of Semiconductors*, (Cambridge Univ. Press, Cambridge, 1996).

[19] R. A. De Souza, M. S. Islam, and E. Ivers-Tiffee, Formation and Migration of Cation Defects in the Perovskite Oxide $LaMnO_3$, *J. Mater. Chem.* **9** 1621 (1999).

[20] Y. Kozuka, Y. Hikita, and H. Y. Hwang, *unpublihsed*.

[21] M. B. Johnson, P. M. Koenraad, W. C. van der Vleuten, H. W. M. Salemink, and J. H. Wolter, Be Delta-Doped Layers in GaAs Imaged with Atomic Resolution Using Scanning Tunneling Microscopy, *Phys. Rev. Lett.* **75**, 1606 (1995).

[22] M. Strongin, O. F. Kammerer, J. E. Crow, R. D. Parks, D. H. Douglass, Jr., and M. A. Jensen, Enhanced Superconductivity in Layered Metallic Films, *Phys. Rev. Lett.* **21**, 1320 (1968).

[23] C. S. Koonce, M. L. Cohen, J. F. Schooley, W. R. Hosler, and E. R. Pferifer, Superconducting Transition Temperatures of Semiconducting $SrTiO_3$, *Phys. Rev.* **163**, 380 (1967).

[24] H. Suzuki, H. Bando, Y. Ootuka, I. H. Inoue, T. Yamamoto, K. Takahashi, and Y. Nishihara, Superconductivity in Single-Crystalline $Sr_{1-x}La_xTiO_3$, *J. Phys. Soc. Jpn.* **65**, 1529 (1996).

[25] B. S. Chandrasekhar, A Note on the Maximum Critical Field of High-Field Superconductors, *Appl. Phys. Lett.* **1**, 7 (1962).

[26] A. M. Clogston, Upper Limit for the Critical Field in Hard Superconductors, *Phys. Rev. Lett.* **9**, 266 (1962).

[27] A. P. Mackenzie and Y. Maeno, The Superconductivity of Sr_2RuO_4 and the Physics of Spin-Triplet Pairing, *Rev. Mod. Phys.* **75**, 657 (2003).

[28] X. S. Wu, P. W. Adams, Y. Yang, and R. L. McCarley, Spin Proximity Effect in Ultrathin Superconducting Be-Au Bilayers, *Phys. Rev. Lett.* **96**, 127002 (2006).

[29] E. Bauer, G. Hilscher, H. Michor, C. Paul, E. W. Scheidt, A. Gribanov, Y. Seropegin, H. Noel, M. Sigrist, and P. Rogl, Heavy Fermion Superconductivity and Magnetic Order in Noncentrosymmetric $CePt_3Si$, *Phys. Rev. Lett.* **92**, 027003 (2004).

[30] Y. A. Bychkov and E. I. Rashba, Oscillatory Effects and the Magnetic Susceptibility of Carriers in Inversion Layers, *J. Phys. C* **17**, 6039 (1984).

[31] V. L. Berezinskii, *Sov. Phys. JETP*, **34**, 610 (1972).

[32] J. M. Kosterlitz and D. J. Thouless, Ordering, Metastability and Phase Transitions in Two-dimensional Systems, *J. Phys. C* **6**, 1181 (1973).

[33] J. E. Mooij, in *Percolation, Localization and Superconductivity*, edited by A. M. Goldman and S. Wolf, (Plenum, New York, 1983), p. 325.

[34] N. Reyren, S. Thiel, A. D. Caviglia, L. Fitting Kourkoutis, G. Hammerl, C. Richter, C. W. Schneider, T. Kopp, A. -S. Ruetschi, D. Jaccard, M. Gabay, D. A. Muller, J. -M. Triscone, and J. Mannhart, Superconducting Interfaces Between Insulating Oxides, *Science* **317**, 1196 (2007).

[35] H. S. J. van der Zant, M. N. Webster, J. Romijn, J. E. Mooji, Vortices in Two-Dimensional Superconducting Weakly Coupled Wire Network, *Phys. Rev. B* **50**, 340 (1994).

[36] Y. Iye, *Superconductivity*, (Asakura Publishing Co., Ltd., Tokyo, 2005).

Chapter 6

Two-Dimensional Quantum Oscillations in a Delta-Doped $SrTiO_3$ Heterostructure

Semiconductor heterostructures provide an ideal platform for studying high-mobility, low-density electrons in reduced dimensions [1–4]. The realization of superconductivity in heavily doped diamond [5], silicon [6], silicon carbide [7] and germanium [8] suggests that Cooper pairs eventually may be directly incorporated in semiconductor heterostructures [9], but these newly discovered superconductors are currently limited by their extremely large electronic disorder. Similarly, the electron mean free path in low-dimensional superconducting thin films is usually limited by interface scattering, in single-crystal or polycrystalline samples, or atomic-scale disorder, in amorphous materials, confining these examples to the extreme dirty limit [10]. Here we report the fabrication of a high-quality superconducting layer within a thin-film heterostructure based on $SrTiO_3$ (the first known superconducting semiconductor [11]). By selectively doping a narrow region of $SrTiO_3$ with the electron-donor niobium, we form a superconductor that is two-dimensional, as probed by the anisotropy of the upper critical magnetic field. Unlike in previous examples, however, the electron mobility is high enough that the normal-state resistance exhibits Shubnikov-de Haas oscillations that scale with the perpendicular field, indicating two-dimensional states. These results suggest that delta-doped $SrTiO_3$ provides a model system in which to explore the quantum transport and interplay [12] of both superconducting and normal electrons.

6.1 Introduction

A key point of the technique of delta-doping [13] is the reduction of the dopant-layer thickness to below the other characteristic lengths in the system, such as the electronic mean free path, l_{mfp}. In this limit, the electron-wavefunction weight in the nearby undoped

regions can be significant, leading to a reduction in electron scattering by ionized impurities and an enhanced mobility relative to a uniformly doped thin film [14]. In the case of $SrTiO_3$, its extremely large dielectric constant at low temperatures [15–17] also allows effective impurity screening, leading to further improvements in the transport properties. $SrTiO_3$ can also be electron-doped to become a superconductor with the lowest known carrier density of any material [18]. For these reasons, this material is increasingly being used to investigate novel phenomena in field-effect devices [19–21]. However, all of these devices rely on electron confinement close to some form of interface, where such lattice screening is not fully effective. Furthermore, high-mobility doped $SrTiO_3$ thin films have until now been unavailable for the study of transport in more complex heterostructures. Recently, we developed a reliable technique to make high-quality niobium-doped $SrTiO_3$ thin films with transport properties similar to the highest-quality single crystals. In this chapter, we investigate low-temperature quantum transport properties, superconductivity and Shubnikov-de Haas oscillations, of a delta-doped $SrTiO_3$ heterostructure.

6.2 Sample Growth and Measurement

We grew the sample by pulsed laser ablation in an atmosphere of less than 10^{-8} torr of oxygen at 1,200 °C. Single-crystal $SrTiO_3$ and Nb:$SrTiO_3$ (1 atomic %) targets were used together with an $SrTiO_3$ (100) substrate. After growth, the sample was annealed in situ at 900 °C under an oxygen partial pressure of 10^{-2} torr for 30 min to refill oxygen vacancies in the $SrTiO_3$ layers. We ultrasonically wire-bonded the sample with aluminium wire and then made magnetotransport measurements in a dilution refrigerator (Kelvinox MX400, Oxford Instruments Co.) with a base temperature of 10 mK, as calibrated using a ^{60}Co nuclear-orientation thermometer, and a pumped ^{3}He cryostat. *In situ* angular rotation could be performed with a relative accuracy of better than 0.05 °, with $\theta = 0$

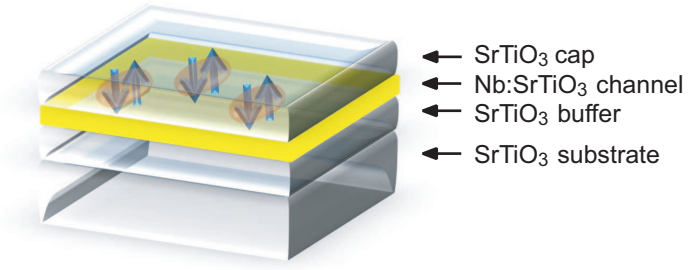

Figure 6.1: Sample structure. A sketch of the delta-doped Nb:$SrTiO_3$ layer sandwiched between insulating $SrTiO_3$ buffer and cap layers on an $SrTiO_3$ substrate. Cooper pairs forming the superconducting layer in the delta-doped layer are shown schematically.

° defined by the minimum of the Hall voltage. The sample was measured with a 16-Hz a.c. current bias of 100 nA, which was far below the superconducting critical current of 35.9 mA at $T = 50$ mK as measured by d.c. methods.

In the work reported here, our sample consisted of a thin-film heterostructure with 100-nm-thick undoped $SrTiO_3$ layers above and below a Nb:$SrTiO_3$ layer that was nominally 5.5 nm thick, as sketched in Fig. 6.1. The motivation behind this design was the desire to remove the effects of surface depletion [22], as well as any electron scattering arising at the surface and, possibly, at the film-substrate interface. Thus, we have a narrow conducting channel with no physical interface controlling the wavefunction of the electrons, as it is only the fixed-charge potential of the dopants that confines them.

6.3 Transport Properties of the Delta-Doped $SrTiO_3$ Heterostructure

The basic transport properties of the sample is shown in Fig. 6.2 (b): the low-field Hall mobility at $T = 2$ K was 1,100 $cm^2V^{-1}s^{-1}$ and the carrier density was $N_s = 4.73 \times 10^{13}$ cm^{-2}. If we simply assume that charge was uniformly distributed throughout the 5.5-nm Nb:$SrTiO_3$ layer, this gives a three dimensional carrier density of $N_{3D} = 8.53 \times 10^{19}$ cm^{-3}. This value is within the range for which Nb:$SrTiO_3$ is superconducting [11], which we confirmed by dilution-refrigerator measurements (Fig. 6.2 (b)) showing a clear superconducting transition with midpoint at $T_c = 370$ mK and a 10-90% width of 18 mK.

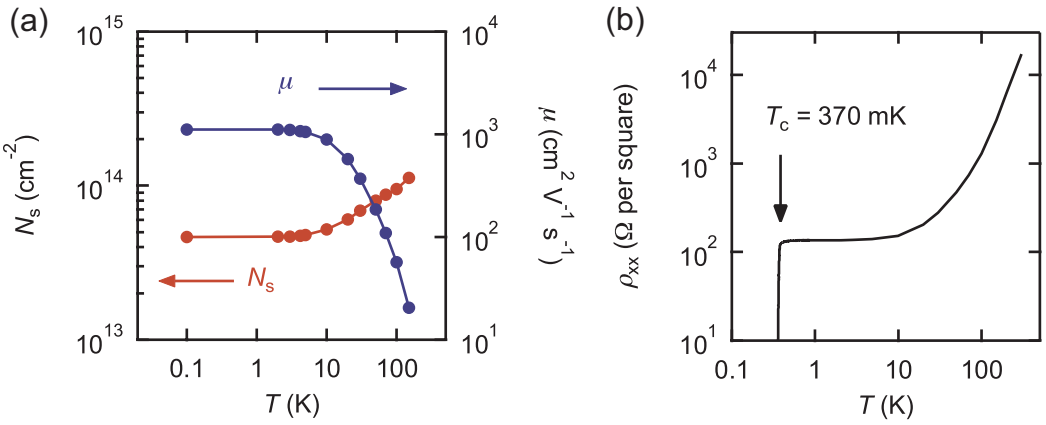

Figure 6.2: Transport characterization and superconducting transition. (a) Low-field sheet carrier density, N_s (red), and electron Hall mobility, μ (blue), versus temperature. (b) Sheet resistance, ρ_{xx}, versus temperature, showing a clear superconducting transition at 370 mK.

6.3.1 Two-Dimensional Superconducting Properties

To investigate the nature of the superconductivity in this structure further, we measured the superconducting upper critical field, H_{c2}, at various angles, θ, between the sample plane and the magnetic field (Fig. 6.3 (a)), finding a strong anisotropy between the parallel critical field ($\theta = 0$ °), $\mu_0 H_{c2}^{\parallel}$ (T) = 1.87 T, and the perpendicular critical field ($\theta = 90$ °), $\mu_0 H_{c2}^{\perp}$ (T) = 0.061 T, where μ_0 is the vacuum permeability. This is a consequence of the thickness of the superconducting layer being much thinner than the Ginzburg-Landau coherence length, ξ_{GL}, meaning that superconductivity in this type-II material cannot be suppressed by vortex entry for in-plane fields. From measurements of the temperature dependence of $H_{c2}^{\perp}$, we can directly extract ξ_{GL} using the linearized Ginzburg-Landau form, Eq. 5.5. This fit (Fig. 6.3 (b)) gives $\xi_{GL}(0) = 61.2 \pm 1.4$ nm. Also the temperature dependence of $H_{c2}^{\parallel}$ for a two-dimensional superconductor is given by Eq. 5.6. This characteristic square root dependence corresponds accurately with our data. From this fit, we extract a superconducting thickness of $d_{\text{Tinkham}} = 8.4 \pm 0.1$ nm. This value is in reasonable correspondence with the growth thickness if we consider that the wave function spreading into the undoped $SrTiO_3$ will tend to increase the effective thickness of the delta layer [13] (see Sec. 6.5). Furthermore, a careful fitting of the full $H_{c2}(\theta)$ data using the formula Eq. 5.7 first derived in [23], shows good agreement, as illustrated in Fig. 6.3 (c).

6.4 Two-Dimensional Shubnikov-de Haas Oscillations

Next we turn to the normal-state properties above the critical field at which superconductivity is suppressed. For $\mu_0 H$ = 5-14 T, we observed Shubnikov-de Haas quantum oscillations in the transverse geometry, superimposed on a background of positive magnetoresistance (Fig. 6.4 (a)) and periodic in $1/H$. After the magnetoresistance background has been subtracted, measurements for various values of θ show a clear scaling of the peak positions with the reciprocal perpendicular component of the magnetic field, that is, with $1/H_{\perp} = 1/H\sin\theta$, as is evident from a comparison of Figs. 6.4 (b) and (c). This feature is critical, and demonstrates that the Shubnikov-de Haas oscillations are due to orbits around a cylindrically shaped Fermi surface, indicative of quantum transport in two-dimensional systems. Thus, for this sample, we find two-dimensional superconductivity at low magnetic fields and Shubnikov-de Haas oscillations due to a two-dimensional Fermi surface topology at high magnetic fields. Although many two-dimensional superconductors have been formed from three-dimensional materials using thin films, they have generally been characterized by very low values of l_{mfp}. For example, in amorphous

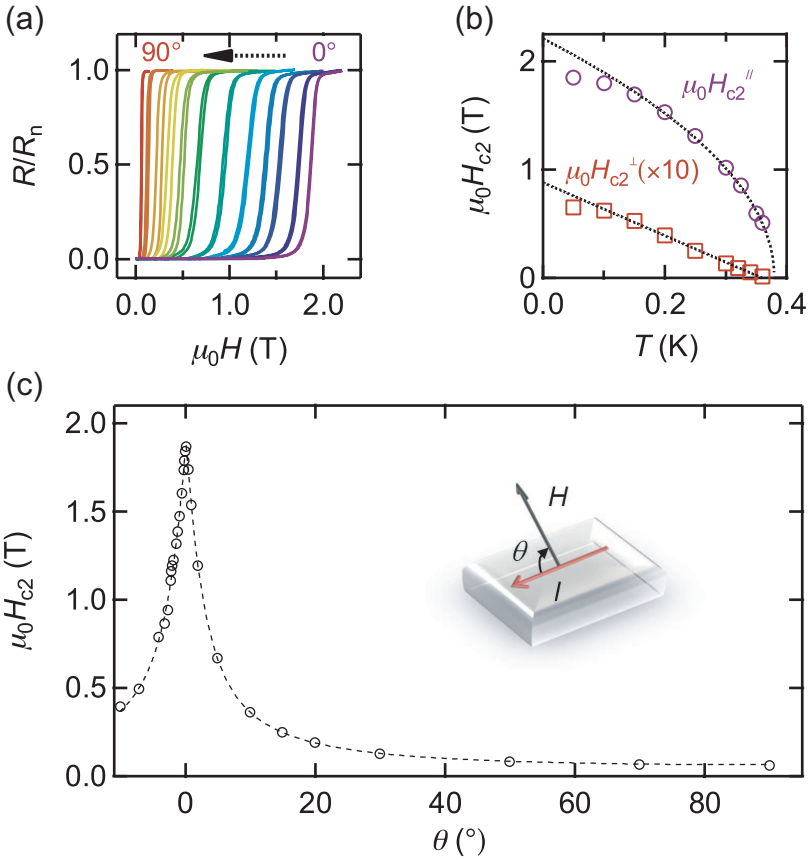

Figure 6.3: Two-dimensional superconducting characteristics. (a) Measurement of the superconducting upper critical field, H_{c2}, using resistance versus magnetic field, H, for various angles between the sample plane and the magnetic field at $T = 50$ mK. R_n, normal-state resistance. (b) H_{c2} versus temperature for H applied perpendicular to the sample plane (squares; field data multiplied by ten for clarity) and parallel to the plane (circles). Dashed lines are fits to linearized Ginzburg-Landau theory. (c) Full angular dependence of H_{c2} ($H_{c2}(\theta)$), where the dashed line is a fit to equation (1). The sketch defines the angle between the sample plane and the applied magnetic field. I, current.

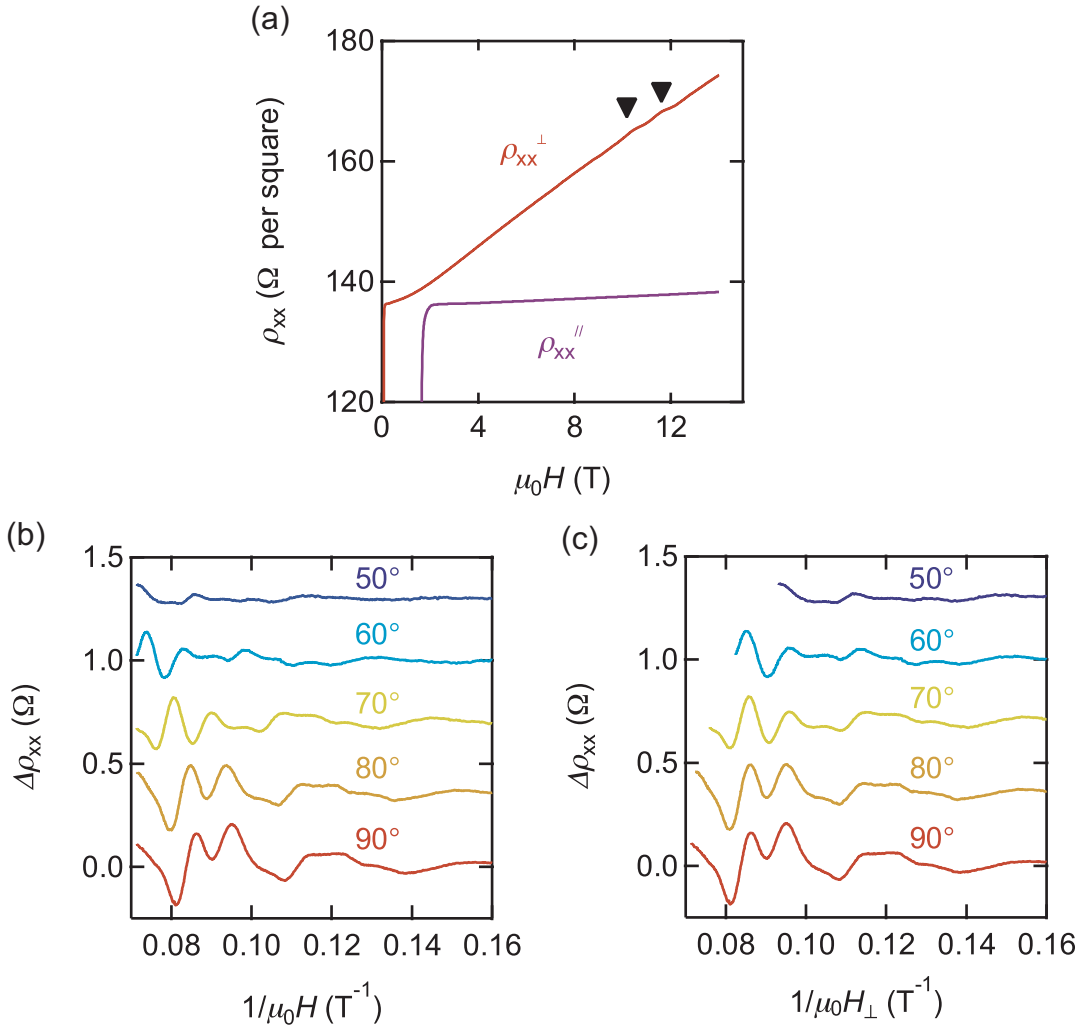

Figure 6.4: Two-dimensional quantum oscillations in the normal state. (a) Longitudinal resistivity in the perpendicular ($\rho_{xx}^{\perp}$) and parallel ($\rho_{xx}^{\parallel}$) geometry, from $\mu_0 H$ = 0-14 T at T = 100 mK. Shubnikov-de Haas oscillations are visible (arrowheads) in $\rho_{xx}^{\perp}(H)$. The sudden increase in ρ_{xx} at low fields is due to the superconducting upper critical field being crossed. (b), (c), Amplitude of the Shubnikov-de Haas oscillations, $\Delta\rho_{xx}$, after background subtraction, for various angles at T = 100 mK, versus the reciprocal total magnetic field (b) and the reciprocal perpendicular magnetic field component ($1/\mu_0 H_{\perp}$; (c)).

bismuth, the electrons are scattered on an atomic scale, resulting in single-electron transport that is completely incoherent and diffusive [10]. Nevertheless, these systems are superconducting, albeit in the dirty limit, reflecting the robustness of superconductivity to disorder. By contrast, the Shubnikov-de Haas oscillations we demonstrate in our artificial two-dimensional superconductor are made possible by the high crystalline coherence and lack of interface or surface scattering.

From a Fourier transform of the Shubnikov-de Haas oscillations in terms of $1/\mu_0 H$ in the range 5 T$< \mu_0 H <$14 T (Fig. 6.5 (a)), it is clear that more than one frequency is observed in the oscillations. Nominal peak assignments by Lorentzian fitting give three primary components (Fig. 6.5 (a)). These correspond to respective sheet carrier densities, N_{SdH}, of 1.83×10^{12} cm^{-2}, 3.63×10^{12} cm^{-2} and 4.83×10^{12} cm^{-2} (representing 0.14, 0.27 and 0.37% of the Brillouin zone, respectively), calculated using the free carrier approximation assuming spin degeneracy. Thus, N_{s}, the sheet carrier density derived from the Hall data, and N_{SdH} show significant disagreement. This suggests that in addition to the intrinsic conduction band structure of $SrTiO_3$, which is composed of three non-degenerate pockets at the zone center [24], there is a complex electronic structure originating from multi-subband occupancy. We must therefore be cautious in drawing strong conclusions from analysis based on a single band picture: detailed band structure calculations are necessary to shed light on the true energy level diagram of our delta-doped system, taking into account the nonlinear response of the $SrTiO_3$ permittivity [15]. An approximate model indicates that three light-electron subbands are occupied, as well as four heavy and two spinorbit-split subbands (see Sec. 6.5). Accordingly, we may conclude that the discrepancy between N_{s} and N_{SdH} arises because only selected subbands in some of the electron pockets contribute to the Shubnikov-de Haas oscillations, as a result of different effective masses and/or scattering times. Nevertheless, the Shubnikov-de Haas oscillations in Fig. 6.4 (c) clearly show that a high-mobility two-dimensional electron gas can be created in a superconducting oxide heterostructure.

6.4.1 Effective Mass and Quantum Scattering Time Analysis

To estimate the effective mass, m^*, and the Dingle temperature, T_{D}, of the two-dimensional electron gas, we measured the temperature dependence of the Shubnikov-de Haas oscillations (Fig. 6.5 (b)) and analyzed it in two different ways. First we chose the oscillation peak at $\mu_0 H = 11.4$ T ($1/\mu_0 H = 0.087$ T^{-1}) and fitted the Shubnikov-de Haas amplitude using the form [2]

$$\Delta\rho_{\mathrm{xx}} = 4\rho_0 \exp(-2\pi^2 k_{\mathrm{B}} T_{\mathrm{D}}/\hbar\omega_{\mathrm{c}}) \frac{2\pi^2 k_{\mathrm{B}} T/\hbar\omega_{\mathrm{c}}}{\sinh(2\pi^2 k_{\mathrm{B}} T/\hbar\omega_{\mathrm{c}})}, \tag{6.1}$$

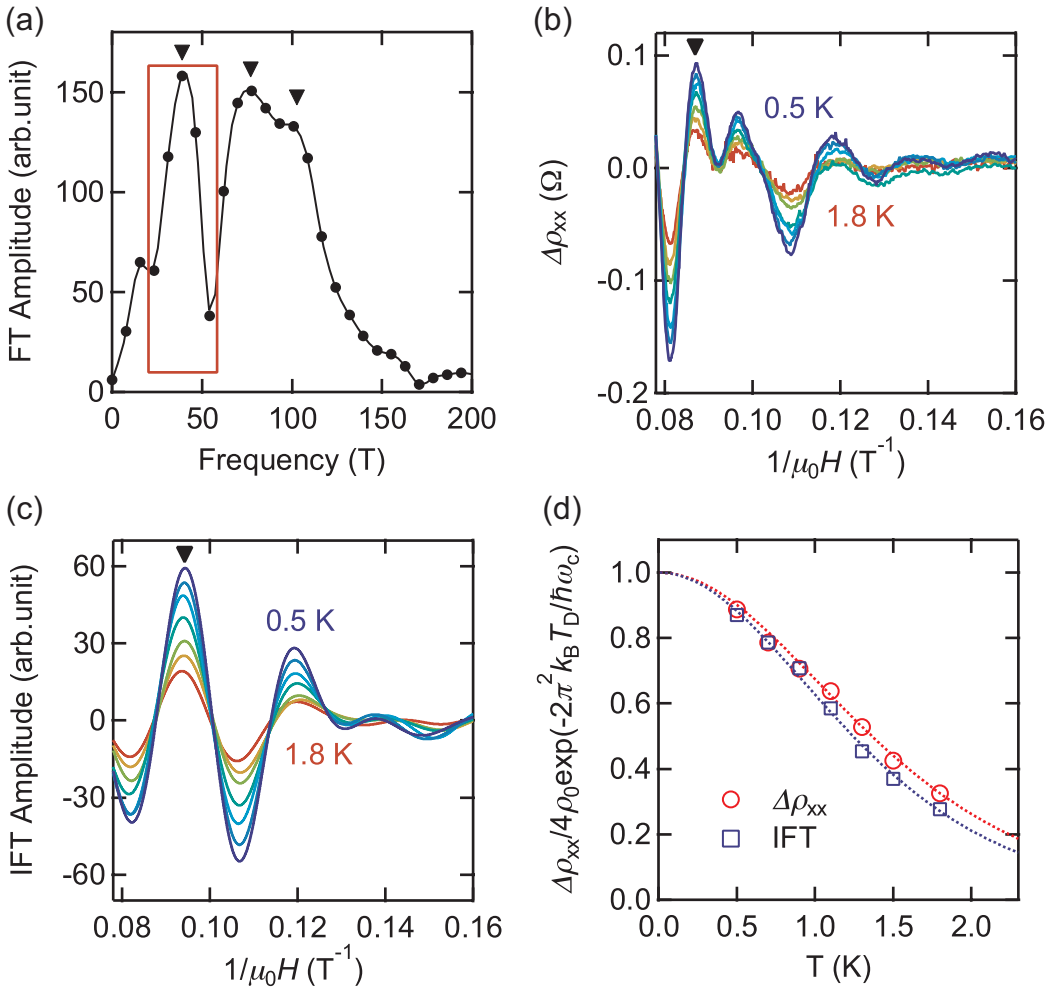

Figure 6.5: Carrier effective mass. (a) Fourier transform (FT) of the Shubnikov-de Haas oscillations at $T = 500$ mK. Lorentzian fitting gives primary peaks corresponding to the frequencies 37.5, 74.1 and 99.4 T. a.u., arbitrary units. (b) Temperature dependence of oscillation amplitude for $\theta = 90$ °. (c) Inverse Fourier transform (IFT) amplitude for the boxed area in a around 37.5 T. (d) Temperature dependence of the scaled Shubnikov-de Haas (circles) and IFT (squares) amplitudes for peaks indicated by arrowheads in (b) and (c). Fits to Eq. 6.1 give effective masses of $(1.24 \pm 0.02)m_0$ and $(1.26 \pm 0.03)m_0$ for $\Delta\rho_{xx}$ and IFT data, respectively.

where ρ_0 is the non-oscillatory component of the resistivity, ω_c is the cyclotron frequency ($e\mu_0 H/m^*$, where e is the elementary charge), k_B is Boltzmanns constant and $\hbar$ is Planck's constant divided by 2π. The fit shown in Fig. 6.5 (d) (red circles) leads to an effective mass of $m^* = (1.24 \pm 0.02)m_0$ (m_0 being the bare electron mass) and a Dingle temperature of $T_D = 5.58 \pm 0.07$ K, corresponding to a quantum scattering time of $\tau_q = \hbar/2\pi k_B T_D = (2.18 \pm 0.03) \times 10^{-13}$ s. However, the existence of multiple frequency components in the Shubnikovde Haas oscillations indicates that this simple analysis neglects multiple contributions to a given peak. Accordingly, we carried out the same analysis for the temperature dependence of the Shubnikovde Haas oscillations in Fig. 6.5 (c), which were constructed from the inverse Fourier transform of the first Fourier peak, centered at 37.5 T (Fig. 6.5 (a)). In this way (Fig. 6.5 (d), blue squares), we find that $m^* = (1.26 \pm 0.03)m_0$, $T_D = 4.48 \pm 0.2$ K and $\tau_q = (2.71 \pm 0.12) \times 10^{-13}$ s. The two approaches thus provide similar values and suggest that all Shubnikov-de Haas components have similar effective masses.

The values we calculate for m^* are comparable to the light effective mass for $SrTiO_3$ found in band structure calculations [24] and bulk experiments [25], lending some support to the subband assignments discussed above, although for a quantitative comparison a more sophisticated calculation would required. This intact effective mass, even under 2D confinement, may be a consequence of the unique design of our heterostructure, which is wholly composed of $SrTiO_3$, avoiding apparent electronic and structural barriers [26]. Using $m^* = 1.24m_0$, we obtain a Drude scattering time of $\tau = (7.82 \pm 0.13) \times 10^{-13}$ s from the low-field Hall mobility (Fig. 6.2 (a)), which is in reasonable agreement with the value of τ_q found above. We estimate the ratio between l_{mfp} and the Bardeen-Cooper-Schrieffer coherence length, ξ_{BCS}, to be $1.76\pi k_B T_c \tau/\hbar < 0.21$, that is, intermediate between the clean ($\xi_{BCS} \ll l_{mfp}$) and dirty ($\xi_{BCS} \approx l_{mfp}$) limits. Given the Fermi energy that we calculate (Sec. 6.5), an approximate value of $l_{mfp} \approx 97$ nm can be estimated for the lowest-energy subband.

6.5 Subband Calculation of a Delta-Doped $SrTiO_3$ Heterostructure

Introduction

In order to confirm a coincidence with the experimental results and a theoretical expectation, we make numerical calculations of the subband structure for the Delta-doped $SrTiO_3$ heterostructure. We first solve Poisson's equation to calculate the potential profile, and then derive the eigenstate energies E_n and envelope wavefunctions ψ_n (n is the

quantum number for each eigenstate) for the potential by solving Schrodinger's equation [27]. Both equations are solved using a conventional Runge-Kutta method. The assumptions are the following:

- 5.5 nm-thick 1 at. % Nb-doped $SrTiO_3$ layer is embedded in undoped $SrTiO_3$ layers.
- All dopants are fully activated.
- The potential is symmetric with respect to the center of the Nb-doped $SrTiO_3$ layer.

There are two further points to be considered in the case of $SrTiO_3$. One is the permittivity of $SrTiO_3$, which is strongly dependent on the electric field. This can drastically modify the potential profile, as we demonstrate below. The relative permittivity is empirically expressed as [28]

$$\epsilon(F) = 1 + \frac{b}{\sqrt{a + F^2}}, \tag{6.2}$$

where F is the electric field, $a = 2.79 \times 10^9$ V^2/m^2 and $b = 1.37 \times 10^9$ V/m are constants at low temperature. The second key feature is the conduction band structure, which is composed of heavy, light (and tetragonally split) and spin-orbit split bands [24]. To investigate these effects, we carried out calculations in the following three cases:

1. A single parabolic band is used with the experimentally determined effective mass m^* of $1.24m_0$, for a potential assuming constant (zero field) permittivity. (Fig. 6.6)
2. A single parabolic band is used with the experimentally determined $m^* = 1.24m_0$, for a potential including the electric field dependent permittivity at the level of approximation in [28]. (Fig. 6.7)
3. Three parabolic bands are used for the potential derived using the electric field dependent permittivity. (Fig. 6.8)

In the final case we used effective masses along the (100) direction at the Γ point of $1.9m_0$, $1.14m_0$ and $1.43m_0$ for the heavy ($E^{(1)}$), light and tetragonally split ($E^{(2)}$) and spin-orbit split ($E^{(3)}$) bands, respectively. The tetragonal splitting was $\Delta_{\rm t} = 1.54$ meV and the spin-orbit splitting was $\Delta_{\rm so} = 18$ meV. These values were taken from [25] for bulk $SrTiO_3$, which we simply assumed to be intact under two-dimensional confinement. Here we take the local dielectric approximation, and assume no inter-subband coupling.

Results and discussions

Fig. 6.6 shows the result of Case 1, where a constant permittivity and a single band are assumed. Because $\epsilon(0)$ exceeds 20,000 the confining potential is quite weak. Accordingly,

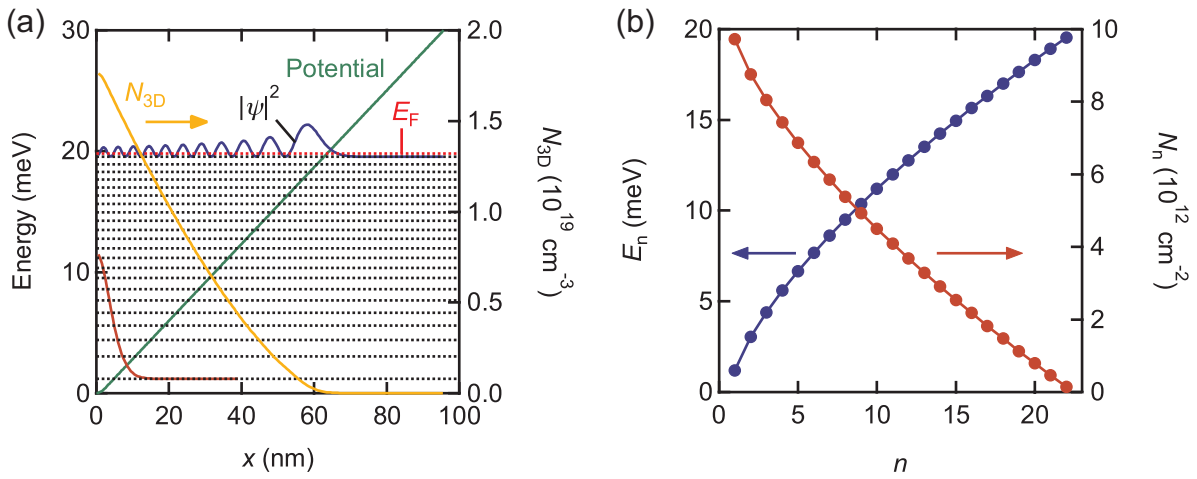

Figure 6.6: Result of subband calculations for Case 1 (single band, linear dielectric). (a) Potential profile, eigenstate energies, local electron density N_{3D} and corresponding envelope wavefunctions for the case of constant $\epsilon = \epsilon(0)$ and a single band with $m^* = 1.24m_0$. The wavefunctions are arbitrarily scaled and shifted upward by E_n. Only two wavefunctions with the lowest and highest energies are shown. (b) Eigenstate energy and carrier density for each subband as a function of the quantum number n.

the spacing between eigenstate energies is rather small, leading to a large number of occupied subbands. The Fermi energy E_F was determined self-consistently by insuring that the total electron density corresponds to the total number of dopants. By summing up the electron densities of each subband, the local three-dimensional electron density N_{3D} is calculated as a function of position x and is also plotted. The electron distribution extends to $x \sim 24$ nm if we take the half-maximum (x_{hm}) value, and $x \sim 40$ nm if we take the threshold below which 90% of the electrons are accounted for ($x_{90\%}$), both of which are much larger than the range of dopants ($|x| < 2.75$ nm). These measures of the electron width are also far wider than the superconducting thickness determined from the upper critical field anisotropy (8.4 nm, corresponding to $x_{SC} = 4.2$ nm), and thus corresponds very poorly to the data.

Fig. 6.7 shows the calculation for Case 2, where the inclusion of the ϵ nonlinearity leads to a strong modification of the potential profile. The suppression of ϵ by the electric field gives a much narrower and more confining potential well, leading to a larger spacing between the eigenstate energies, and hence a smaller number of occupied subbands. In this case x_{hm} is 4.3 nm and $x_{90\%}$ is 5.0 nm, corresponding reasonably well with the experimentally determined $x_{SC} = 4.2$ nm. Here the range of local electron density is consistent with the bulk superconducting phase diagram [29], and $x_{90\%}$ is approximately the 3D density threshold for the onset of bulk superconductivity.

Finally, in Case 3, we consider the effects of three nondegenerate conduction bands

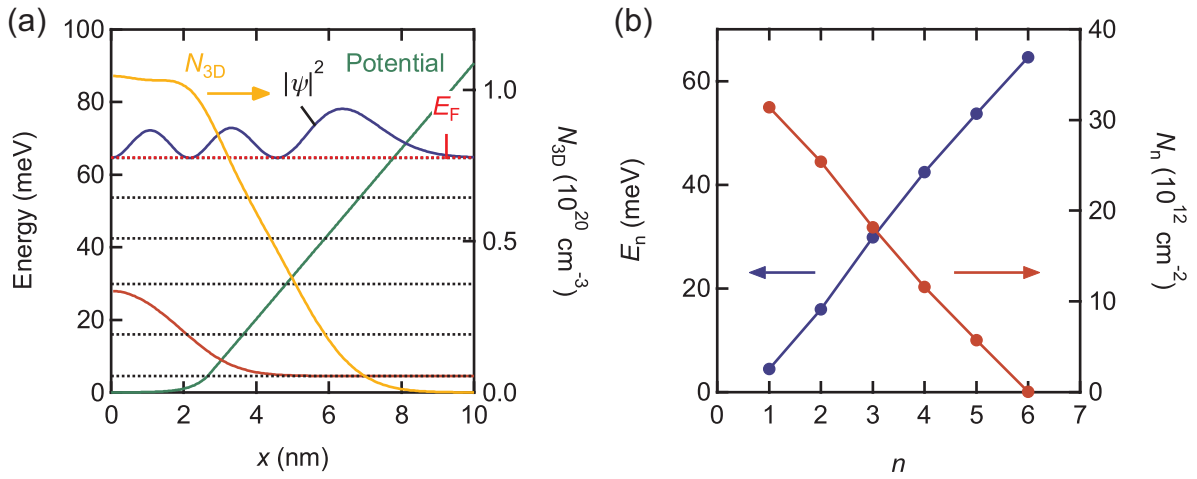

Figure 6.7: Result of subband calculations for Case 2 (single band, nonlinear dielectric). (a) Potential profile, eigenstate energies, local electron density N_{3D} and corresponding envelope wavefunctions for the case of electric-field dependent ϵ and a single band with $m^* = 1.24m_0$. The wavefunctions are arbitrarily scaled and shifted upward by E_n. Only two wavefunctions with the lowest and highest energies are shown. (b) Eigenstate energy and carrier density for each subband.

of $SrTiO_3$ using the bulk parameters given above, as well as dielectric nonlinearities, the results of which are shown in Fig. 6.8. Now x_{hm} is ~ 3.3 nm and $x_{90\%}$ is 3.6 nm, again in reasonable agreement with the experimental value. Case 3 is likely to be the best approximation to the actual electronic configuration, at this level of calculation. Here E_F is 35 meV. Using this value, the Fermi velocity $v_F = 8.1 \times 10^6$ cm/s is determined for the lowest heavy electron subband, corresponding to a mean free path $l_{mfp} = v_F = 97$ nm. In the case that the Shubnikov-de Haas oscillations we have observed correspond to the three light electron subbands, the corresponding values for the lowest light electron subband are $v_F = 1.0 \times 10^7$ cm/s and $l_{mfp} = 74$ nm.

Limitations

In these calculations, a number of simplifying approximations have been made, which include the following:

- Full electrostatic self-consistency of the fixed-charge potential with the electron distribution was not considered. Particularly with a strong dielectric nonlinearity, this may induce nontrivial corrections beyond those observed in conventional semiconductors.

- $d\epsilon/dx$ (i.e. polarization charge) and nonlocal dielectric effects were not incorporated, both of which grow in importance for large short-length-scale variations in the

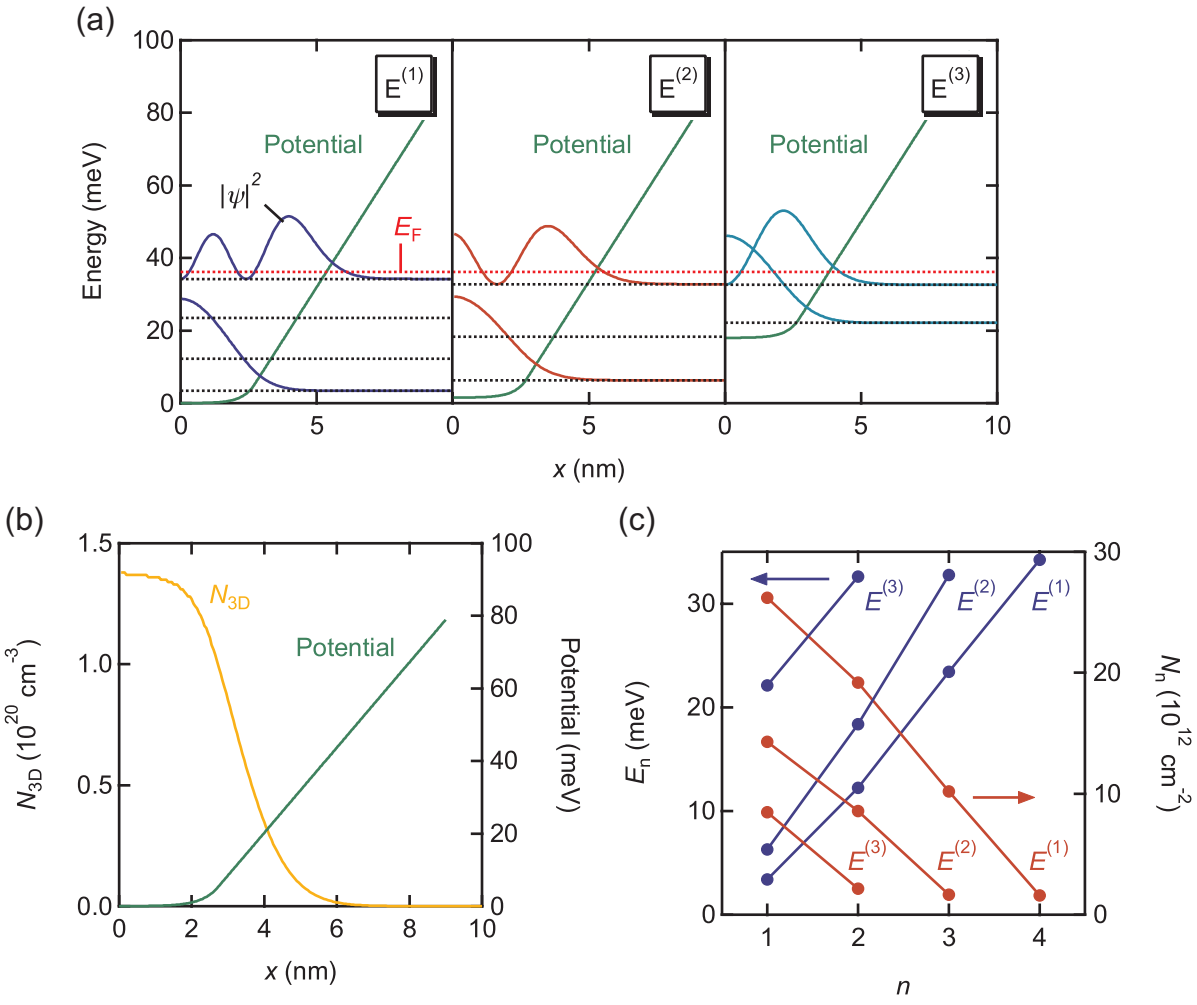

Figure 6.8: Result of subband calculations for Case 3 (three bulk-like bands, nonlinear dielectric). (a) Potential profile and eigenstate energies for the case of three conduction bands (bulk values) with an electric-field dependent ϵ. The potential, envelope wavefunctions and eigenstate energies are shifted by the corresponding energies $\Delta_{\rm t} = 1.54$ meV and $\Delta_{\rm so} = 18$ meV for the tetragonally split light electron band $E^{(2)}$ and spin-orbit split band $E^{(3)}$. (b) Local electron density $N_{\rm 3D}$ and potential versus position. (c) Eigenstate energy and carrier density are plotted as a function of n for each conduction subband.

potential.

- The electron pocket structure of bulk $SrTiO_3$ has been shown theoretically to be sensitive to both the tetragonal distortion and TiO_6 octahedral rotation [24], which has not been considered here by using only fixed bulk values. The deviation of the potential in Figs. 6.7 and 6.8 from a simple triangular well can be considered a proxy for spatial variations in the local crystal structure. When incorporated, the local electronic structure will also vary spatially.

In light of these simplifications, the calculations presented here should be considered to be a rough guide. A detailed numerical comparison would require a much more sophisticated calculation addressing these points.

6.6 Summary

In conclusion, we have demonstrated that delta-doped $SrTiO_3$ thin-film heterostructures can open new avenues connecting the previously disparate worlds of high-mobility semiconductors and low-dimensional superconductors. As we approach the limit at which Landau quantization becomes relevant, a potentially new and fascinating world opens before us [12]. Whether these novel phases proposed using idealized models, such as re-entrant superconductivity, can be observed will depend sensitively on the band structure in the delta-doped region, the g factor and Zeeman splitting, as well as further improvements in mobility. We also note that heterostructures such as these offer the possibility of engineering low-density quantum superlattices, which are artificial analogues of the layered high-temperature superconductors in which recent observations of Fermi surface oscillations have provoked intense interest [30]. With precise layer control in our heterostructures, it may be possible to tune the coupling between two-dimensional superconducting layers, which has been suggested to be of central importance in understanding the high-temperature superconducting copper oxides [31, 32].

References

[1] K. v. Klitzing, G. Dorda, and M. Pepper, New Method for High-Accuracy Determination of the Fine-Structure Constant Based on Quantized Hall Resistance, *Phys. Rev. Lett.* **45**, 494 (1980).

[2] T. Ando, A. B. Fowler, and F. Stern, Electronic Properties of Two-Dimensional Systems, *Rev. Mod. Phys.* **54**, 437 (1982).

[3] D. C. Tsui, H. L. Stormer, and A. C. Gossard, Two-Dimensional Magnetotransport in the Extreme Quantum Limit, *Phys. Rev. Lett.* **48**, 1559 (1982).

[4] E. Abrahams, S. V. Kravchenko, and M. P. Sarachik, Metallic Behavior and Related Phenomena in Two Dimensions, *Rev. Mod. Phys.* **73**, 251 (2001).

[5] E. A. Ekimov, V. A. Sidorov, E. D. Bauer, N. N. Mel'nik, N. J. Curro, J. D. Thompson, and S. M. Stishov, Superconductivity in Diamond, *Nature* **428**, 542 (2004).

[6] E. Bustarret, C. Marcenat, P. Achatz, J. Kamarik, F. Levy, A. Huxley, L. Ortega, E. Bourgeois, X. Blase, D. Debarre, and J. Boulmer, Superconductivity in Doped Cubic Silicon, *Nature* **444**, 465 (2006).

[7] Z. -A. Ren, J. Kato, T. Muranaka, J. Akimitsu, M. Kriener, and Y. Maeno, Superconductivity in Boron-Doped SiC, *J. Phys. Soc. Jpn.* **76**, 103710 (2007).

[8] T. Herrmannsdorfer, V. Heera, O. Ignatchik, M. Uhlarz, A. Mucklich, M. Posselt, H. Reuther, B. Schmidt, K.-H. Heinig, W. Skorupa, M. Voelskow, C. Wundisch, R. Skrotzki, M. Helm, and J. Wosnitza, Superconducting State in a Gallium-Doped Germanium Layer at Low Temperatures, *Phys. Rev. Lett.* **102**, 217003 (2009).

[9] X. Blase, E. Bustarret, C. Chapelier, T. Klein, and C. Marcenat, Superconducting Group-IV Semiconductors, *Nature Mater.* **8**, 375 (2009).

[10] A. M. Goldman and N. Markovic, Superconductor-Insulator Transitions in the Two-Dimensional Limit, *Phys. Today* **226**, 39 (1998).

[11] J. F. Schooley, W. R. Hosler, and M. L. Cohen, Superconductivity in Semiconducting $SrTiO_3$, *Phys. Rev. Lett.* **12**, 474 (1964).

[12] M. Rasolt and Z. Tesanovic, Theoretical Aspects of Superconductivity in Very High Magnetic Fields, *Rev. Mod. Phys.* **64**, 709 (1992).

[13] E. F. Schubert, Delta Doping of III-V Compound Semiconductors: Fundamentals and Device Applications, *J. Vac. Sci. Technol. A* **8**, 2980 (1990).

[14] E. F. Schubert, J. E. Cunningham, and W. T. Tsang, Electron-Mobility Enhancement and Electron-Concentration Enhancement in Delta-Doped n-GaAs at $T =$ 300 K, *Solid State Commun.* **63**, 591 (1987).

[15] M. A. Saifi and L. E. Cross, Dielectric Properties of Strontium Titanate at Low Temperature, *Phys. Rev. B* **2**, 677 (1970).

[16] T. Sakudo and H. Unoki, Dielectric Properties of $SrTiO_3$ at Low Temperatures, *Phys. Rev. Lett.* **26**, 851 (1971).

[17] K. A. Muller and H. Burkard, $SrTiO_3$: an Intrinsic Quantum Paraelectric Below 4 K, *Phys. Rev. B* **19**, 3593 (1979).

[18] J. K. Hulm, M. Ashkin, D. W. Deis, and C. K. Jones, Superconductivity in Semiconductor and Semimetals, *Prog. Low Temp. Phys.* **6**, 205 (1970).

[19] H. Nakamura, H. Takagi, I. H. Inoue, Y. Takahashi, T. Hasegawa, and Y. Tokura, Low Temperature Metallic State Induced by Electrostatic Carrier Doping of $SrTiO_3$, *Appl. Phys. Lett.* **89**, 133504 (2006).

[20] K. Ueno, S. Nakamura, H. Shimotani, A. Ohtomo, N. Kimura, T. Nojima, H. Aoki, Y. Iwasa, and M. Kawasaki, Electric-Field-Induced Superconductivity in an Insulator, *Nature Mater.* **7**, 855 (2008).

[21] A. D. Caviglia, S. Gariglio, N. Reyren, D. Jaccard, T. Schneider, M. Gabay, S. Thiel, G. Hammerl, J. Mannhart, and J. -M. Triscone, Electric Field Control of the $LaAlO_3/SrTiO_3$ Interface Ground State, *Nature* **456**, 624 (2008).

[22] A. Ohtomo and H. Y. Hwang, Surface Depletion in Doped $SrTiO_3$ Thin Films, *Appl. Phys. Lett.* **84**, 1716 (2004).

[23] M. Tinkham, Effect of Fluxoid Quantization on Transitions of Superconducting Films, *Phys. Rev.* **129**, 2413 (1963).

[24] L. F. Mattheiss, Effect of the 110 °K Phase Transition on the $SrTiO_3$ Conduction Bands, *Phys. Rev. B* **6**, 4740 (1972).

[25] H. Uwe, R. Yoshizaki, T. Sakudo, A. Izumi, and T. Uzumaki, Conduction Band Structure of $SrTiO_3$, *Jpn. J. Appl. Phys.* **24S2**, 335 (1985).

[26] M. J. Yang, P. J. Lin-Chung, B. V. Shanabrook, J. R. Waterman, R. J. Wagner, and W. J. Moore, Enhancement of Cyclotron Mass in Semiconductor Quantum Wells, *Phys. Rev. B* **47**, 1691 (1993).

[27] E. F. Schubert, *Delta-Doping of Semiconductors*, (Cambridge Univ. Press, Cambridge, 1996).

[28] T. Yamamoto, S. Suzuki, K. Kawaguchi, and K. Takahashi, Temperature Dependence of the Ideality Factor of $Ba_{1-x}K_xBiO_3$/Nb-Doped $SrTiO_3$ All-Oxide-Type Schottky Junctions, *Jpn. J. Appl. Phys.* **37**, 4737 (1998).

[29] C. S. Koonce, M. L. Cohen, J. F. Schooley, W. R. Hosler, and E. R. Pferifer, Superconducting Transition Temperatures of Semiconducting $SrTiO_3$, *Phys. Rev.* **163**, 380 (1967).

[30] N. Doiron-Leyraud, C. Proust, D. LeBoeuf, J. Levallois, J. -B. Bonnemaison, R. Liang, D. A. Bonn, W. N. Hardy, and L. Taillefer, Quantum Oscillations and the Fermi Surface in an Underdoped High-T_c Superconductor, *Nature* **447**, 565 (2007).

[31] P. W. Anderson, Interlayer Tunneling Mechanism for High-T_c Superconductivity: Comparison with c Axis Infrared Experiments, *Science* **268**, 1154 (1995).

[32] S. Chakravarty, H. -Y. Kee, and K. Volker, An Explanation for a Universality of Transition Temperatures in Families of Copper Oxide Superconductors, *Nature* **428**, 53 (2004).

Chapter 7

Conclusion

The study of oxide heterostructures has been difficult in spite of the versatile physical properties expected from bulk, due to the difficulty of precise structural and physical control of the materials growth. In this Thesis, low-dimensional electronic properties of oxide heterostructures are investigated by using the precise control of interface termination and the delta-doping technique. The structures were studied through three physical phenomena: photoconductivity, superconductivity and normal-state transport. It is revealed that in the two target systems, the $LaAlO_3/SrTiO_3$ interfaces and $SrTiO_3/Nb{:}SrTiO_3/SrTiO_3$ heterostructures, they show novel properties prospect for future applications, as follows.

1. The insulating $LaAlO_3/SrTIO_3$ P-type and (110) interfaces were investigated via photoconductivity effect. The interface states with broadened energy levels were revealed at the interfaces, affecting the long life-time and non-exponential relaxation of the photo-induced carriers. The long lifetime of photo-induced carriers at the interface indicates the possibility of persistent photoconductivity in ~ 20 mK region, which would be an attractive method to tune the carrier density continuously and investigate the low-temperature transport properties.

2. The superconducting properties of the $SrTiO_3/Nb{:}SrTiO_3/SrTiO_3$ heterostructures were investigated. The dimensionality crossover of superconductivity from three dimensions to two dimensions was observed as the doped layer becomes thinner. We also observed novel characteristics in the thin limit such as an increase of the mean free path, an increase of the superconducting transition temperature, and the violation of the Pauli paramagnetic limit. The realization of the delta-doped superconductor can be applied to the construction of superconductor superlattices in analogy with layered superconductors, for example, the copper-oxide superconductors. It is expected that the interlayer coupling between the delta-doped superconductor can be investigated experimentally by varying the inter-layer distance.

3. The formation of two-dimensional Fermi surface in the delta-doped $SrTiO_3$ heterostructure was manifested by two-dimensional quantum oscillations in the normal-state, which is the first realization of two-dimensional Shubnikov-de Haas oscillations in a two-dimensional superconductor. This result forms a platform for studying the possible interplay between quantum oscillations and superconductivity, a region which has never been explored experimentally.

These results form a basis for oxide semiconductors to be tailored in low dimensions with low electron density and high mobility. As a future perspective, one subject is further reducing the defect density and increasing the electron mobility, where we can expect to observe the quantum Hall effect, a well-known phenomena for clean two-dimensional electronic systems. $SrTiO_3$ is expected to show relatively strong electron correlation effects from its large effective electron mass. It will be interesting to see such exotic effects of $SrTiO_3$ through quantum transport phenomena in comparison with conventional semiconductors.

The second subject is to combine the $SrTiO_3$ two-dimensional electron gas with other perovskite oxides, and make artificial correlated interfaces. It is well-known that the multi-ferroics show successful coupling between several ferroic characteristics in perovskite oxides. Thus, new ways to control the electronic degrees of freedom in the $SrTiO_3$ layer, and vice versa, may be created by combining it with other perovskite oxides such as cuprates showing high-T_c superconductivity or manganites showing colossal magnetoresistance. If it is possible, this can be connected to the realization of oxide devices operated based on conceptually new mechanisms.

Acknowledgements

To begin with, I would like to express my appreciation to Professor Harold Yoonsung Hwang. He introduced me to the field of oxide thin films, where I could encounter wide range of interesting scientific developments. With his constructive comments, I was able to pursue valuable research always with a clear point in mind. His generous encouragement of my scientific activity allowed me to write papers in journals, and attend domestic and international conferences.

Assistant Professor Yasuyuki Hikita always gave me beneficial comments and warm support. From his enthusiasm about research I learnt to have a strong will, and not to lose confidence. Also, his help in the optic measurements was essential to build Chapter 4. Mr. Yusuke Kozuka helped me most closely, both experimentally and mentally. It was a great pleasure to study the high-quality $SrTiO_3$ films grown by him, which was indispensable for Chapters 5 and 6. His thorough attitude and punctual thinking in science were what I have pursued mostly in my master's work. Dr. Christopher Bell kindly prepared the $LaAlO_3/SrTiO_3$ interface samples studied in Chapter 4. Many critical arguments I have made in this Thesis could be born from his vast experience of the oxide interface, as well as his deep understanding in superconductivity. I received generous support from Associate Professor Bog-Gi Kim from Pusan National University. As well as his acute experimental skills, which helped me to make clean measurements, light conversations with him helped me not to forget my mother language.

I want to to thank the laboratory members for their kind help in daily life and wonderful interactions in research: Dr. Yanwu Xie, Mr. Takeaki Yajima, Mr. Yuichi Ota, Mr. Motohide Kawamura, Mr. Yasuo Nakanishi, Mr. Hiroki Sato, Mr. Satoshi Harashima, Mr. Moyuru Kurita, and Mr. Taro Wakamura, as well as former members, Associate Professor Jong Hyun Song, Dr. Shunsuke Tsuda, Dr. Kei Takahashi, Mr. Takuya Higuchi, Mr. Kotaro Takeyasu, and Mr. Takeaki Hidaka. Special thanks also to the Korean members: Mr. Daeyoung Kwon, Mr. Bongju Kim, Mr. Youngsoo Wu, and Ms. Sunhwa Kim. I also had enjoyable time with visiting members: Ms. Guneeta Singh-Bhalla, Mr. James M. Rondinelli, and Mr. Hans Boschker. I greatly appreciate Professor Mikk Lippmaa and his laboratory members for allowing me to use their equipment.

I would like to thank Ms. Makiko Tanaka, who is a kind and beautiful secretary, and helped me in my research life, as well as with painful procedures to be a foreign student.

Lastly, I give my thank to my family for their invariable support at all times.

Appendix A

DX center and Persistent Photoconductivity

The DX center is one type of deep center caused by defects whose energy levels are located near the middle of the bandgap. The properties of deep centers cannot be understood within effective mass theory, which on the contrary can be successfully applied to shallow centers [A1]. The DX center was discovered by D. V. Lang *et al.* in 1979 [A2], in the ternary alloy system n-$Al_xGa_{1-x}As$ with $x > 0.22$. It was confirmed experimentally, as shown in Fig. A.1 (a-1), that the center exhibits a higher activation energy which can be excited optically, and requires a finite energy to thermally capture excited electrons. As a result, samples containing these centers exhibit persistent photoconductivity at low temperatures (typically $T < 100$ K), because the optically excited electrons cannot be captured by the centers and remain in the conduction band, as shown in Fig. A.1 (a-2). Later, the donor displacement model [A3] was proposed to explain the formation of DX centers. In this model, the donor is relaxed by the light irradiation and the atomic displacement creates dangling bonds, producing excess carriers. Because a finite energy is needed to recover the relaxation, it can remain in a metastable state for a very long time ($> 10^9$ sec [A4]) at low temperatures.

By using persistent photoconductivity, the carrier density can be tuned without having a structural change. For example, chemical substitution may disturb the atomic structure, and electrostatic field-effect doping needs a surface preparation process which may create defect states [A5]. In this sense, persistent photoconductivity has been a useful tool to investigate the transport properties of semiconductors. For example, using Si doped $Al_{0.3}Ga_{0.7}As$ [A4], the carrier density can be tuned to control a Metal-Insulator transition, as shown in Fig. A.2 (a). In nitride-based heterostructures [A6], the illumination can tune the Shubnikov-de Haas oscillation period of the high-mobility two-dimensional electron gas at the heterointerface in Fig. A.2 (b). In Chap. 4, the possibility of persistent photoconductivity at the $LaAlO_3/SrTiO_3$ interface is examined.

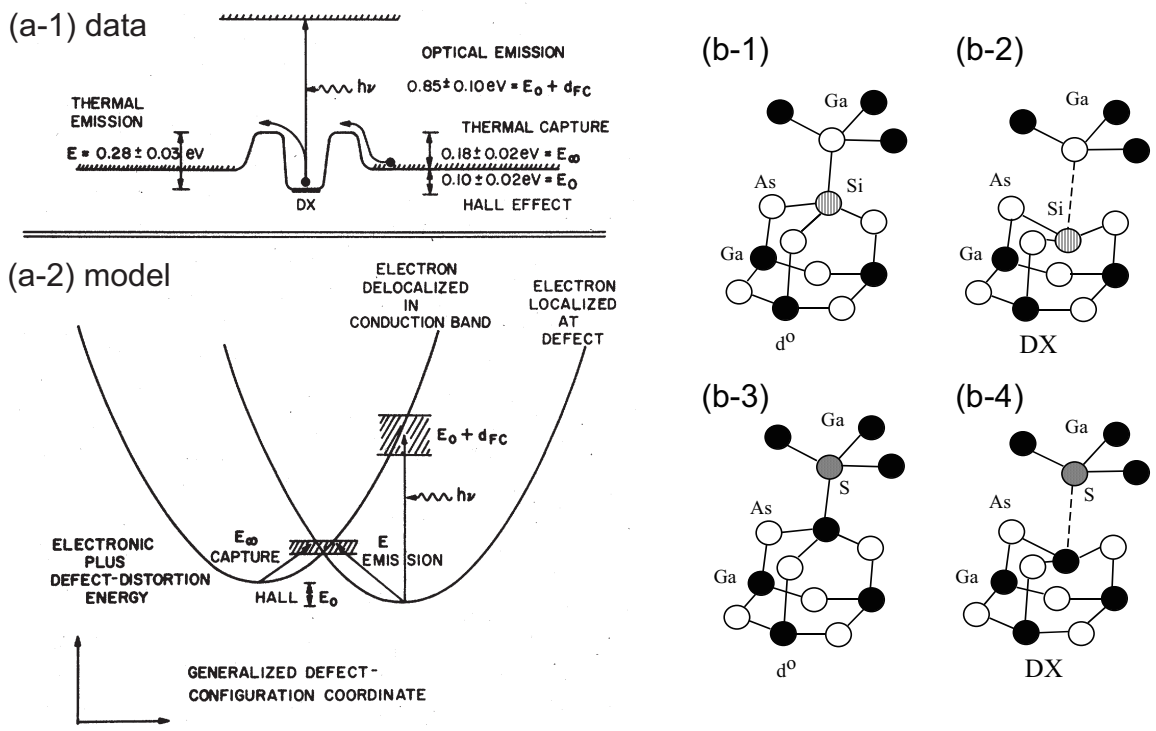

Figure A.1: Characteristics of DX centers and the donor displacement model. The experimental data and the proposed model in Te doped $Al_xGa_{1-x}As$ alloys [A2] are shown in (a-1) and (a-2). The donor displacement model [A3] in forming the DX center is shown in (b). In (b-1) and (b-3) the substitutional atoms (Si and S) are in their neutral states and located at tetrahedral sites. In (b-2) and (b-4) the substitutional atoms are displaced along one of the bonds into a site where it is effectively surrounded by only three host atoms.

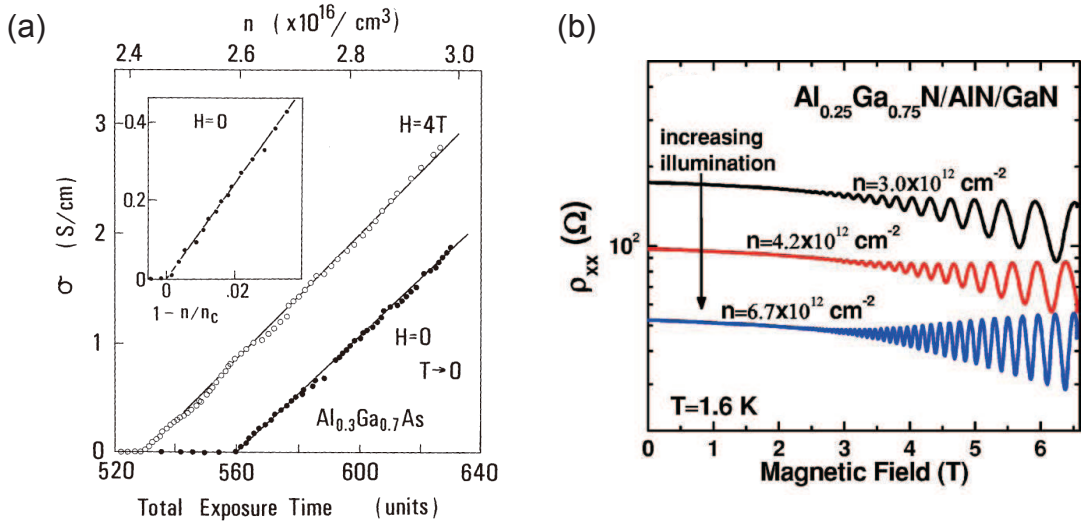

Figure A.2: Tuning of the carrier density by persistent photoconductivity. (a) Conductivity modulation as a function of the exposure times in Si doped $Al_{0.3}Ga_{0.7}As$ [A4]. (b) Modulation of the Shubnikov-de Haas oscillations in a Nitride heterostructure [A6].

References

[A1] P. Y. Yu and M. Cardona, *Fundamentals of Semiconductors*, 3rd ed., (Springer, Berlin, 2005).

[A2] D. V. Lang, R. A. Logan, and M. Jaros, Trapping Characteristics and a Donor-Complex (DX) Model for the Persistent-Photoconductivity Trapping Center in Te-Doped $Al_xGa_{1-x}As$, *Phys. Rev. B* **19**, 1015 (1979).

[A3] D. J. Chadi and K. J. Chang, Energetics of DX-Center Formation in GaAs and $Al_xGa_{1-x}As$ Alloys, *Phys. Rev. B* **39**, 10063 (1989).

[A4] S. Katsumoto, F. Komori, N. Sano, and S. Kobayashi, Fine Tuning of Metal-Insulator Transition in $Al_{0.3}Ga_{0.7}As$ Using Persistent Photoconductivity, *J. Phys. Soc. Jpn.* **56**, 2259 (1987).

[A5] K. Shibuya, T. Ohnishi, T. Uozumi, T. Sato, K. Nishio, and M. Lippmaa, Observation of $SrTiO_3$ In-Gap States by Depletion Mode Field Effect, *Appl. Phys. Lett.* **92**, 032109 (2008).

[A6] N. Biyikli, U. Ozgur, X. Ni, Y. Fu, H. Morkoc, and C. Kurdak, Illumination and Annealing Characteristics of Two-dimensional Electron Gas Systems in Metal-Organic Vapor-Phase Epitaxy Grown $Al_xGa_{1-x}N$/AlN/GaN Heterostructures, *J. Appl. Phys.* **100**, 103702 (2006).

2009 Master's Thesis: Low-Dimensional Electronic Properties of Oxide Heterostructures

（酸化物ヘテロ構造における低次元電子物性）

86017 Minu Kim